Photoluminescence Reveals Charge Carrier Recombination in Organic and Hybrid Semiconductors

Dissertation zur Erlangung
des naturwissenschaftlichen Doktorgrades
der Julius–Maximilians–Universität Würzburg

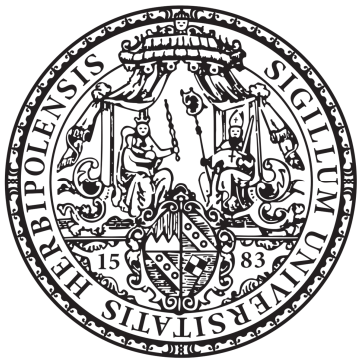

vorgelegt von
Liudmila Kudriashova
aus Ryazanskaya Oblast, Russland

Würzburg, 2019

Eingereicht am:
bei der Fakultät für Physik und Astronomie

1. Gutachter: Prof. Dr. Vladimir Dyakonov
2. Gutachter: Prof. Dr. Sven Höfling
3. Gutachter:
der Dissertation.

1. Prüfer: Prof. Dr. Vladimir Dyakonov
2. Prüfer: Prof. Dr. Sven Höfling
3. Prüfer: Prof. Dr. Bernd Engels
im Promotionskolloquium.

Tag des Promotionskolloquiums: 18.12.2019

Doktorurkunde ausgehändigt am:

Contents

Chapter 1

Introduction

1.1. Challenges of Today's Material Science

Human fondness of light is unbreakable. We use light in our daily activities, for communication, for safety, for medicine, and for entertainment. The list can be continued. For instance, almost every modern gadget incorporates a light-emitting screen or at least an array of light-emitting diodes. The unceasing production and further development of displays and light sources for various applications require low-cost energy-efficient light-emitting devices with strictly defined optical and mechanical properties.

The idea of energy-efficient device brings us to other important concerns of today's world: energy production, consumption, and the associated terror of global warming. The alarming statistics of CO_2 concentration in the atmosphere[1,2] and the corresponding growth of global temperature[3] (see **Figure 1.1**) along with the predicted depletion of fossil fuels[4] show that the current world-spread obsession with renewable energy sources has very reasonable grounds.

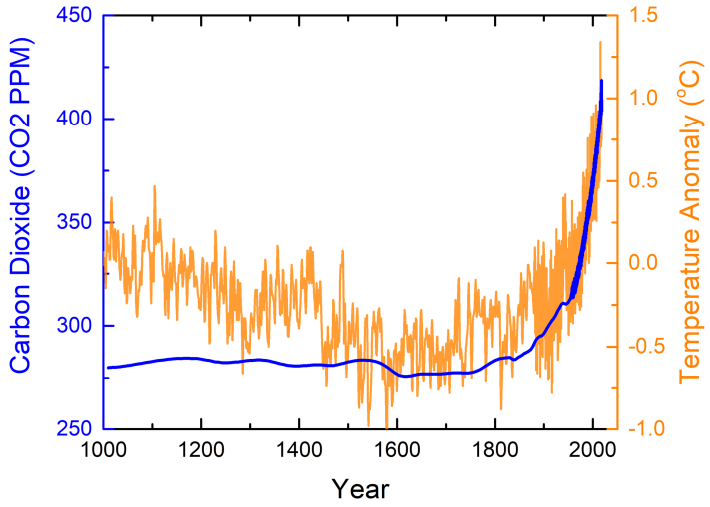

Figure 1.1. Historical CO_2 records from Law Dome ice cores (blue) and global temperature record (orange). Adopted from https://www.co2.earth/.

One of the environment-friendly alternatives to fuel combustion is the usage of photovoltaic effect to convert solar light into electricity. The key physical processes which define performance of every photovoltaic device are light absorption and subsequent dynamics of the generated excited species.

Generally speaking, absorption and emission of photons accompanied by generation and recombination of charge carries are crucial for development of both efficient light-emitting diodes and solar cells. Collective research effort of the last decade yielded new

promising players in these fields, such as thermally activated delayed fluorescence emitters for organic light-emitting diodes and perovskite absorbers for hybrid organic–inorganic solar cells. Further development of these fascinating materials is possible only with deep understanding of the light–matter interaction that lies behind the impressive device performances.

1.2. Photoluminescence Spectroscopy

A straightforward way to study interaction of light and matter in whole complexity is photoluminescence (PL) spectroscopy, which is based on ability of a chromophore to be excited upon light absorption and emit photons upon subsequent relaxation to the ground state. Absorption and luminescence characteristics, such as spectrum, lifetime, and absolute quantum yield, are defined by the intrinsic properties of the emitter, by its molecular surrounding, by microscopic material structure, and by geometry of the sample.

PL spectroscopy exists for almost two centuries. The first scientific report on fluorescence was published in 1845 By Sir John Frederick William Herschel and was called *"On a case of superficial colour presented by a homogeneous liquid internally colourless"*.[5] Certainly, the spectroscopic techniques have been well developed since then. Up-to-date PL toolbox includes a variety of steady-state and time-resolved measurements. PL is suitable for precise evaluation of absolute quantum yields, as well as for relative estimates on-the-run. It is one of a few contactless techniques for material characterization. At the same time, PL can be used to probe charge carrier recombination at the interfaces and in complete devices.

Meanwhile, the time scales of time-resolved PL (TRPL) allow observation of ultrafast processes associated with molecular scale dynamics (~1 ps), long-lived phosphorescence associated with triplet transitions (~1 s), and everything in between. Being proportional to the density of excited states, TRPL signal is sensitive to all variety of recombination events including nonradiative quenching and trap-assisted recombination. On top of that, spectroscopic equipment is relatively simple and affordable and, therefore, is present in almost every scientific laboratory. On the other hand, such powerful tool as PL is often used just for additional characterization of highly emissive compounds, but not for extensive self-consistent material study. Full complexity of background photophysical processes is frequently overseen in analysis of spectroscopic data.

In this work, we aimed to give a fresh look on PL spectroscopy and its applications in the hottest areas of material research. The introductory **Chapter 2** of this thesis gives a brief overview of the main spectroscopic ideas, corresponding notions, and experimental techniques. The information given in the **Chapter 2** is sufficient for basic measurements and the data interpretation. **Chapter 3** addresses photophysical processes responsible for light absorption and generation in organic and hybrid emitters. The effects of environment, from single molecule to polycrystalline film, are discussed. The following **Chapters 4–6** are written as self-consistent scientific reports. There we show how PL reveals excitation dynamics in perovskite absorbers and in the novel organic emitters.

1.3. Perovskite Absorbers

Perovskites are hybrid organometallic crystalline materials sharing the same ABX_3 stoichiometry, where A is an organic cation, B is a metal cation, and X is a halide anion (see **Figure 1.2a**). At first, perovskite application in photovoltaics was motivated by scientific curiosity. Unexpectedly, the perovskite-based devices advanced greatly within less than a decade of academic research and attained power conversion efficiencies of 22.7%.[6] **Figure** 1.2**b** shows a general layout of planar solar cell employing polycrystalline perovskite thin film. Presently, the best perovskite solar cells rival the record silicon-based devices and pave the way to commercialization.

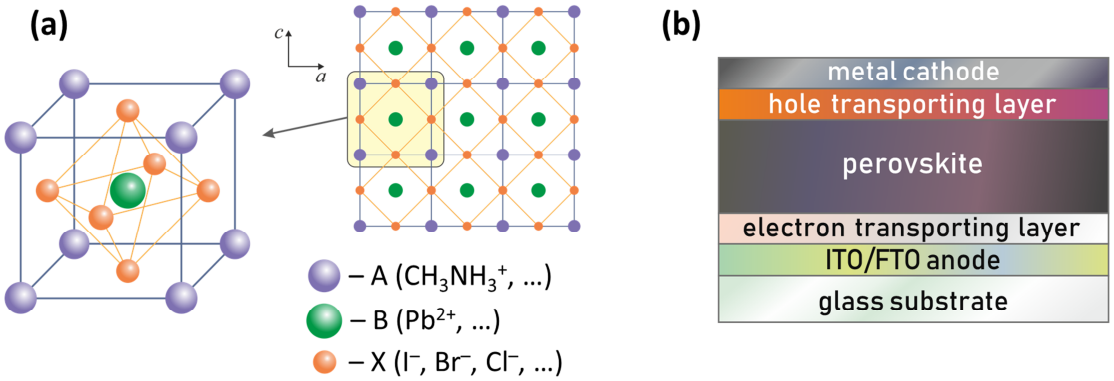

Figure 1.2. (a) ABX_3 crystalline structure of metal–halide perovskites. (b) General layout of perovskite solar cell in planar configuration.

Unprecedented development of perovskite photovoltaics attracted interest of research groups from all around the world. The skyrocketing number of perovskite-related publications was accompanied by the controversy of published findings. In particular, the reported PL lifetimes varied from tens of picoseconds to microseconds even for the most established methylammonium lead iodide thin films ($CH_3NH_3PbI_3$ or MAPI).[7,8] Although the exciton binding energies were found to be smaller than k_BT at room temperature and the concept of free recombining electrons and holes was generally agreed upon,[9] the exact picture of carrier recombination still remained unclear. Additionally, presence of charge-selective layers was shown to escalate the PL decay,[10,11] whereas the role of interfaces was not elucidated. Do they introduce surface defects, promote interfacial recombination or change the perovskite growth conditions and film morphology? In **Chapter 4** of this thesis, we address impact of charge transporting materials on carrier dynamics in perovskites, isolate bulk and interfacial effects by means on transient PL, apply kinetic model for electron–hole recombination, and show why the concept of lifetime is not straightforward for TRPL spectroscopy of perovskite thin films.

Another important cause of disagreement between intrinsic and apparent emission parameters of perovskites is strong self-absorption and subsequent re-emission of PL. In combination, those effects are usually referred to as photon recycling. The photon recycling

introduces series of spectral shifts in microscopic luminescence[12] and prolongs macroscopically detected PL decay.[13] The photon recycling can affect the performance of solar cells,[14] although the magnitude of the effect is questionable.[15] A complete model for spectral changes caused by photon recycling has not been developed up to now, because the effect involves complex interplay between several generations of PL photons and charge carriers. Moreover, the corresponding measurements imply microscopic detection of PL at a broad dynamic range of intensities. In **Chapter 5**, we demonstrate the effect of photon recycling in polycrystalline perovskite films by means of double-objective spatially resolved PL and propose a numerical model for the obtained emission maps.

1.4. Thermally Activated Delayed Fluorescence Emitters

Light-emitting diode produces photons via electrical injection of charge carriers and their subsequent recombination in the active layer. Organic active layers offer a number of advantages: light weight, flexibility, tunability of the emission color in the entire optical region, and large variety of possible molecular structures. First practical electroluminescence diode based on purely organic material (OLED) was demonstrated by C. W. Tang and S. A. VanSlyke in 1987.[16] This pioneering device together with the first polymer-based OLED presented in 1990 by J. H. Burroughes *et al.*[17] resulted in a rapid development of plastic electronics followed by OLED commercialization.

OLED efficiency is generally limited by spin statistics: when injected electrically, charge carriers form no more than 25% of singlet excitons.[18] The remaining 75% of triplet excitons mostly undergo nonradiative relaxation to the ground state at room temperature (**Figure 1.3b**). Thus, the maximum internal electroluminescence efficiency of conventional organic emitters does not exceed 25%. Consequently, the maximum possible external quantum efficiency (EQE) of the resulting OLED is only 5% (at the assumed 20% light outcoupling).

Luckily, the excited triplets can also be harvested radiatively at certain conditions. The alternative radiative decay pathways for triplets include room-temperature phosphorescence,[19–22] triplet–triplet annihilation,[23,24] and thermally activated delayed fluorescence (TADF).[25,26] The last was the subject of our study. TADF results from radiative recombination of singlet excitons produced by triplet-to-singlet reverse intersystem crossing (RISC). TADF allows 100% internal electroluminescence quantum yield, but exerts strict requirements on the molecular design.

The RISC is a temperature activated process. Therefore, its efficiency depends exponentially on the singlet–triplet energy splitting, which should be close to $k_B T = 26\ meV$ in order to provide efficient TADF at room temperature. This condition can be fulfilled by a large dihedral angle between the donor and acceptor parts of the molecule. Additionally, the donor and acceptor units should form a highly emissive charge-transfer state. These requirements on geometry and energetics significantly limit the choice of building blocks for TADF molecules.

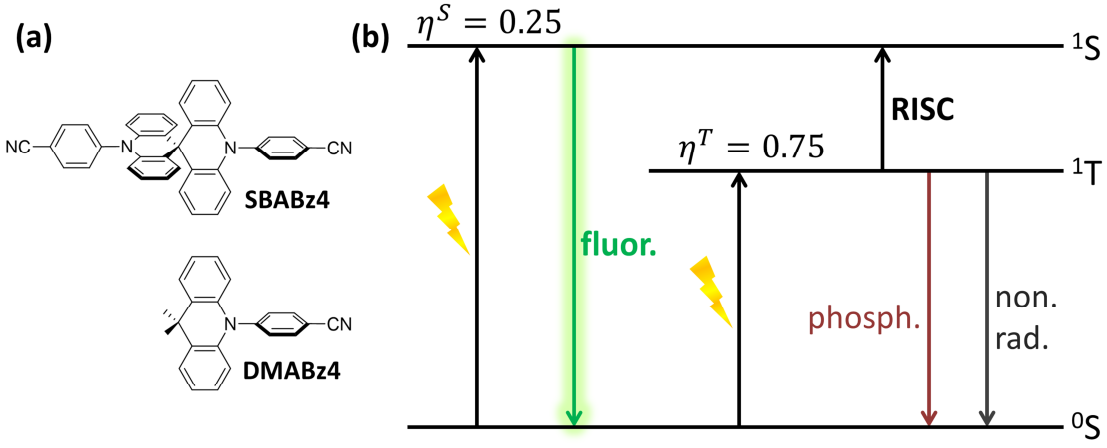

Figure 1.3. (a) Dimer and monomer TADF emitters based on acridane and benzonitrile units. (b) Scheme of electrical injection and subsequent excitonic transitions in organic emitter.

Design and synthesis of deep blue TADF emitters offer additional challenges. First, both singlet and triplet energies should be rendered high in order to provide high energy of luminescence photons while maintaining the narrow singlet–triplet gap. Second, the excited-state orbital should be rather delocalized in order to provide efficient fluorescence, but such delocalization causes a red shift of emission. Despite all the challenges stated here, several efficient deep blue TADF emitters were recently reported.[27–30]

Quantum chemical calculations can roughly predict energetics of organic molecules. Nevertheless, only experiment gives the final verdict on the emission properties of a newly synthesized compound and on its value for the device application. OLED fabrication and optimization are extremely demanding in terms of both material and effort. Therefore, the PL spectroscopy is an essential time-saving prerequisite for device development. PL gives valuable information about quantum yields of the involved transitions, reveals emission color, accounts for molecular surrounding, highlights structure–property relationships, and, ultimately, allows further optimization of the molecule. **Chapter 6** of this thesis presents extensive study of two blue emitters (**Figure 1.3a**), whose TADF properties were proven independently by oxygen quenching and temperature-dependent time-resolved PL.

1.5. References

(1) Etheridge, D. M.; Steele, L. P.; Langenfelds, R. L.; Francey, R. J.; Barnola, J.-M.; Morgan, V. I. Carbon Dioxide Information Analysis Center. *Historical CO2 Records from the Law Dome DE08, DE08-2, and DSS Ice Cores.* https://www.co2.earth/co2-ice-core-data (accessed Nov 17, 2018).

(2) National Oceanic and Atmospheric Administration. Earth System Research Laboratory. *Global Monitoring Division - Mauna Loa Observatory.* https://www.esrl.noaa.gov/gmd/ccgg/trends/gl_full.html (accessed Nov 17, 2018).

(3) National Oceanic and Atmospheric Administration. *Climate - Global Temperature Anomalies.* https://www.climate.gov/maps-data/dataset/global-temperature-anomalies-graphing-tool (accessed Nov 17, 2018).

(4) Shafiee, S.; Topal, E. When Will Fossil Fuel Reserves Be Diminished? *Energy Policy* **2009**, *37*, 181–189.

(5) Sir Herschel, J. F. W. On a Case of Superficial Colour Presented by a Homogeneous Liquid Internally Colourless. *Phil. Trans. Roy. Soc.* **1845**, *135*, 143–145.

(6) National Renewable Energy Laboratory. Research Cell Record Efficiency Chart. https://www.nrel.gov/pv/assets/images/efficiency-chart.png (accessed Nov 20, 2018).

(7) Chen, K.; Barker, A. J.; Morgan, F. L. C.; Halpert, J. E.; Hodgkiss, J. M. Effect of Carrier Thermalization Dynamics on Light Emission and Amplification in Organometal Halide Perovskites. *J. Phys. Chem. Lett.* **2015**, *6*, 153–158.

(8) Stranks, S. D.; Burlakov, V. M.; Leijtens, T.; Ball, J. M.; Goriely, A.; Snaith, H. J. Recombination Kinetics in Organic-Inorganic Perovskites: Excitons, Free Charge, and Subgap States. *Phys. Rev. Appl.* **2014**, *2*, 1–8.

(9) Miyata, A.; Mitioglu, A.; Plochocka, P.; Portugall, O.; Wang, J. T.-W.; Stranks, S. D.; Snaith, H. J.; Nicholas, R. J. Direct Measurement of the Exciton Binding Energy and Effective Masses for Charge Carriers in Organic–inorganic Tri-Halide Perovskites. *Nat. Phys.* **2015**, *11*, 582–587.

(10) Wojciechowski, K.; Stranks, S. D.; Abate, A.; Sadoughi, G.; Sadhanala, A.; Kopidakis, N.; Rumbles, G.; Li, C.-Z.; Friend, R. H.; Jen, A. K.-Y.; et al. Heterojunction Modification for Highly Efficient Organic–Inorganic Perovskite Solar Cells. *ACS Nano* **2014**, *8*, 12701–12709.

(11) Stranks, S. D.; Eperon, G. E.; Grancini, G.; Menelaou, C.; Alcocer, M. J. P.; Leijtens, T.; Herz, L. M.; Petrozza, A.; Snaith, H. J. Electron-Hole Diffusion Lengths Exceeding 1 Micrometer in an Organometal Trihalide Perovskite Absorber. *Science* **2014**, *342*, 341–344.

(12) Pazos-Outon, L. M.; Szumilo, M.; Lamboll, R.; Richter, J. M.; Crespo-Quesada, M.; Abdi-Jalebi, M.; Beeson, H. J.; Vru ini, M.; Alsari, M.; Snaith, H. J.; et al. Photon Recycling in Lead Iodide Perovskite Solar Cells. *Science* **2016**, *351*, 1430–1433.

(13) Staub, F.; Hempel, H.; Hebig, J. C.; Mock, J.; Paetzold, U. W.; Rau, U.; Unold, T.; Kirchartz, T. Beyond Bulk Lifetimes: Insights into Lead Halide Perovskite Films from Time-Resolved Photoluminescence. *Phys. Rev. Appl.* **2016**, *6*, 1–13.

(14) Kirchartz, T.; Staub, F.; Rau, U. Impact of Photon-Recycling on the Open-Circuit Voltage of Metal Halide Perovskite Solar Cells. *ACS Energy Lett.* **2016**, *1*, 731–739.

(15) Fang, Y.; Wei, H.; Dong, Q.; Huang, J. Quantification of Re-Absorption and Re-Emission Processes to Determine Photon Recycling Efficiency in Perovskite Single Crystals. *Nat. Commun.* **2017**, *8*, 1–9.

(16) Tang, C. W.; VanSlyke, S. A. Organic Electroluminescent Diodes. *Appl. Phys. Lett.* **1987**, *51*, 913–915.

(17) Burroughes, J. H.; Bradley, D. D. C.; Brown, A. R.; Marks, R. N.; Mackay, K.; Friend, R. H.; Burns, P. L.; Holmes, A. B. Light-Emitting Diodes Based on Conjugated Polymers. *Nature* **1990**, *347*, 539–541.

(18) Segal, M.; Baldo, A.; Holmes, J.; Forrest, R.; Soos, G. Excitonic Singlet-Triplet Ratios in Molecular and Polymeric Organic Materials. *Phys. Rev. B - Condens. Matter Mater. Phys.* **2003**, *68*, 1–14.

(19) Baldo, M. A.; O'Brien, D. F.; You, Y.; Shoustikov, A.; Sibley, S.; Thompson, M. E.; Forrest, S. R. Highly Efficient Phosphorescent Emission from Organic Electroluminescent Devices. *Nature* **1998**, *395*, 151–154.

(20) Ma, Y.; Zhang, H.; Shen, J.; Che, C. Electroluminescence from Triplet Metal—Ligand Charge-Transfer Excited State of Transition Metal Complexes. *Synth. Met.* **1998**, *94*, 245–248.

(21) Adachi, C.; Baldo, M. A.; Thompson, M. E.; Forrest, S. R. Nearly 100% Internal Phosphorescence Efficiency in an Organic Light Emitting Device. *J. Appl. Phys.* **2001**, *90*, 5048–5051.

(22) Köhler, A.; Wilson, J. S.; Friend, R. H. Fluorescence and Phosphorescence in Organic Materials. *Adv. Mater.* **2002**, *14*, 701–707.

(23) Kondakov, D. Y. Characterization of Triplet-Triplet Annihilation in Organic Light-Emitting Diodes Based on Anthracene Derivatives. *J. Appl. Phys.* **2007**, *102*, 114504.

(24) Hu, J. Y.; Pu, Y. J.; Satoh, F.; Kawata, S.; Katagiri, H.; Sasabe, H.; Kido, J. Bisanthracene-Based Donor-Acceptor-Type Light-Emitting Dopants: Highly Efficient Deep-Blue Emission in Organic Light-Emitting Devices. *Adv. Funct. Mater.* **2014**, *24*, 2064–2071.

(25) Goushi, K.; Yoshida, K.; Sato, K.; Adachi, C. Organic Light-Emitting Diodes Employing Efficient Reverse Intersystem Crossing for Triplet-to-Singlet State Conversion. *Nat. Photonics* **2012**, *6*, 253–258.

(26) Uoyama, H.; Goushi, K.; Shizu, K.; Nomura, H.; Adachi, C. Highly Efficient Organic Light-Emitting Diodes from Delayed Fluorescence. *Nature* **2012**, *492*, 234–238.

(27) Liu, M.; Komatsu, R.; Cai, X.; Hotta, K.; Sato, S.; Liu, K.; Chen, D.; Kato, Y.; Sasabe, H.; Ohisa, S.; et al. Horizontally Orientated Sticklike Emitters: Enhancement of Intrinsic Out-Coupling Factor and Electroluminescence Performance. *Chem. Mater.* **2017**, *29*, 8630–8636.

(28) Rajamalli, P.; Senthilkumar, N.; Huang, P. Y.; Ren-Wu, C. C.; Lin, H. W.; Cheng, C. H. New Molecular Design Concurrently Providing Superior Pure Blue, Thermally Activated Delayed Fluorescence and Optical Out-Coupling Efficiencies. *J. Am. Chem. Soc.* **2017**, *139*, 10948–10951.

(29) Chan, C.-Y.; Cui, L.-S.; Kim, J. U.; Nakanotani, H.; Adachi, C. Rational Molecular Design for Deep-Blue Thermally Activated Delayed Fluorescence Emitters. *Adv. Funct. Mater.* **2018**, 1706023.

(30) Byeon, S. Y.; Kim, J.; Lee, D. R.; Han, S. H.; Forrest, S. R.; Lee, J. Y. Nearly 100% Horizontal Dipole Orientation and Upconversion Efficiency in Blue Thermally Activated Delayed Fluorescent Emitters. *Adv. Opt. Mater.* **2018**, *1701340*, 1701340.

Chapter 2

Toolbox of Photoluminescence Spectroscopy

ABSTRACT

In this Chapter, we introduce basic ideas and parameters of photoluminescence spectroscopy with emphasis on experiment. Every section explains a new notion and aims to clarify following questions:

- What is it? Description or definition, units, and physical meaning.
- How to measure it? Experimental techniques and related setups, tips and tricks.
- How to process the data? How to calibrate, normalize, correct, and present graphically.
- What can go wrong? Possible mistakes in measurement and processing. How to avoid / correct / account for them.
- How to analyze the data? Information hidden in the data and corresponding equations, sample parameters to be obtained, and material properties to be revealed.

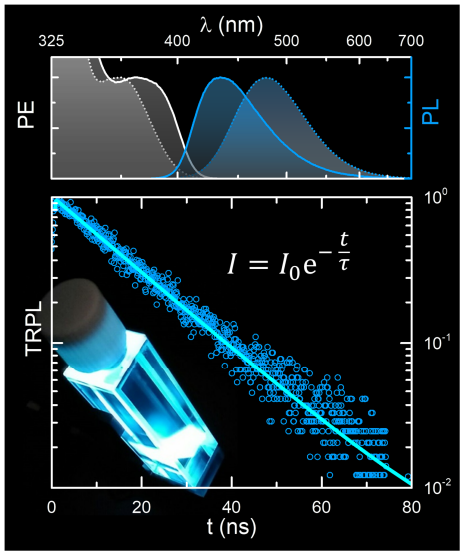

2.1. Optical Spectrum

Interaction of light and matter defines appearance of all objects surrounding us, for example, their color, opacity, and gloss. The way to quantitively describe these properties is to measure how light rays of various colors change after interaction with the matter, which means to record an optical spectrum. Generally, optical spectrum shows energy (wavelength) distribution of photon density or light power. The term *optical* describes physical processes involving visible light plus neighboring ultraviolet and infrared regions. Depending on experimental configuration, a spectrum can describe different steps of light–matter interaction: absorption, transmission, reflection, emission, and so forth.

In following, we consider a modular spectrometer FLS980 as an example of flexible setup for steady-state and time-resolved optical spectroscopy. We acquired the majority of data presented in this Thesis using the FLS980 spectrometer.

The spectrometer has the following main components: four light sources for various purposes, excitation and detection double-grating monochromators, sample chamber, and single-photon detector (see **Figure 2.1**). The setup is computer-controlled.

The continuous xenon arc lamp Xe1 is an excitation source for steady-state spectral measurements. The lamp produces light in a broad spectral region from 250 to 1000 nm.

The compact xenon flashlamp µF2 triggered by the spectrometer controller is optimized for time-resolved measurements in microsecond diapason. The flashlamp has a narrow pulse width of 2–3 µs and an adjustable pulse repetition rate between 0.1 and 100 Hz. Its spectrum covers region from 200 to 950 nm.

The two picosecond laser diodes EPL-375 and EPL-510 are pulsed excitation sources for time-resolved measurements with nanosecond resolution. Here, the resolution is defined by the detection unit and not by the laser pulse width. EPL-375 has wavelength of 375.0 nm and pulse width of 80 ps. EPL-510 has wavelength of 505.2 nm and pulse width of 105 ps. The repetition rate of the lasers is tunable in a broad diapason from 2.5 kHz to 20 MHz. Importantly, the energy of a single laser pulse is the same for all repetition rates.

A monochromator transforms an input light ray containing wide range of wavelengths to an output narrow band around a selected wavelength. The FLS980 spectrometer has two double-grating symmetric monochromators: an excitation monochromator and a detection monochromator. Their double-gratings provide excellent spectral resolution up to 0.02 nm. Each monochromator has two chambers: an upper optical chamber and a lower electrical chamber. The optical chamber is coated with black absorbing paint and sealed against ambient light. Additionally, the chamber is fitted with shields and baffles that minimize reflections of scattered light on shiny surfaces. The electrical and mechanical components controlling the movable parts of monochromator (grating turrets, swing mirrors, shutters, and so on) are placed in the lower chamber. **Figure** 2.1 shows only the schemes of the upper monochromator chambers.

The exit port of the excitation monochromator and the entrance port of the detection monochromator are connected to the central sample chamber, which is subdivided into an upper optical and a lower electronic compartment. Two interlocked ports on top of the sample chamber provide routine access to its interior. Besides the standard holders for liquid and solid samples, the sample chamber permits installation of an integrating sphere and a cryostat. The integrating sphere is optimized for the measurements of photoluminescence quantum yield (see **Section 2.4**). The cryostat allows measurements in vacuum and at low temperatures.

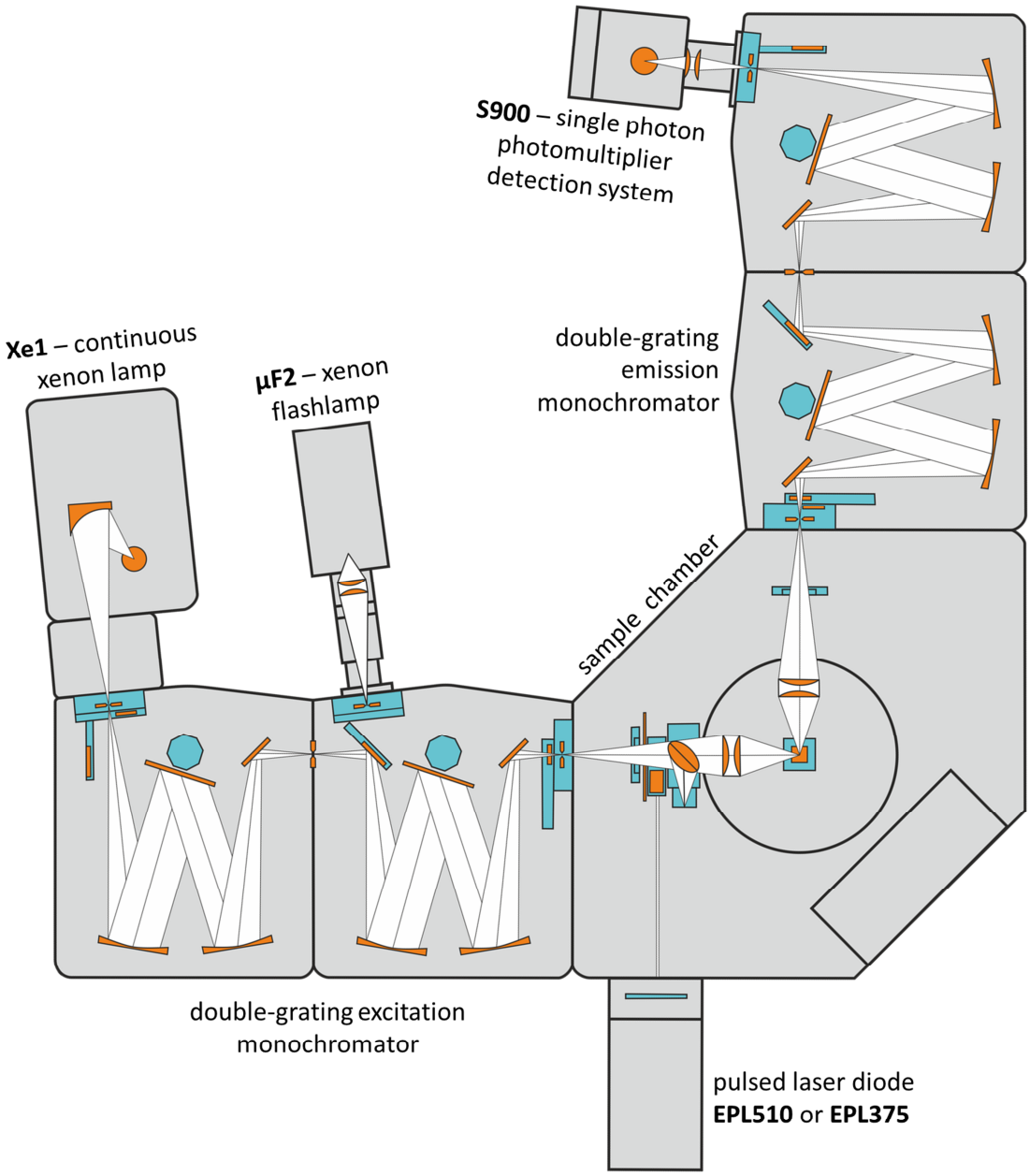

Figure 2.1. Fluorescence spectrometer FLS980 for steady-state and time-resolved measurements.

Two pairs of plano-convex fused silica lenses focus the excitation light onto the sample and collect the emission light. The chamber has two slots for additional optical filters in the excitation and detection arms. A beam splitter in the way of continuous excitation beam diverts its fraction to a reference silicon detector. The output of the reference detector is used to monitor the xenon lamp intensity, to account for optical filters, and to correct photoexcitation spectra (see **Section 2.5**).

The FLS980 includes a high-gain photomultiplier detection system S900 suitable for both steady-state and time-resolved applications. The S900 is designed to operate in the single photon counting mode with spectral sensitivity from 185 to 900 nm. The low noise level in the red region from 670 to 900 nm is provided with a cooled housing that maintains detector temperature at –22°C when the external temperature is 20–25°C.

The detection system S900 includes a side-on type photomultiplier R928, which combines high amplification with low dark-noise level. The multialkali photocathode material determines the R928 quantum efficiency, that is, the ratio of the photon pulses at the output of the photomultiplier in respect to the number of incident photons (**Figure** 2.2). R928 reaches the maximum response at around 400 nm.

However, the sensitivity of the whole spectrometer is defined by the combination of factors such as the efficiency of the monochromators (grating curves), spectral characteristics of the optical components, and brightness of the light sources in the spectral range of interest. For instance, the output signal of Xe1 continuous lamp is rather low below 400 nm, whereas both excitation and detection monochromators cover wavelengths from 200 to 900 nm.

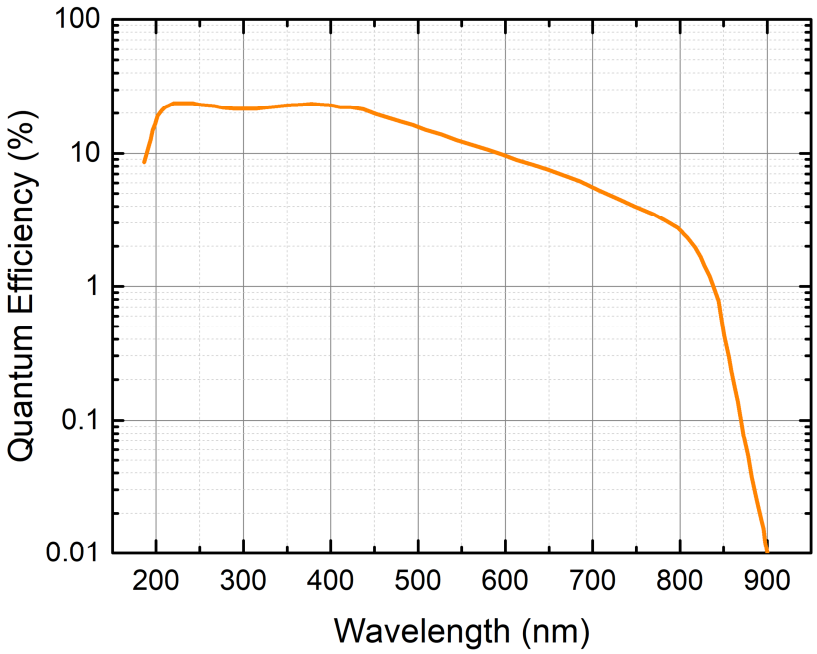

Figure 2.2. Quantum efficiency of the multialkali photocathode for single-photon detection in FLS980.

2.2. Absorption

Atoms and molecules of matter can be excited by light. Such optical excitation is followed by spontaneous relaxation of the excited species back to the ground state. If the excessive energy is disposed radiatively in the form of photons, the process (as well as the resulting emission) is called luminescence. Prior to quantitive study of luminescence, one has to determine the total amount of energy or number of photons absorbed by the sample. Light absorption depends on the wavelength (energy) of the incident photons: the matter opaque in one spectral region can be transparent in another. Absorption spectrum is always material-specific and often sample-specific.

A straightforward way to quantify absorption is to divide the absorbed light intensity, $I_{\text{abs}}(\lambda)$, by the incident intensity, $I_0(\lambda)$:

$$A(\lambda) = \frac{I_{\text{abs}}(\lambda, d)}{I_0(\lambda)} \tag{2.1}$$

Here λ is the wavelength of incident light, d is the sample thickness. The nondimensional coefficient A is sometimes called absorbance.

Experimentally, absorption characteristics are usually derived from the fraction of transmitted light, $I(\lambda, d)$. If the sample does not scatter or reflect, then $I_{\text{abs}}(\lambda, d) = I_0(\lambda) - I(\lambda, d)$ and the absorbance is

$$A(\lambda) = 1 - \frac{I(\lambda, d)}{I_0(\lambda)} \tag{2.2}$$

In a basic measurement, a strongly dilute solution of the studied compound is charged in a quarts cuvette with a square cross-section and placed in the path of a monochromated collimated light beam of wavelength λ. Then $I(\lambda)$ is the intensity of light transmitted by the charged cuvette and $I_0(\lambda)$ is the reference intensity transmitted by the same cuvette filled with pure solvent.

Some authors use the term absorbance interchangeably with the term optical density.[1] Optical density, OD, is defined by the following formula

$$\mathrm{OD}(\lambda) = -\log_{10}\left(\frac{I(\lambda, d)}{I_0(\lambda)}\right) \tag{2.3}$$

Sample thickness is implicit in the definitions of absorbance and optical density: the thick sample has higher absorbance than the thinner one produced of the exact same material. Alternatively, the absorption coefficient, $\alpha(\lambda)$, characterizes a particular medium and is independent of the sample geometry. By definition, the absorption coefficient is the fraction of the light intensity absorbed per a unit length of the medium:

$$\alpha(\lambda) = \frac{dI(\lambda, x)}{I(\lambda, x)} \cdot \frac{1}{dx} \tag{2.4}$$

Integration of **Eq. 2.4** along the sample depth x gives Lambert–Beer law for intensity transmitted through a medium slice of thickness d:

$$I(\lambda) = I_0 \mathrm{e}^{-\alpha(\lambda)d} \tag{2.5}$$

Eq. 2.2, **2.3**, and **2.5** imply following relations between the absorption characteristics for uniform nonscattering nonreflecting samples at linear light propagation:

$$\alpha(\lambda) = \frac{\mathrm{OD}}{d}\ln 10 \tag{2.6}$$

$$\alpha(\lambda) = -\frac{\ln(1-A)}{d} \tag{2.7}$$

A number of additional processes accompany absorption and complicate its measurement in optically dense samples, in particular, in thin films.

Generally, the incident light can be reflected by optical medium, propagate through it, or be transmitted. Naturally, the amount of transmitted light depends on the reflectivity of sample surfaces and on the way light propagates through the sample bulk. In other words, these three general steps of light–matter interaction are bound quantitively.

The light propagation, in turn, includes absorption (followed by PL and sample heating), refraction, and scattering. Refraction reduces the velocity of light propagation compared to free space and causes ray bending at the interfaces, but does not affect the intensity of the incoming light and direction of the rays normal to the sample surface. Thus, one does not need to account for light refraction when measuring absorption. Scattering, on contrary, can introduce significant error in experimental figures, especially for solid samples with non-uniform morphology. Scattering changes the direction of the propagating photons, thus effectively attenuating the incident beam. Nonetheless, the total number of photons leaving the medium is preserved. Therefore, scattering is automatically taken into account by three-dimensional light integration in so-called integrating sphere.

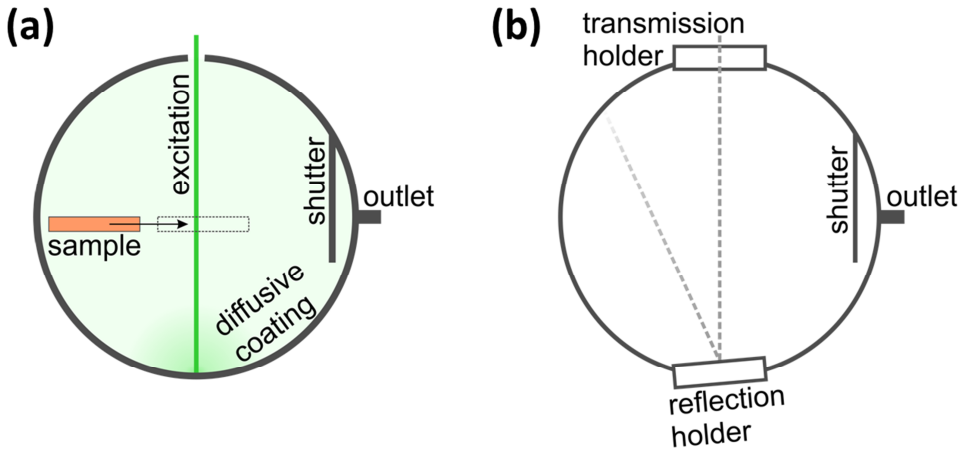

Figure 2.3. Integrating spheres for absorption measurement. (a) Sample is placed inside the sphere so that it can be moved in or out of the excitation ray. (b) Two sample holders are embedded into the sphere walls so that the sample transmits or reflects incident photons to the integrating cavity.

Figure 2.3a shows the basic scheme for absorbance measurement employing an integrating sphere. Integrating sphere is a spherical cavity coated with white material that provides close to unity diffusive reflection in the entire optical region. Therefore, the total amount of photons inside the sphere is preserved while their directions are randomized and the ray collimation is broken.

The entrance aperture permits the monochromated excitation beam inside the sphere. The exit aperture, protected from the collimated rays by a shutter, guides out the resulting integrated emission. The apertures should be much smaller than the sphere diameter not to disturb the light integration.

In the reference measurement, the sample is placed inside the sphere, but out of the way of the excitation beam. One obtains the corresponding reference spectrum by changing the excitation wavelength and recording the output light, $I_0(\lambda)$. Next, the sample is placed directly in the way of the excitation beam. In such configuration, the direct incident light is absorbed. Consequently, the measured output intensity $I(\lambda)$ is lower than $I_0(\lambda)$. Their difference is proportional to the sample absorbance, which can now be calculated with the **Eq. 2.2**.

The measurement with the sample inside the integrating sphere accounts for scattering, reflection, and transmission, but fails to separate them. Consequently, this scheme gives only the absorbance of the sample, A, but not the absorption coefficient of the material, $\alpha(\lambda)$.

Transmission and reflection are quantified by nondimensional coefficients: transmittance, T, and reflectance, R. The transmittance is the ratio of the transmitted intensity to the incident intensity; the reflectance is the ratio of the reflected intensity to the incident intensity. The common source of confusion is whether these coefficients are related to a single surface or to the entire sample. In the following part of this Chapter, we denote the transmittance and reflectance of a surface with τ and ρ, respectively, while T and R describe the entire sample. Energy conservation law bounds the coefficients:

$$\rho + \tau = 1 \tag{2.8}$$

$$R + T + A = 1 \tag{2.9}$$

One can measure R and T and then calculate the absorption coefficient $\alpha(\lambda)$ using the scheme shown at **Figure 2.3b**. Two sample holders are built in the walls of the sphere, so that the sample is in the way of the excitation ray. When the sample is mounted in the front (rear) holder, all transmitted (reflected) photons are directed into the integrating cavity.

In the reference measurement, $I_0(\lambda)$, the transmission holder is empty and the reflection holder is blocked with a diffusive plate. The transmitted and reflected intensity, $I_T(\lambda)$ and $I_R(\lambda)$, are measured with the sample in the front and rear holder, respectively. Then $T = I_T/I_0$, $R = I_R/I_0$, and $A = 1 - I_T/I_0 - I_R/I_0$. Here and in the following formulas, we drop (λ) for clarity, still implying that all characteristics are spectral.

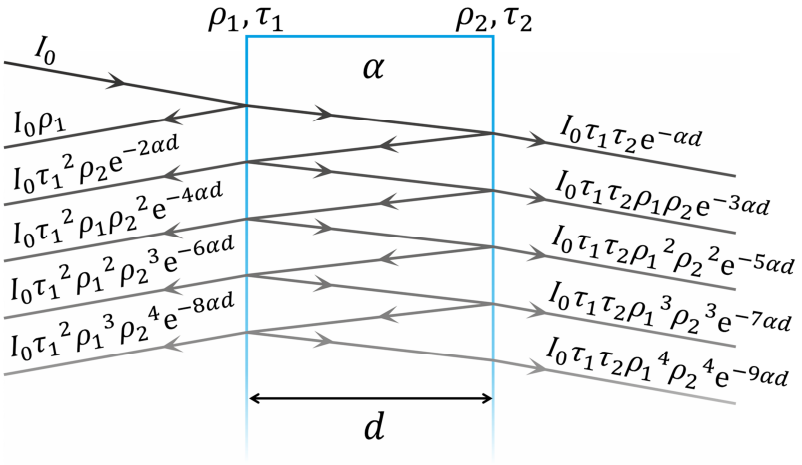

Figure 2.4. Multiple reflections and transmissions of incident ray I_0 in a uniform parallel-sided plate where interference effects are negligible.

Now, we can connect the measured coefficients T and R with the surface characteristics ρ and τ and absorption coefficient α. Let us consider a parallel-sided plate made of a uniform material (**Figure 2.4**). We assume that the plate is thick enough ($d \gg \lambda$), so that interference is negligible. A normal incident ray of intensity I_0 undergoes multiple reflection and transmission events at the sample surfaces and is partially absorbed in the sample bulk. **Figure 2.4** shows nonzero incident angle for clarity of representation. Nonetheless, all further equations are derived for the beams perpendicular to the sample.

Infinite sum of geometric progression for subsequent reflection and transmission events results in the following formulas for total transmittance, reflectance, and absorbance of the sample:

$$R \equiv \frac{I_R}{I_0} = \frac{\rho_1 + \rho_2 e^{-2\alpha d} - 2\rho_1\rho_2 e^{-2\alpha d}}{1 - \rho_1\rho_2 e^{-2\alpha d}} \tag{2.10}$$

$$T \equiv \frac{I_T}{I_0} = \frac{(1-\rho_1)(1-\rho_2)e^{-\alpha d}}{1 - \rho_1\rho_2 e^{-2\alpha d}} \tag{2.11}$$

$$A \equiv 1 - \frac{I_R}{I_0} - \frac{I_T}{I_0} = \frac{(1-\rho_1)(1-\rho_2 e^{-\alpha d})(1-e^{-\alpha d})}{1 - \rho_1\rho_2 e^{-2\alpha d}} \tag{2.12}$$

Here we also used **Eq. 2.8** and **2.9**. The plate thickness d is measured separately, for example, with a caliper. R and T are measured directly in the integrating sphere.

The two independent **Eq. 2.10** and **2.11** contain 3 variables: ρ_1, ρ_2 and α. For a uniform plate with air on either side, $\rho_1 = \rho_2 \equiv \rho$, from considerations of symmetry. Only then the surface reflectance ρ and the absorption coefficient α can be numerically extracted from **Eq. 2.10–2.11**. However, in the common case of absorbing thin film deposited on a glass substrate, the reflectance at material–air interface differs from that at material–substrate interface ($\rho_1 \neq \rho_2$). Therefore, additional measurements or approximations are necessary to determine absorption coefficient in layered samples.

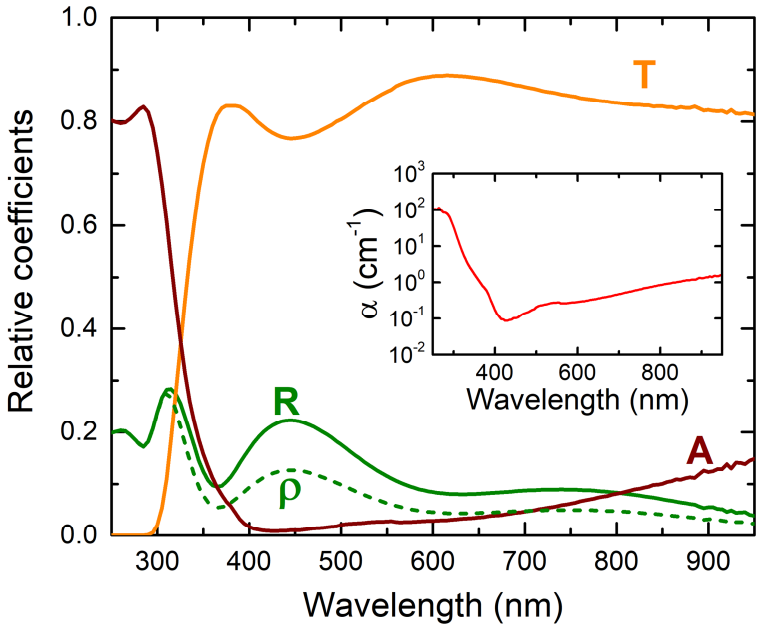

Figure 2.5. Reflectance R, transmittance T, and absorbance A of a lab-glass slide measured in the integrating sphere. The dashed line shows reflectance at the glass–air interface. Inset: the glass absorption coefficient.

First, one measures reflectance R_S and transmittance T_S of the bare substrate in the integrating sphere and calculates the reflectance at the substrate–air interface, ρ_S, and the absorption coefficient, α_S, using **Eq. 2.10–2.11** (see **Figure 2.5**). Then the substrate covered with the absorbing film is measured in three configurations. First, the sample is in the transmittance holder (T_{MS}). Second, the sample is in the reflectance holder while the absorbing material is facing the incoming beam (R_{MS}). Third, the sample is in the reflectance holder while the substrate is facing the incoming beam (R_{SM}). The approximate formula for each configuration writes

$$T_{MS} \approx (1-\rho_M)(1-\rho_{MS})(1-\rho_S)e^{-\alpha_M d_M} e^{-\alpha_S d_S} \quad (2.13)$$

$$R_{MS} \approx \rho_M + (1-\rho_M)^2 \rho_{MS} e^{-2\alpha_M d_M} \quad (2.14)$$

$$R_{SM} \approx \rho_S + (1-\rho_S)^2 \rho_{MS} e^{-2\alpha_S d_S} \quad (2.15)$$

Here we neglect multiple subsequent reflections and transmission events and consider only the major addends. As follows from **Eq. 2.13**, the front sample side for transmittance measurement does not matter to the first approximation. Material and substrate thicknesses, d_M and d_S, are measured separately. Reflectance at the substrate–air interface, ρ_S, and the substrate absorption coefficient, α_S, are determined in the preceding measurement. Therefore, the 3 independent **Eq. 2.13–2.15** contain 3 unknown values: the reflectance at material–air interface, ρ_M, the reflectance at material–sample interface, ρ_{MS}, and the absorption coefficient of the material, α_M. Now, the last can be expressed numerically from the system of **Eq. 2.13–2.15**. This approach was used for perovskite thin films in **Chapter 5** of this Thesis.

Alternatively, one can make additional assumptions about a layered sample in order to directly apply **Eq. 2.10–2.11**. For example, if the studied material and substrate are both highly transparent (region of low absorption), one can estimate the reflectance at the interfaces between the two media using their refractive indices:[1]

$$\rho_{\mathrm{MS}} \approx \left(\frac{n_{\mathrm{M}} - n_{\mathrm{S}}}{n_{\mathrm{M}} + n_{\mathrm{S}}}\right)^2 \tag{2.16}$$

For glass, quartz or sapphire substrates, α_{S} can be put to 0 in optical region. However, one should be careful with any approximations near to the edge of absorption spectrum, because optical constants of the material may change abruptly in that region.

2.3. Photoluminescence

Photoluminescence (PL) is a radiative release of photoinduced material excitation. PL normally takes place at lower energies than absorption. In other words, material emission spectrum is shifted toward the red wavelengths compared to its absorbance spectrum. The physical reasons for this red shift will be discussed in **Chapter 3**.

The PL spectrum can be recorded with a spectrometer or spectrograph. The spectrometer contains movable turret with gratings, so that emission at subsequent wavelengths strikes the narrow vertical output slit while the turret is rotating (see **Section 2.1**). On contrary, the spectrograph presents the entire spectrum at once at the extended horizontal output slit. Spectrograph offers the advantage of prompt measurement and is more stable because of its immobile gratings, but requires an array of photodetectors or a CCD camera in order to record the result. Spectrometer offers better spectral resolution and improved signal-to-noise ratio, but requires precise control of the turret rotation.

Unlike absorption, a correct luminescence measurement implies calibration of both X– and Y–axes. Indeed, absorption is by definition a relative characteristic: one always normalizes the transmitted intensity by the reference intensity of the source at the same wavelength. In contrast, PL is proportional to absolute emission flux per unit spectral step.

First of all, a PL spectrum presented on wavelength scale is different from that presented on energy scale.[2] Indeed, $S(\lambda)d\lambda = S(\varepsilon)d\varepsilon$, because the total amount of emitted energy per corresponding segments $d\lambda$ and $d\varepsilon$ cannot depend on the scaling. Then, taking into account that $\lambda = hc/\varepsilon$, we obtain:

$$S(\varepsilon) \propto \lambda^2 S(\lambda) \tag{2.17}$$

$$S(\lambda) \propto \varepsilon^2 S(\varepsilon) \tag{2.18}$$

Thus, showing both wavelength and energy axes for one curve is, strictly speaking, incorrect. Experimentally, the spectra are usually recorded on wavelength scale. At the same time, energy scale is more convenient for analysis.

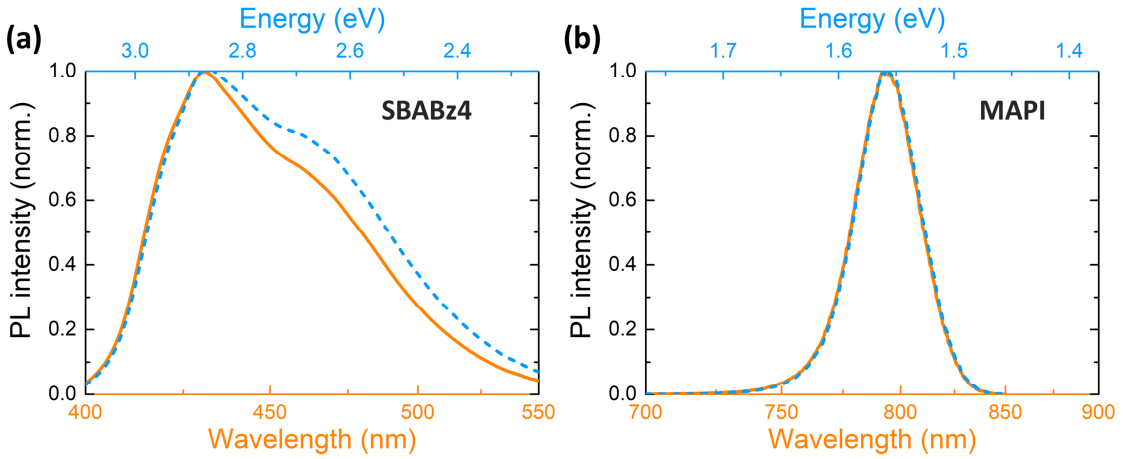

Figure 2.6. PL spectra of deep-blue organic emitter SBABz4 (a) and low-gap organo-metal-halide perovskite MAPI (b). Wavelength scale corresponds to the orange solid curves, energy scale to the dashed blue ones.

Fortunately, the deviation expressed by **Eq. 2.17–2.18** is small in optical region and becomes negligible for larger wavelengths (see **Figure 2.6**). Therefore, the complimentary energy axis is frequently shown in literature as a guide for the eyes. At that, one of the axes in the frame is linear, the other is reciprocal, because $\lambda \propto 1/\varepsilon$. We also sometimes use such double scaling in this Thesis.

Second, Y–axis should be properly calibrated and scaled in order to provide correct spectral shape. A light source with a known broad emission spectrum, $S_{\text{true}}(\lambda)$, is required for spectral calibration of an optical setup. One obtains a calibration curve, $\kappa(\lambda)$, dividing the actual spectrum, $S_{\text{true}}(\lambda)$, by that recorded in the setup, $S_{\text{recorded}}(\lambda)$:

$$\kappa(\lambda) = \frac{S_{\text{true}}(\lambda)}{S_{\text{recorded}}(\lambda)} \tag{2.19}$$

Afterwards, one can calculate a corrected spectrum for every new compound as a product of its recorded emission and the calibration curve, $\kappa(\lambda)$. In such way, PL spectra of the same compound measured with different calibrated setups have the same shape.

PL measurements rarely require more demanding calibration of Y–axis in absolute photometric units. Instead, spectra presented in arbitrary units (a.u.) suffice for PL efficiency analysis, whereas those normalized to their maximum value reveal energetics of the excited species. Nonetheless, the units chosen for setup calibration affect even the shapes of arbitrary or normalized PL spectra. Namely, the detected emission is proportional whether to irradiation intensity, whether to photon flux. The default units for every setup are defined by the reference spectrum of the calibration source. For example, the calibrated spectrometer FLS980 used in the current work produces spectra proportional to photon flux. Representation of PL spectra in photon units is necessary to determine photoluminescence quantum yield (see **Section 2.4**). One can easily transform intensity to photon representation by dividing the curve to photon energy (or multiplying by wavelength). **Figure** 2.7 shows calibration curves of FLS980 for irradiation intensity and for photon flux.

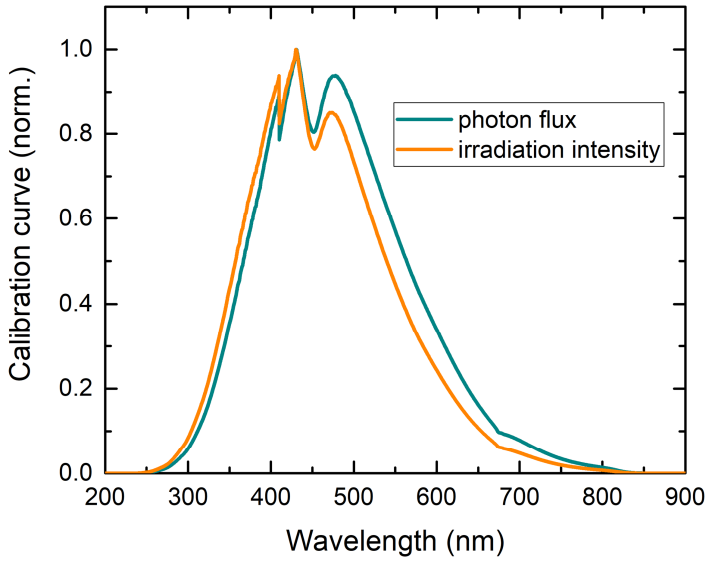

Figure 2.7. Calibration curves for emission in FLS980 spectrometer. Steps at 410 and 675 nm correspond to automatic exchange of neutral density filters in the detection arm.

2.4. Photoluminescence Quantum Yield

The number of emitted PL photons divided by the number of absorbed photons is called photoluminescence quantum yield (PLQY). PLQY is a quantitive measure for efficiency of radiative material relaxation versus nonradiative.

There are several established relative[3] and absolute[4–6] methods for experimental determination of PLQY. In this Thesis, we applied a widely used measurement of PLQY in the integrating sphere.[7] This purely optical method requires no additional material parameters and no fluorescence standard. The PLQY measurement in the integrating sphere is suitable for both liquid and solid samples, including highly scattering and refractive ones.

Figure 2.8 shows three experimental configurations and the corresponding spectra needed to determine PLQY of one sample. For the sake of simplicity, we use in this sketch the computer-generated Gaussian curves instead of actual experimental spectra. In the measurement (a), the excitation beam passes through the empty sphere. In the measurement (b), the sample is in the sphere but out of the excitation beam, so that only the diffused light reaches the sample. In the measurement (c), the sample is placed directly in the way of the collimated excitation beam.

Two portions of emission contribute to the resulting spectra: a narrow peak from the laser (lamp) and a broader red-shifted PL from the sample. The integral under each part is proportional to the density of excitation photons or sample PL. We will denote those integrals as L and P, respectively, whereas the subscripts a, b or c will denote experimental configuration. Calibrated Y–axis is critical for the correct integration. All spectra must be proportional to the photon flux at a given wavelength interval (see **Section 2.3**).

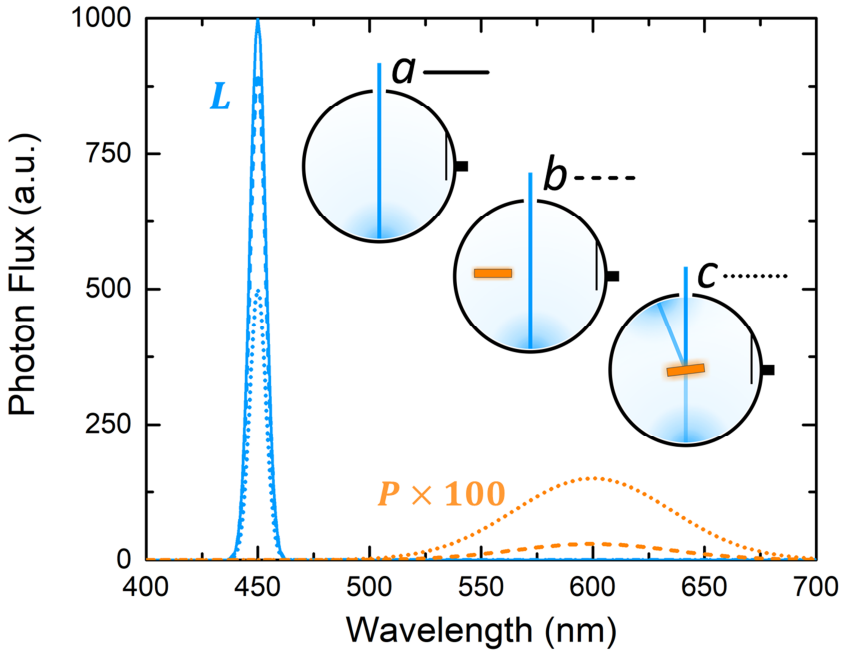

Figure 2.8. Scheme of PLQY measurement in the integrating sphere and the corresponding spectra. Excitation is shown in blue color, emission (magnified by a factor 100) in orange. Solid, dashed, and dotted lines refer to different experimental configurations (see the sketch in the inset).

Configuration (a) serves as a reference to determine the photon density. In the measurement (b), the laser peak is lower, because a fraction μ of scattered excitation photons is absorbed by the sample:

$$L_b = L_a(1-\mu) \tag{2.20}$$

In the configuration (c), the directly illuminated sample absorbs an additional fraction A of the excitation photons:

$$L_c = L_a(1-A)(1-\mu) \tag{2.21}$$

Note that the coefficient A coincides with the sample absorbance only if the cross-section of the incident beam is smaller than the sample area. Otherwise, a part of the collimated excitation beam passes by the sample without interaction. In any case, the shape of the normalized curve $A(\lambda)$ follows the normalized absorbance spectrum.

The total amount of photons leaving the integrating sphere in the measurement (b) is $(L_b + P_b)$. The direct absorption of the collimated beam lowers this amount in the configuration (c). Therefore, the first portion of the diffused light leaving the sphere in the experiment (c) amounts to $(1-A)(L_b + P_b)$. Additionally, the direct sample illumination causes PL emission whose quantum efficiency is defined by the sample PLQY. Thus, the other portion of the diffused light leaving the sphere in the experiment (c) is $(\mathrm{PLQY} \cdot AL_a)$. Now, the total photon flux detected in the configuration (c) is

$$L_c + P_c = (1-A)(L_b + P_b) + \mathrm{PLQY} \cdot AL_a \tag{2.22}$$

Eq. 2.20 and **2.21** give simple expressions for the coefficients $\mu = 1 - L_b/L_a$ and $A = 1 - L_c/L_b$. With that, the PLQY of the sample is:

$$\mathrm{PLQY} = \frac{P_c - (1 - A)P_b}{AL_a} \tag{2.23}$$

If the absorption of diffused light at the given wavelength is low ($L_a \approx L_b$), the measurement (b) can be omitted. Then, the **Eq. 2.23** simplifies to

$$\mathrm{PLQY} = \frac{P_c}{L_a - L_c} \tag{2.24}$$

Sample holders, substrates, and imperfections of the sphere coating often result in the parasitic additional absorption and background emission. Thus, one should place the sample holder and substrate inside the sphere in the measurement (a), in order to account for their absorption and to record the background signal, P_a. The background emission must be then subtracted from the total recorded PL (P_b and P_c).

Figure 2.9 shows an example of PLQY measurement of a thin amorphous film of organic emitter SBABz4 (see **Chapter 6**). Here, we used high excitation power and omitted the measurement (b), because the absorption of the thin film was very weak at 360 nm. Logarithmic scale demonstrates the large difference between the magnitudes of the excitation and emission spectra. Spectral measurements in such broad dynamic diapason usually require judicious use of optical filters. Note that there is a parasitic background emission (the dotted line in the PL region) that presumably comes from the glass substrate. PLQY of the sample presented at **Figure 2.9** is $(40 \pm 3)\%$. PLQY determination of blue emitters is especially challenging, because they absorb well only in the ultraviolet region.

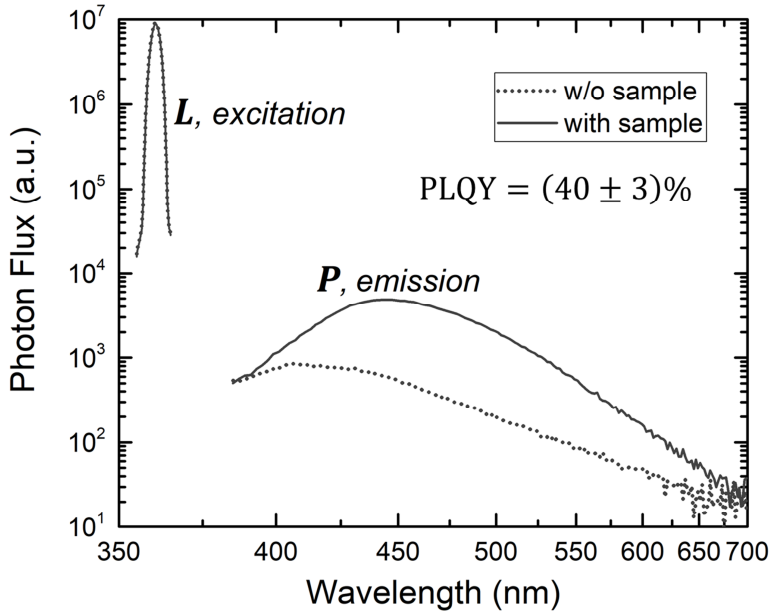

Figure 2.9. Spectra used to determine PLQY of an amorphous film SBABz4 in the integrating sphere: peaks of continuous xenon lamp with and without sample, parasitic background emission, and PL from the sample.

PLQY is normally independent of the excitation wavelength (Vavilov rule).[8] Therefore, light of any wavelength can be used to measure PLQY, as long as the sample has reasonable absorption in this region. Additionally, PL spectra are independent of the excitation wavelength (Kasha rule).[9] The both rules steam from the fast vibrational relaxation, which will be discussed in **Chapter 3**. At the same time, PLQY of various materials and material systems depends (sometimes nonlinearly) on the excitation power. This dependence is due to the second- and higher-order recombination processes and is actively exploited in perovskite research.[10–12]

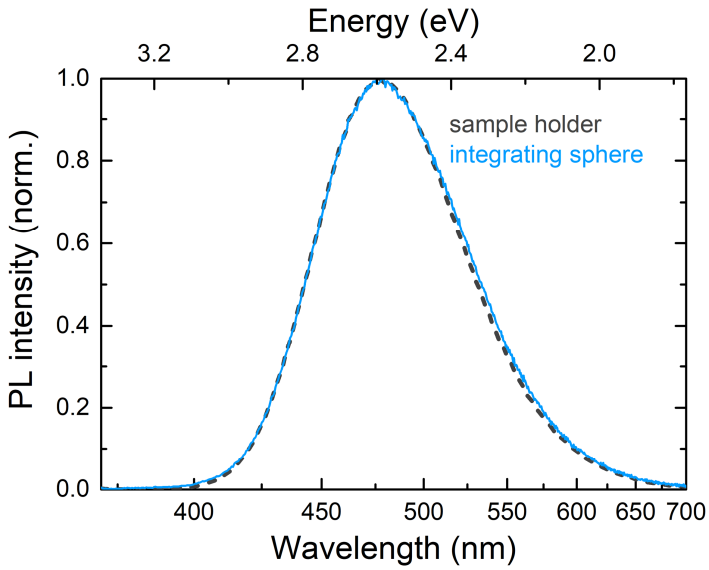

Figure 2.10. PL spectra of SBABz4 dilute solution when cuvette is placed in a standard sample holder (dashed black line) or inside the integrating sphere (solid blue line).

Some authors claim that integrating sphere increases self-absorption,[7] that is, absorption of PL photons by the emitter itself (see **Chapter 5**). We would like to point out that solid samples that require measurement in the integrating sphere are naturally prone to self-absorption: they have high refractive index and provoke waveguide effect. The integrating sphere collects all PL, including the one that comes from the film edges and is strongly distorted after passing through the material. Therefore, the resulting PL spectrum of a solid highly-refractive sample may differ from that recorded in the standard sample holder in a transmission mode or in 45-degree geometry. In contrast, PL of dilute solutions and amorphous films with low refractive index shall be unaltered by the properly calibrated integrating sphere (**Figure 2.10**).

2.5. Photoexcitation

Almost every emissive sample includes additional absorbing media: solvent, impurities, polymeric matrix, substrate, electrodes, and so forth. They add parasitic bands to the absorption spectrum. Thus, analysis of samples with absorbing admixtures requires more

selective technique than the standard absorption spectroscopy. For instance, one can detect emission from the studied material at an arbitrary fixed wavelength while varying the excitation wavelength. The resulting photoexcitation (PE) spectrum separates the absorption that causes luminescence from the background one. In some sense, PE is an inversed PL measurement, in which the excitation wavelength is fixed while the detection is scanned. **Figure 2.11** schematically illustrates the reciprocity of PE and PL. Note that the resulting PE and PL spectra for the organic dye mirror each other when shown on energy scale. Molecular emitters frequently follow the mirror symmetry rule that results from the symmetry of excitation and relaxation in organic semiconductors (see **Chapter 3**).

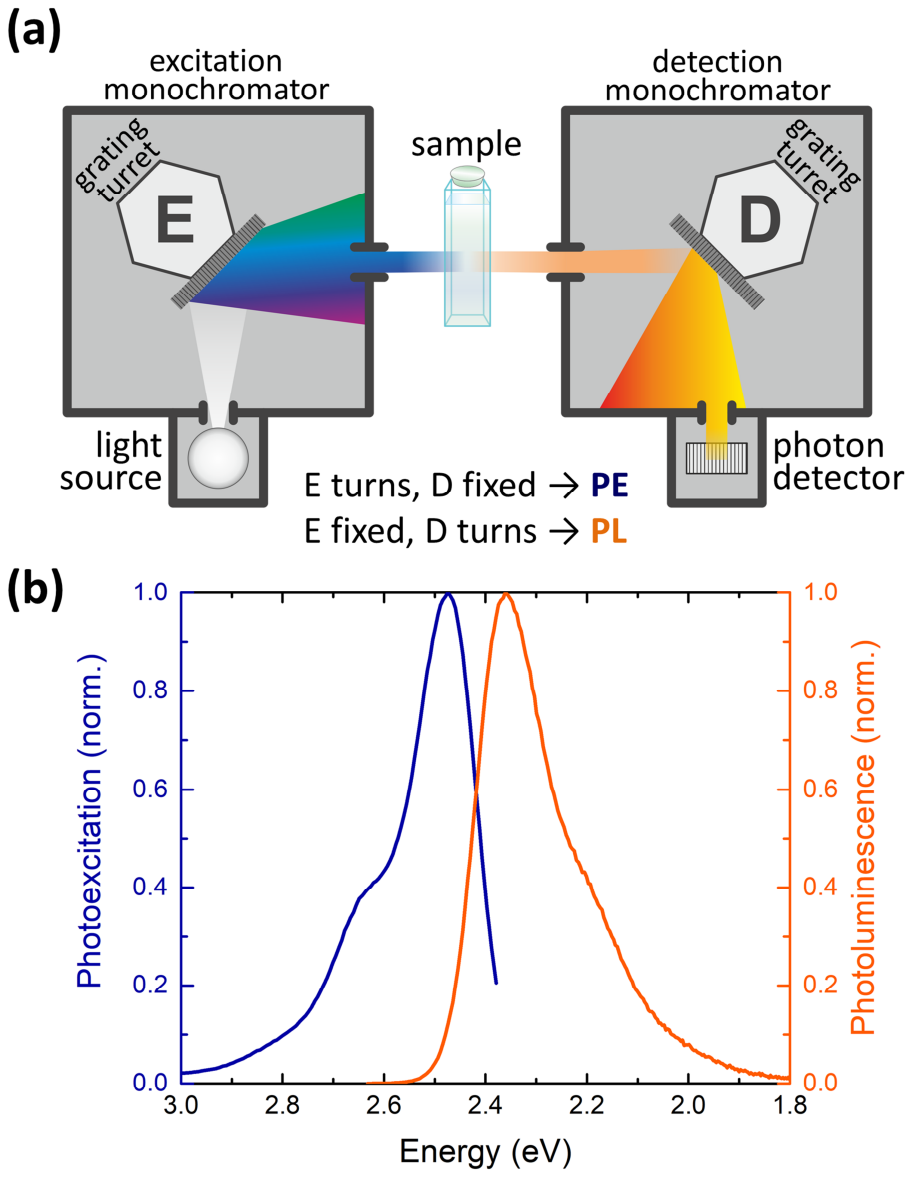

Figure 2.11. (a) Simplified scheme of excitation and detection for PE and PL measurements. The excitation turret E turns and the detection turret D is fixed for PE spectrum, whereas E is fixed and D turns for PL spectrum. (b) PE and PL spectra for dilute solution of the red fluorescein derivative, FAM. The energy scale emphasizes the mirror symmetry of the spectra.

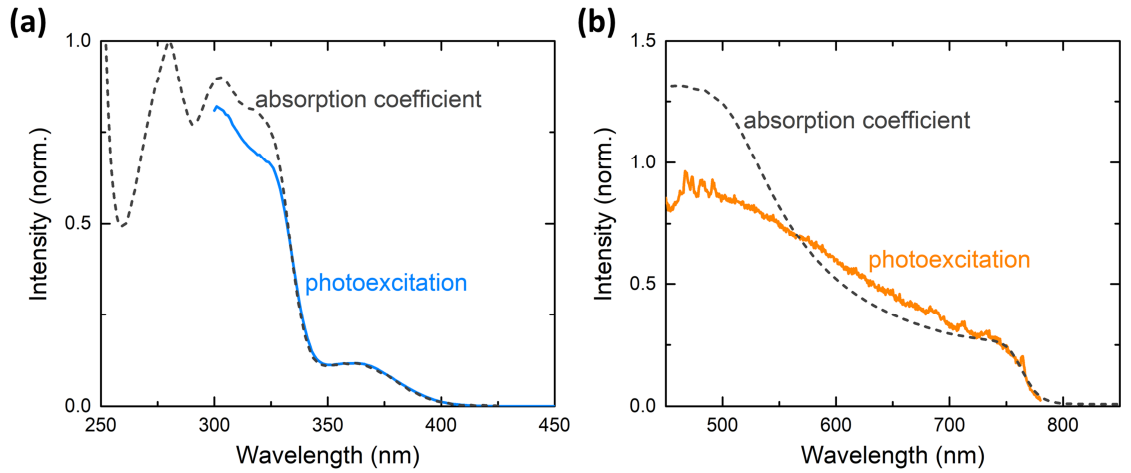

Figure 2.12. Comparison of absorption (dashed black lines) and PE (solid colored lines) for an amorphous film of organic emitter SBABz4 (a) and for a thin polycrystalline MAPI film (b).

The idea of PE spectroscopy is based on Vavilov rule: quantum yield of emission is independent of the excitation wavelength.[8] The photon density of excitation should remain constant at every wavelength, in order to provide a correct PE spectrum. Considering that no real source produces constant emission at every wavelength, one should always divide the detected photon flux from the sample to the measured photon flux of the source.

The wavelength-dependent reflectance in the region of interest also distorts PE spectrum. Therefore, PE is beneficial only for solutions and amorphous films, whereas anisotropic crystalline samples require complete analysis of transmittance, reflectance, and absorbance (see **Section 2.2**). **Figure 2.12a** shows that the properly corrected PE spectrum of an amorphous thin film coincides with the corresponding absorption spectrum down to 320 nm, where the parasitic substrate absorption emerges. On contrary, PE does not follow the absorption coefficient of a polycrystalline MAPI film for its main part (**Figure 2.12b**), because of the strong wavelength-dependent perovskite reflection.

2.6. Time-Resolved Photoluminescence

Excited state population in most materials relaxes back to the ground state almost immediately after the excitation light has been switched off. The quickly decaying PL that accompanies such process carries important information about the excitation dynamics within the material. The detection of time-resolved PL (TRPL) is challenging because of vast material diversity. Namely, TRPL lifetimes vary from several picoseconds to several seconds, that is, within 12 orders of magnitude. Additionally, the long living TRPL often includes important prompt features that require excellent time resolution, up to 10^{-6} of the entire time window (see **Chapter 6**). The long portion of PL is usually less intense than the prompt one. Therefore, TRPL signal containing several components covers several orders of magnitude in intensity. Thus, one has to find a compromise between the sensitivity and acquisition time. All in all, TRPL requires expert operation of advanced setups.

There are two general approaches to TRPL detection: streak camera imaging and time-correlated single-photon counting (TCSPC). Both approaches offer a number of technical advantages and both allow detection of TRPL for a broad range of lifetimes with sufficient time resolution. In this Thesis, we mainly applied TCSPC. For comparison, however, we will now briefly discuss the streak camera imaging.

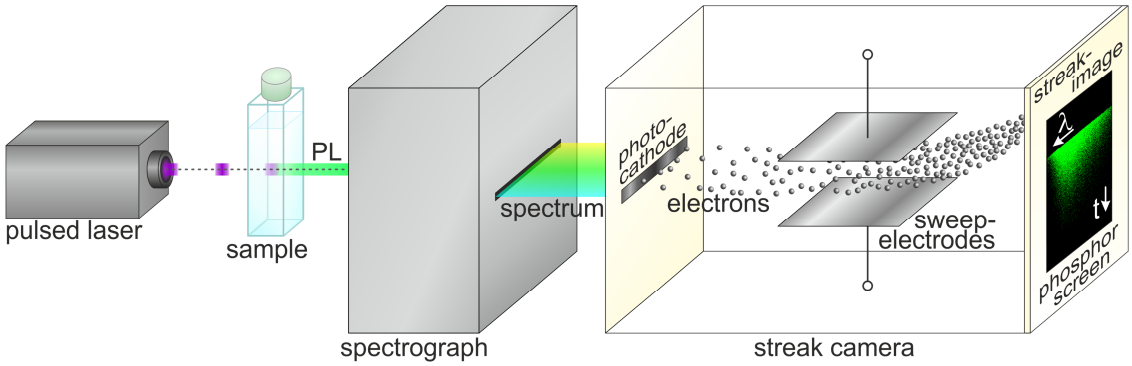

Figure 2.13. A scheme of the streak camera imaging. For clarity, we show only the essential elements.

Streak camera produces two-dimensional PL maps. Each horizontal cross-section of such map gives a spectrum at a certain stage of PL decay, whereas each vertical cross-section shows PL decay curve at an arbitrary wavelength. The spectral resolution for streak camera is usually provided by a spectrograph (**Figure 2.13**). The spectrograph transforms PL emission caused by a laser pulse into a horizontal spectrally resolved ray. Streak camera then uses photoelectric effect in order to convert this light into a flux of electrons, which can be manipulated by the fast electric field changing in the vertical direction. Namely, the electrons pass between two sweep electrodes that decline them with a linearly decreasing voltage. The electrons that arrive to the sweep electrodes first, will be declined to the greater angles than those arriving later. Altogether, streak camera working principle is similar to that of an electronic oscilloscope.

The alternative mode of transient PL measurements — TCSPC — was realized within FLS980 spectrometer (see **Section 2.1**). **Figure 2.14** shows a basic working scheme of the TCSPC. A short excitation pulse strikes the sample and initiates PL. At the same time, a trigger signal comes from the laser to start a time counter. The PL emission passes through a spectrometer that selects a narrow band around a desired wavelength. The PL signal is rendered low, for example, by a neutral density filter, so that only one photon leaves the spectrometer after each excitation event. The monochromated PL photon serves as a stop pulse for the time counter. Therefore, a certain delay between the excitation and emission moments is assigned to each detected photon. A distribution of these delays for large number of excitation–emission events gives the PL decay curve. In fact, the TCSPC is a fast stopwatch for PL photons. TCSPC profits from the excellent sensitivity of single-photon detector and spectral resolution of double-monochromator. On the other hand, the streak-camera imaging is much faster, because it immediately produces a two-dimensional PL map.

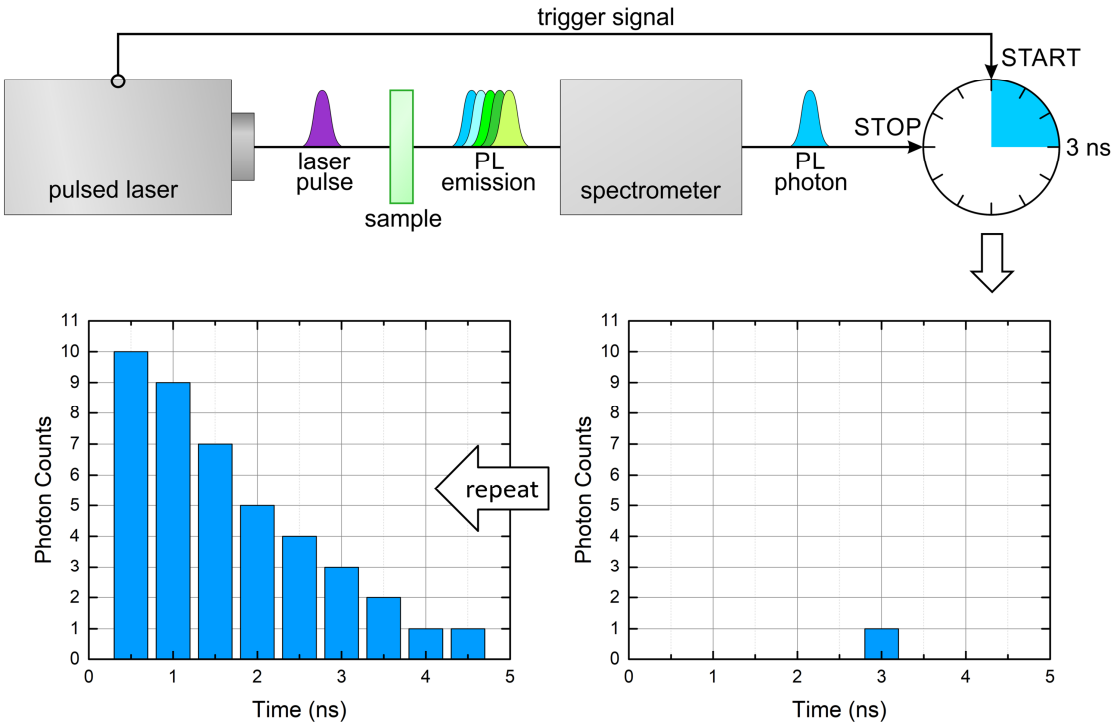

Figure 2.14. A scheme of time-correlated single-photon counting (TCSPC).

The TRPL detection is a statistical Poisson process, because it involves counting discrete independent events (spontaneous emission of photons) occurring in a fixed interval of time (between two excitation pulses). Such measurements require large number of repetitions (sweeps) in order to record a TRPL curve with an acceptable signal-to-noise ratio. The high signal-to-noise ratio can be attained by high signal intensity in one repetition, as well as by large number of repetitions. Experimentally, though, the large number of repetitions is preferable, because the high signal intensity leads to erroneous TRPL curves.

Figure 2.15 simulates how the overly high signal intensity distorts TRPL both for streak camera imaging and for TCSPC. The gray lines here show the exponential fits for PL decay; the blue symbols show the correctly detected signal; the orange symbols show the distorted measurement of the same PL. Note that we refer to the emission intensities that are still not damaging for the equipment.

The high PL intensity causes dense electron flux inside the streak camera. Thus, two or more electrons can strike approximately the same position at the phosphorous screen and appear as only one count. Consequently, the peak of PL decay curve will be smoothed, whereas the shape of its tail will be preserved (**Figure 2.15**a). The high PL intensity in TCSPC causes more than one photon to leave the spectrometer after a single excitation event. Only the first of them will serve as a stop pulse for the time counter while the others will be neglected. Therefore, the detected curve will appear steeper than the actual PL decay (**Figure 2.15**b).

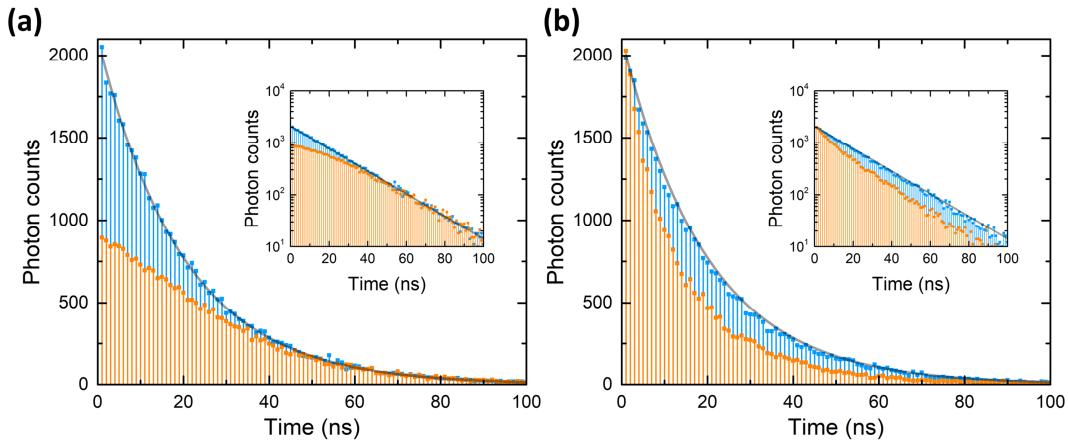

Figure 2.15. TRPL curves simulated according to the principles of streak camera imaging (a) and TCSPC (b). The PL intensity in one sweep is 10 times higher for orange curves than for the blue ones. The 10 times longer acquisition time for the blue curves equalizes the total photon statistics. Note how the overly high signal intensity distorts the shape of the orange curves in both measurements. Gray lines show the corresponding monoexponential decay with the lifetime of 20 ns. The insets show the same curves on a semilogarithmic scale.

We used a monoexponential PL decay for the simulation in **Figure 2.15**:

$$I(t) = I_0 \mathrm{e}^{-\frac{t}{\tau}} \tag{2.25}$$

Here I_0 is the initial PL intensity and τ is the characteristic PL lifetime. The monoexponential PL decay appears as a straight line on a semilogarithmic scale (see the insets in **Figure 2.15**). Such decay shape is frequently encountered in the TRPL experiments. It is characteristic for organic emitters isolated, for example, in a dilute solution or in an inert amorphous matrix (see **Chapter 6**). The monoexponential PL decay also signifies well-ordered organic systems, such as molecular crystals with low defect density. TRPL from inorganic materials can also appear as a straight line on a semilogarithmic scale, as long as the material is heavily doped. Nonetheless, the monoexponential decay is not the only possible shape of the TRPL signal. In the experimental chapters of this Thesis, we will deal with the complex recombination processes resulting in more exotic TRPL curves, which are not always expressed analytically.

The characteristic PL lifetime is connected with PLQY via a number of rate constants. In fact, the combined measurements of the lifetime and quantum yield can be used to derive the rates of carrier recombination, intramolecular transitions, and excitation transfer within the material. For the monoexponential decay, PLQY is directly proportional to the lifetime:

$$\mathrm{PLQY} = k_{\mathrm{rad}}\tau \tag{2.26}$$

Here k_{rad} is the radiative recombination rate. Unfortunately, one cannot apply the simple **Eq. 2.26** for the materials that involve up-conversion processes or energy transfer. We will elaborate **Eq. 2.26** and more general connection of lifetime and PLQY, as well as some special cases in the following chapters.

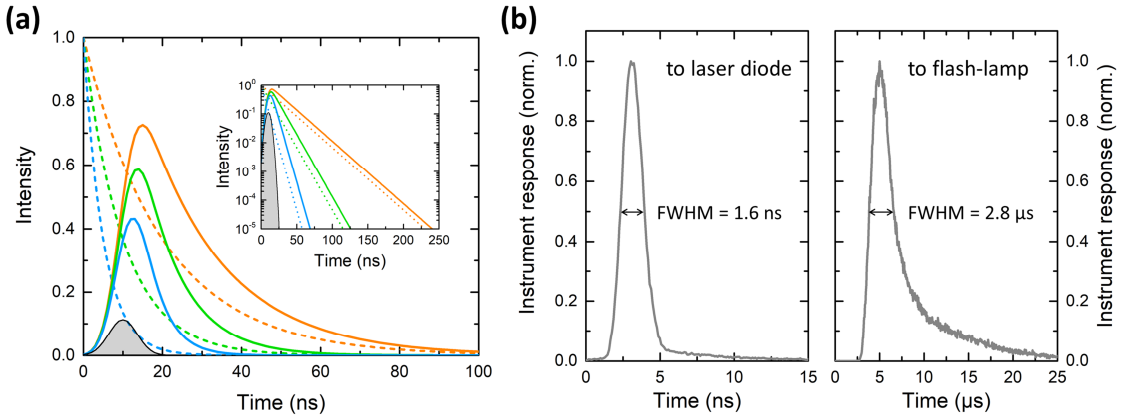

Figure 2.16. (a) Convolution of the monoexponential decay curves (dashed lines) with the Gaussian instrument response function (gray peak, FWHM = 5 ns). Blue, green, and orange decay curves have lifetimes of 5, 10, and 20 ns, respectively. The solid lines of the respective colors show the resulting signal. Inset: the same curves on a semilogarithmic scale. (b) Instrument response of FLS980 to the picosecond laser diode and microsecond flashlamp measured in TCSPC mode.

Prior to quantitative analysis of a PL decay curve, one has to make sure that its features are accurately resolved in the experiment. Time resolution of a TRPL setup is the minimum interval between two short pulses that appear in the measurement as two separate peaks. The shorter is this time interval, the faster decay can be recorded. As follows from the definition, the time resolution is determined by the broadening of the delta-like input pulse at the setup output, that is, by the instrument response function of the setup. The signal that appears in the TRPL experiment, $S(t)$, is the convolution of the instrument response function, $IRF(t)$, and the actual decay, $PL(t)$:

$$S(t) = IRF_{\text{norm}}(t) \otimes PL(t) \equiv \frac{\int_{-\infty}^{+\infty} IRF(\theta) \cdot PL(t-\theta)d\theta}{\int_{-\infty}^{+\infty} IRF(\theta)d\theta} \qquad (2.27)$$

Note that **Eq. 2.27** includes normalization of the IRF to its area.

Figure 2.16a shows how a Gaussian IRF with full width at half-maximum (FWHM) of 5 ns changes the monoexponential decay curves with the lifetimes of 5, 10, and 20 ns. First, the IRF postpones the curve rise. The magnitude of the delay depends both on the PL lifetime and on the IRF shape. Second, the convolution with IRF lowers the magnitude of the signal, but preserves the information about its lifetime. Notice that the decreasing parts of the initial and distorted signals are parallel on the logarithmic scale (respective dashed and solid lines in the inset of **Figure 2.16a**).

Experimentally, one can estimate the IRF as a decay of a very short input signal, for example, a pulse from the excitation source. In **Figure 2.16b**, the instrument response to the picosecond laser EPL-510 broadens mostly because of the finite response time of the optical and electrical components within the setup. The instrument response to the microsecond flashlamp µF2 is mostly defined by the pulse width of the source itself. In this Thesis, we chose the excitation source according to the PL lifetime of the sample.

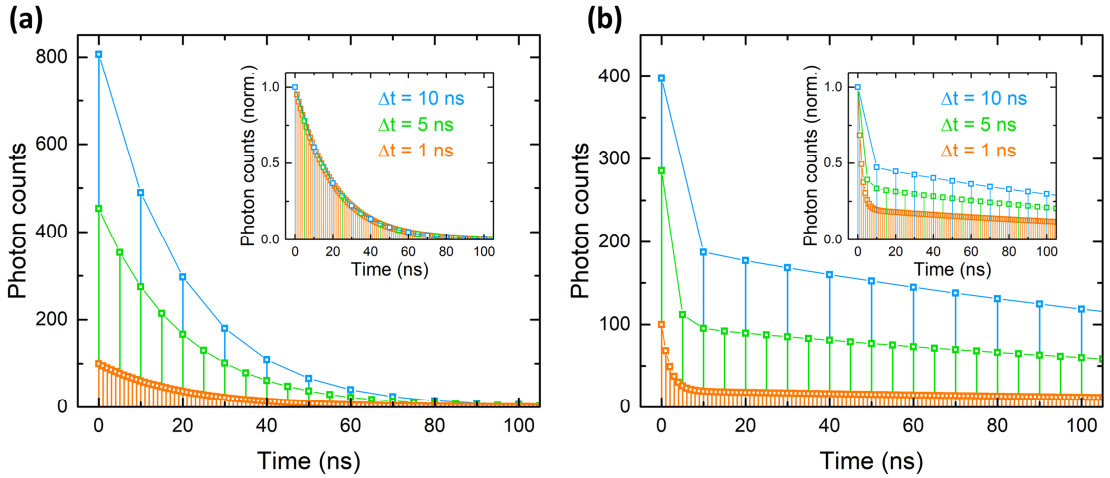

Figure 2.17. A decaying function simulated according to TCSPC principle with various sampling rates along the time axis. The blue, green, and orange curves were digitized with the discreet steps of 10, 5, and 1 ns, respectively. Inset: the same curves normalized to their maximum value. The decay function in (a) is monoexponential with the lifetime of 20 ns. The decay function in (b) is the sum of two exponents with the lifetimes of 2 and 200 ns.

The digital readout system can be also responsible for a poor time resolution in the TRPL experiment. In the streak imaging, a CCD camera with a finite density of pixels is placed behind the phosphor screen in order to digitize the signal. Clearly, higher density of the pixels provides better time resolution. In the TCSPC, a certain number of channels is assigned to the entire time window. This number of channels defines a unit step along the time axis and, therefore, the digital resolution of the readout. Certainly, this figure is arbitrary and can be changed within the software without any physical adjustments of the setup.

The optimal step of the digital readout is usually slightly below the width of the setup IRF. An overly large number of channels along the time axis (oversampling) makes the data acquisition unnecessarily long. The overly low number of channels along the time axis (undersampling) might distort the signal shape.

Figure 2.17 shows how different sampling rates along the time axis change the shape and intensity of the mono- and double-exponential decay curves in TCSPC. If the data is digitized with the step of 1 ns, there are 5 channels and 5 experimental points between 0 and 5 ns. If the data is digitized with the step of 5 ns, all photons coming to the detector within the interval 0–5 ns are now added up in one experimental point. Therefore, the magnitude of the signal recorded with large step along the time axis exceeds that of the same signal recorded with smaller step. Therefore, the signals recorded with different sampling rates should be normalized to their maximum value before the analysis. The inset in **Figure 2.17a** shows that the shape of monoexponential decay is undisturbed by the sampling rate. In contrast, the shape of decays containing short components is distorted by the undersampling (see inset in **Figure 2.17b**). Namely, the undersampling decreases the apparent contribution of the short component to the TRPL curve.

2.7. Summary

To sum up, in this Chapter we discussed the basic notions and parameters of PL spectroscopy putting an accent on experiment. The ideas proposed here should suffice for advanced steady-state and time-resolved PL measurements. The interpretation of the resulting data, however, requires deep understanding of the underlying physical processes. Thus, the following **Chapter 3** addresses the theory behind the fascinating phenomenon of luminescence. Such chapter arrangement outlines the way familiar to material physicists who gain new knowledge from scrupulous experiments and credible data.

2.8. References

(1) Fox, M. *Optical Properties of Solids*, 2nd ed.; Oxford University Press, **2010**.

(2) Köhler, A.; Bassler, H. *Electronic Processes in Organic Semiconductors*; Wiley-VCH, **2015**.

(3) Demas, J. N.; Grosby, G. A. The Measurement of Photoluminescence Quantum Yields. A Review. *J. Phys. Chem.* **1971**, *75*, 991–1024.

(4) Adams, M. J.; Highfield, G.; Kirkbright, G. F. Determination of Absolute Fluorescence Quantum Efficiency of Quinine Bisulfate in Aqueous Medium By. *Anal. Chem.* **1977**, *49*, 1850–1852.

(5) Brannon, J. H.; Magde, D. Absolute Quantum Yield Determination by Thermal Blooming. Fluorescein. *J. Phys. Chem.* **1978**, *82*, 705–709.

(6) Greenham, N. C.; Samuel, I. D. W.; Hayes, G. R.; Phillips, R. T.; Holmes, A. B.; Friend, R. H. Measurement of Absolute Photoluminescence Quantum Efficiencies in Conjugated Polymers. *Chem. Phys. Lett.* **1995**, 89–96.

(7) De Mello, J. C.; Wittmann, H. F.; Friend, R. H. An Improved Experimental Determination of External Photoluminescence Quantum Efficiency. *Adv. Mater.* **1997**, *9*, 230–232.

(8) Vavilov, S. I. The Dependence of the Intensity of the Fluorescence of Dyes upon the Wave-Length of the Exciting Light. *London, Edinburgh, Dublin Philos. Mag. J. Sci.* **1922**, *43*, 307–320.

(9) Kasha, M. Characterization of Electronic Transitions in Complex Molecules. *Disc. Faraday. Soc.* **1950**, *9*, 14–19.

(10) Saba, M.; Cadelano, M.; Marongiu, D.; Chen, F.; Sarritzu, V.; Sestu, N.; Figus, C.; Aresti, M.; Piras, R.; Geddo Lehmann, A.; et al. Correlated Electron-Hole Plasma in Organometal Perovskites. *Nat. Commun.* **2014**, *5*, 5049.

(11) Richter, J. M.; Abdi-Jalebi, M.; Sadhanala, A.; Tabachnyk, M.; Rivett, J. P. H.; Pazos-Outón, L. M.; Gödel, K. C.; Price, M.; Deschler, F.; Friend, R. H. Enhancing Photoluminescence Yields in Lead Halide Perovskites by Photon Recycling and Light Out-Coupling. *Nat. Commun.* **2016**, *7*.

(12) Staub, F.; Hempel, H.; Hebig, J. C.; Mock, J.; Paetzold, U. W.; Rau, U.; Unold, T.; Kirchartz, T. Beyond Bulk Lifetimes: Insights into Lead Halide Perovskite Films from Time-Resolved Photoluminescence. *Phys. Rev. Appl.* **2016**, *6*, 1–13.

Chapter 3

Photophysics behind Photoluminescence

ABSTRACT

In this Chapter, we discuss the photophysical processes leading to luminescence in organic and hybrid semiconductors. Our experimental PL data from polycrystalline perovskite films and molecular organic emitters illustrates the theoretical statements. Here, free carrier dynamics in the metal–halide perovskites is shown in band representation, which is typical for classic direct gap inorganic semiconductors, such as gallium arsenide. In contrast, excitonic transitions in molecular emitters are described in terms of potential energy curves, which are convenient for organic π-conjugated systems, such as polyacenes. We unify those seemingly different pictures using Jablonski state diagrams and rate equations. We show that basic kinetic models can describe various transitions within both organic and hybrid semiconductors and explain the experimental TRPL data.

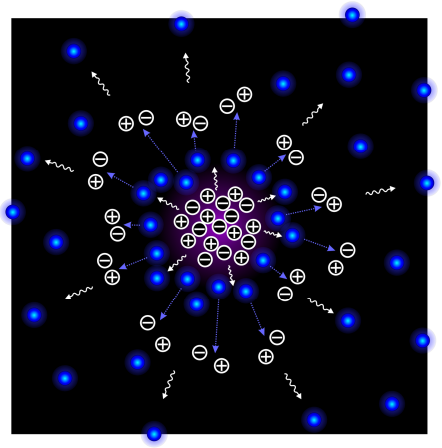

3.1. Photoluminescence from Metal–Halide Perovskites

3.1.1. Electron–Hole Recombination

In this Thesis, we focus on recombination processes in polycrystalline thin films of two lead-based perovskites: methylammonium lead iodide (MAPI) and formamidinium lead iodide (FAPI). During the last decade, those films have been widely used as an active layer for efficient solar cells.[1,2] Therefore, their production is comparatively well established,[3] which allows systematic material research.

PL from MAPI and FAPI at room temperature is caused by radiative interband recombination of free electrons and holes. The high absorption coefficient and sharp onset of absorption spectra imply the direct character of bandgap in MAPI and FAPI. **Figure 3.1a** shows the absorption and emission processes for direct gap semiconductors. Any photon with the energy above the gap, E_g, can be absorbed, which results in the broad absorption spectrum with the sharp onset around E_g (**Figure 3.1b**). Upon the photon absorption, electron and hole are formed in the conduction and valence band, respectively. Those excited charge carriers undergo quick thermal relaxation towards the energetic minima of their bands, from which they recombine radiatively. Therefore, the respective PL spectrum is a narrow peak centered near to E_g (**Figure 3.1b**). Its shape and width is defined by the density of states within the bands at given temperature.

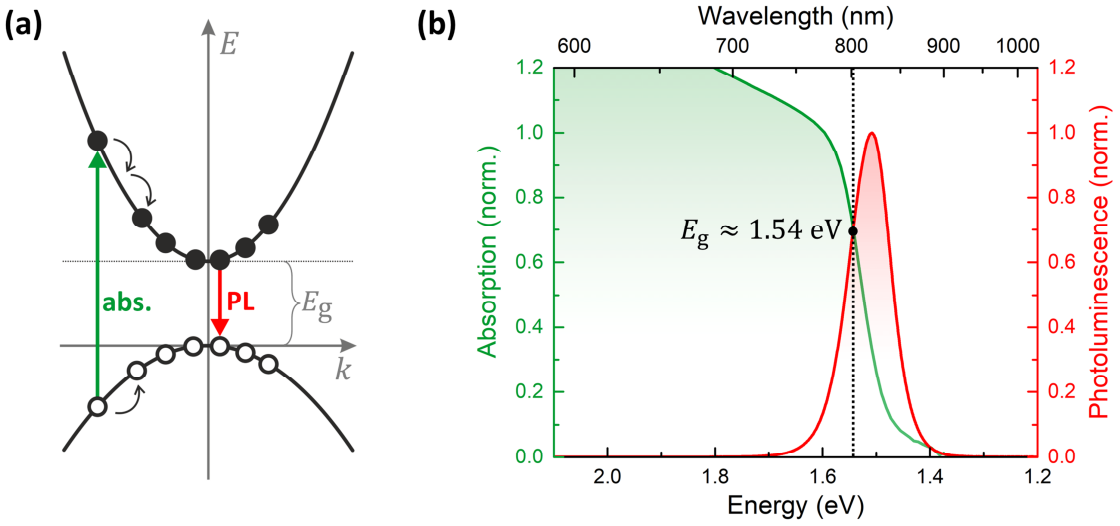

Figure 3.1. (a) Scheme of optical absorption, thermal intraband relaxation, and radiative band-to-band electron–hole recombination for direct gap semiconductors. (b) Normalized absorption and PL spectra for a polycrystalline FAPI film.

Lattice imperfections, grain boundaries, dangling bonds, and impurities in perovskite films can act as trap states intercepting excited charge carriers. Trap-mediated recombination is nonradiative, because the trapped electrons and holes dissipate their energy in form of thermal lattice vibrations, phonons.

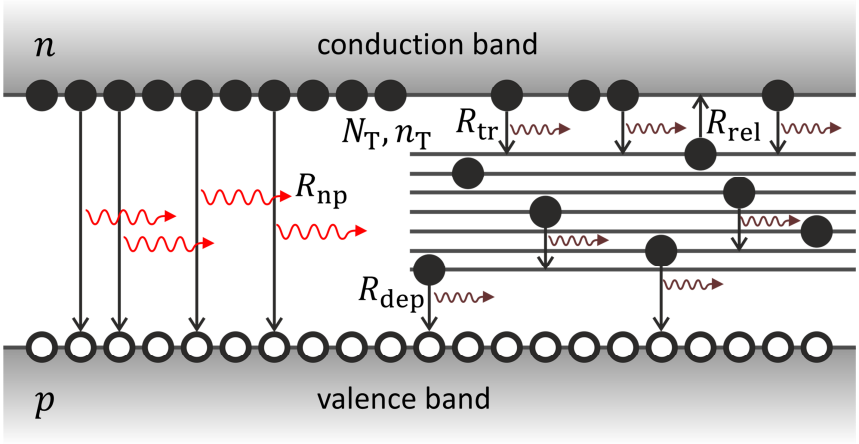

Figure 3.2. Direct band-to-band and trap-mediated electron–hole recombination in perovskites.

Generally, material scientists make every effort to eliminate the nonradiative pathways for solar cell absorbers, in order to push the device efficiency to its highest limit. Therefore, the defect origin and physics in perovskites, as in every novel material, is largely discussed in literature.[4–6] On one hand, perovskite photovoltaics profits from the simple film deposition from solution at room temperature. On the other hand, the solution-processing introduces a large variety of defects. Despite the proposed high defect-tolerance of MAPI,[7] the trap-assisted recombination remains an important player of charge carrier dynamics.

Depending on the trap depth, that is, their energy positioning relative to the conduction band, one can distinguish shallow and deep trap states. The electrons intercepted by shallow traps can be released back to the conduction band.[8,9] The electrons trapped in the deep traps are likely to remain there until they recombine nonradiatively.[10]

Figure 3.2 shows some radiative and nonradiative transitions in perovskites. The band representation here is simplified to Jablonski state diagram.[11] One can assign a characteristic rate constant to every type of transition. Here, we denote the rate of radiative band-to-band recombination with R_{np}, the rate of electron trapping with R_{tr}, the rate of electron release from the shallow traps with R_{rel}, and the rate of nonradiative depopulation of deep traps with R_{dep}. The kinetic equations for the recombination processes shown in **Figure 3.2** write as following:

$$\frac{dn(t)}{dt} = -R_{np}np - R_{tr}n(N_T - n_T) + R_{rel}n_T \quad (3.1)$$

$$\frac{dn_T(t)}{dt} = R_{tr}n(N_T - n_T) - R_{dep}n_Tp - R_{rel}n_T \quad (3.2)$$

$$\frac{dp(t)}{dt} = -R_{np}np - R_{dep}n_Tp \quad (3.3)$$

Here n and p are densities of free electrons and holes, respectively, n_T is the density of trapped electrons, and N_T is the constant trap density within the film. We further elaborate these equations and connect them with the experimental TRPL data in **Chapter 4**.

3.1.2. External Conditions

Interestingly, PL from MAPI can vary during its measurement. The magnitude, rate, and direction of the PL change depend on external conditions and excitation intensity. Therefore, multiple literature reports describing this so-called light-soaking effect are diverse and frequently contradicting. Almost every material characterization technique involves film illumination. Naturally, different groups use different light sources and different encapsulation methods. Thus, every researcher encounters major difficulties reproducing the data published by other groups, as long as the film response to external conditions is unclear. More importantly, the metal–halide perovskites are supposed to act as solar-cell absorbers, thus being permanently exposed to light. Therefore, the stable physical properties of the films or at least their predictable behavior under illumination are imperative in perovskite photovoltaics.

The most dramatic (up to thousandfold) increase of PL intensity in metal–halide perovskites under illumination was observed in presence of oxygen.[12–14] Consequently, the authors explain this phenomenon by oxygen-induced defect healing. However, a moderate growth of PL signal was reported also for the samples measured in the nitrogen atmosphere,[12,15] in vacuum,[15] and for those covered with additional protective layers.[16–18] This time, the proposed explanations of PL enhancement include light-induced defect curing at low illumination intensities,[16] carrier confinement within the crystalline domains,[17] photo-activated ion redistribution within the perovskite bulk,[15] and electrically-driven ion migration toward the selective contacts.[18] On the contrary, some authors argue that the ion migration causes nonradiative recombination and suppresses PL for high excitation intensities.[16] Note that the light-soaking occurs in freshly prepared perovskite films and is unrelated to material degradation.

We observed a stable PL signal under low excitation intensity for MAPI film deposited by two-step technique (see **Chapter 4**, **Figure 4.11**). The absolute PL intensity, spectral shape, and TRPL curve remained unaltered within 1 hour under illumination, which allowed us to record transient data for all samples without light-soaking effect or degradation.

In contrast, a strong light-soaking effect took place for the samples illuminated with an intense continuous sharply focused laser beam in **Chapter 5**. For both MAPI and FAPI films, the PL signal rapidly built up and fully stabilized within 2–4 min (see **Figure 5.2**). Therefore, we illuminated the perovskite films for 5 min prior to each data acquisition in **Chapter 5**, thus attaining a stable PL image in the stationary recombination mode.

3.2. Photoluminescence from Molecular Organic Emitters

3.2.1. Exciton Dynamics

Carbon-based molecules with alternating single and double bonds share their atomic p-orbitals along the carbon chain to form an extended molecular π-orbital. This orbital

endows the π-conjugated organic compounds with the intrinsic semiconducting properties and electronic transitions in optical region.[19] The unique electronic, optical, and mechanical properties of organic semiconductors, along with the almost infinite capabilities of organic synthesis, gave rise to a broad interdisciplinary field of plastic electronics. Today, many products of plastic electronics, such as organic solar cells and organic light emitting diodes (OLEDs), are commercialized, while the emerging ideas and novel materials occupy scientific laboratories and researcher minds all around the world. In **Chapter 6** of this Thesis, we focus on a deep blue organic emitter SBABz4 that shows thermally activated delayed fluorescence (TADF), thereby meeting both color and efficiency challenges of the last generation OLEDs.

Excited electrons and holes in organic materials experience strong Coulomb attraction, because of low dielectric constant and subsequently negligible microscopic screening. As a result, the bound electron–hole pairs form neutral quasi-particles — excitons. An exciton can be distributed over a large distance, like in molecular crystals or conjugated polymers, or confined to one molecule, like in our case of intramolecular emissive state. In following, we use a state representation that depicts the total potential energy of the molecule depending on the normal configuration coordinate of its nuclei.

Figure 3.3a shows the simplified potential energy curves and the corresponding transitions for a ground singlet and the first excited singlet and triplet states. Transitions between the states of the same multiplicity are called internal conversion (IC); those between singlet and triplet states are called intersystem crossing (ISC). IC is dipole-allowed and therefore fast (from picoseconds to nanoseconds), whereas ISC is dipole-forbidden and thus slow (from microseconds to seconds).

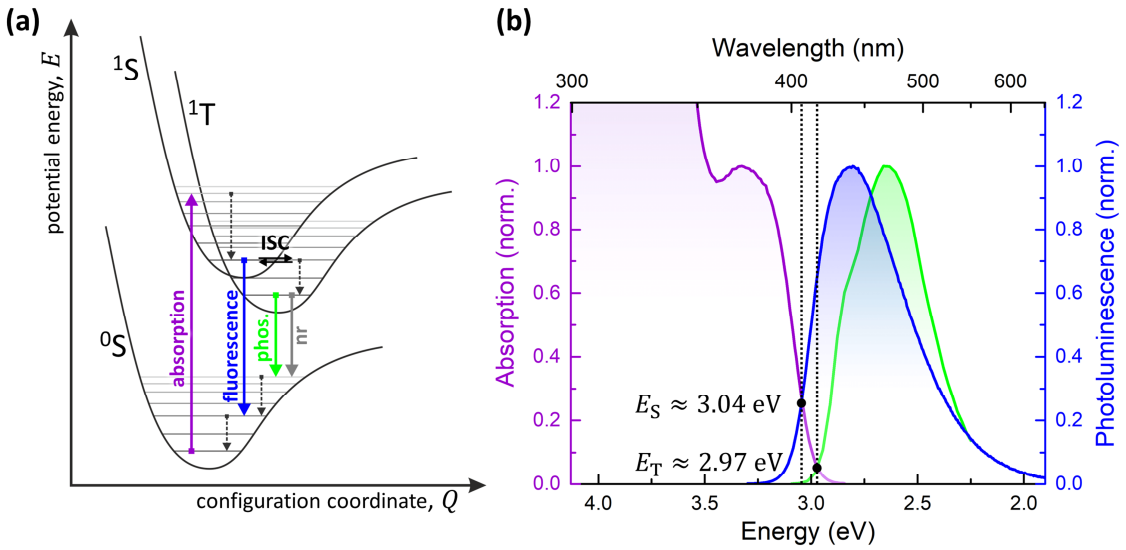

Figure 3.3. (a) Simplified potential energy curves for ground and excited singlet and triplet states of organic molecule. Black dashed arrows show internal conversion (IC) between the vibrational sublevels of one state; black solid arrows show intersystem crossing (ISC) between the singlet and triplet excited states; purple, blue, green, and gray arrows show absorption, fluorescence, phosphorescence, and nonradiative decay, respectively. (b) Absorption and emission spectra of SBABz4 thin film. Color coding corresponds to the transitions in (a).

Strictly speaking, absorption and fluorescence are IC between ^{0}S and ^{1}S, and phosphorescence is ISC between ^{1}T and ^{0}S. However, those processes are traditionally referred to with their respective names. Accordingly, we will use the term IC only for the transitions between the vibrational sublevels within one state or for those from the higher excited singlets (triplets) to the first excited singlet (triplet). In turn, we will call ISC the transition between ^{1}S and ^{1}T. The reverse ISC (RISC) is especially important for our work, because it facilitates TADF.

Nuclear coordinates remain stable within the short time frame of IC. Therefore, state diagrams depict absorption, fluorescence, and thermal intrastate relaxation with vertical arrows. Here, we also show phosphorescence and nonradiative triplet decay with vertical arrows, because more accurate graphical representation is not feasible for our simplified diagram.[20] However, the horizontal arrows for ISC in **Figure 3.3a** emphasize the tunnelling character of this transition. Spin–orbit coupling adds the minor triplet components to the wavefunction of the excited singlet state, thus facilitating ISC and RISC.[20] The rate and efficiency of the direct ISC can compete with fluorescence; whereas the RISC is usually very slow, because it is mediated by the thermal population of the upper vibrational ^{1}T sublevels. The experimental characteristic constants for ISC and RISC are calculated in **Chapter 6**.

The downward IC provides prompt thermal relaxation (~1 ps) toward the bottom of the ground and the first excited states, because their vibrational sublevels are in a very close proximity with each other. Therefore, absorption occurs from the lowest vibrational sublevel of ^{0}S, and fluorescence from the lowest vibrational sublevel of ^{1}S. As a result, PL spectrum and quantum yield are independent of the excitation wavelength (Kasha and Vavilov rules, respectively).[21,22]

Harmonic function approximates the minima of potential energy curves very well. Therefore, the lower vibrational sublevels are equally spaced for ground and excited states. The distance between them is equal to one vibrational quantum (≈100–400 meV, depending on the mode considered).[19] One might expect the absorption and emission spectra to have vibronic structure that is defined by the electronic transitions to the different vibrational sublevels. However, the vibronic progression in amorphous systems is disguised by the thermal oscillations of individual molecules and the randomized energy distribution of the entire molecular ensemble.

Selection rules allow optical absorption to any vibrational sublevel of the excited singlet, as well as the radiative relaxation to any vibrational sublevel of the ground singlet. Thus, absorption and fluorescence spectra of organic molecules usually mirror each other. **Figure 3.3b** shows an example of the mirror rule for an amorphous film of SBABz4 emitter.

The intersection of absorption and corrected florescence spectra on energy scale corresponds to the gap between the lowest vibrational sublevels of ^{0}S and ^{1}S, which is analogous to the energy gap of inorganic semiconductors.[23] If the lowest possible energy of the molecule is chosen as a reference and arbitrary set to zero, then the intersection of

absorption and fluorescence spectra indicates the energy of the first excited singlet, whereas the intersection of absorption and phosphorescence spectra is approximately the energy of the first triplet state (**Figure 3.3b**). Their difference gives the singlet–triplet energy gap, ΔE_{ST}, that defines the TADF efficiency. We estimated $\Delta E_{\mathrm{ST}} \approx 70\ \mathrm{meV}$ for SBABz4 emitter independently from the steady-state PL (**Figure 3.3b**) and temperature-dependent transient PL (**Chapter 6**, **Section 6.2.4**).

As mentioned in **Chapter 2**, fluorescence spectra of organic emitters are usually redshifted relative to their absorption. The quantitive measure of this so-called Stokes shift is conventionally taken as a difference between the nearest peaks of absorption and fluorescence spectra (although IUPAC more strictly defines it as the energy difference between the 0–0 transitions observed in absorption and emission).[24] The Stokes shift is completely absent only for the exactly resonant 0–0 transitions of individual emitters in the gas phase at low temperatures. For all other cases, Stokes shift can have different physical reasons. For example, the first peak of vibronic progression can be suppressed because of poor overlap of the respective wavefunctions. Then the apparent PL maximum corresponds to the second peak, which will result in a large Stokes shift. The PL spectrum can be also red shifted because of solvation effects or because of electronic coupling among the densely packed molecules. We will discuss the effects of molecular surrounding in the next **Section 3.2.2**. Finally, the organic molecules with flexible bonds can change their geometry between the ground and excited states (for example, from twisted to the planar one).[25] Such conformational relaxation also results in a Stokes shift.

Figure 3.4 shows a further simplified Jablonsky diagram for all discussed transitions. This diagram is especially convenient for mathematical description of the exciton dynamics. A complete solution for the three-level system with RISC is elaborated in **Chapter 6**. Now, for clarity of the illustration, we will derive a basic connection of PL lifetime and PLQY for a simpler two-level system.

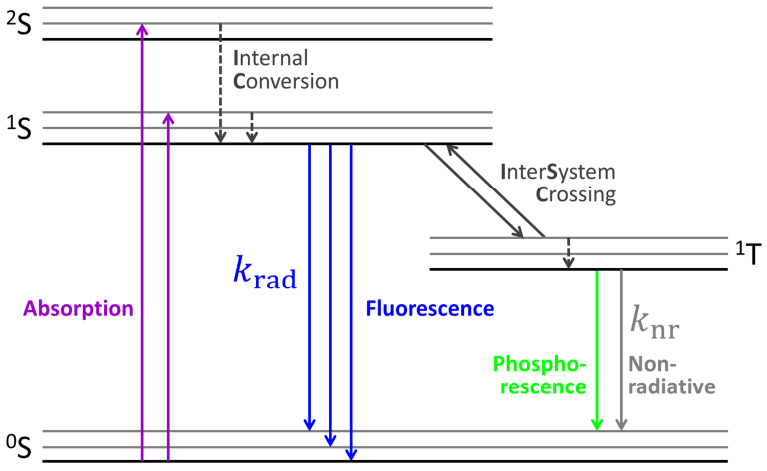

Figure 3.4. Jablonsky state diagram showing the main transitions within organic molecule.

The kinetic equation for excitons in two-level system writes:

$$\frac{dn(t)}{dt} = -k_{\mathrm{rad}}n - k_{\mathrm{nr}}n \tag{3.4}$$

Here k_{rad} and k_{nr} are the rates of radiative and nonradiative decay, respectively, and n is the density of excited species. One can consider any organic molecule in which RISC and phosphorescence are inefficient as a two-level system. Then, the nonradiative singlet depopulation occurs via the irreversible ISC to triplet.

Integral of **Eq. 3.4** describes the exponential decay of the exciton population:

$$n(t) = n_0 \mathrm{e}^{-\frac{t}{\tau}} \tag{3.5}$$

$$\tau \equiv \frac{1}{k_{\mathrm{rad}} + k_{\mathrm{nr}}} \tag{3.6}$$

Here n_0 is the initial exciton density, and τ is the exciton lifetime. PL signal originates from the radiative decay component, that is, $\mathrm{PL}(t) = k_{\mathrm{rad}}n(t)$. By definition, PLQY is the ratio of emitted photons to the number of absorbed photons. Taking into account that every absorbed photon gives rise to one exciton, we can now calculate PLQY:

$$\mathrm{PLQY}(t) = \frac{1}{n_0}\int_0^{\infty} k_{\mathrm{rad}}n_0 \mathrm{e}^{-\frac{t}{\tau}}\,dt \tag{3.7}$$

Integrating **Eq. 3.7**, we obtain the classical expression for PLQY of two-level system:

$$\mathrm{PLQY}(t) = \frac{k_{\mathrm{rad}}}{k_{\mathrm{rad}} + k_{\mathrm{nr}}} \tag{3.8}$$

The same approach can be applied to more complex optical systems with the assigned transitions rates, as we demonstrate in **Chapter 6**.

3.2.2. Molecular Surrounding

TADF requires a large spatial separation of the highest occupied and the lowest unoccupied molecular orbitals. By definition, intramolecular charge-transfer (CT) is an electronic transition in which a large fraction of an electronic charge is transferred from one region of a molecular entity (the electron donor) to another (the electron acceptor).[24] Therefore, the excited state of TADF emitter is charge-transfer (CT) state.

CT states are easily polarizable, because they acquire a large static dipole moment in comparison with ground state. Thus, they are extremely sensitive to the microscopic polarization of their molecular surrounding. The characteristic feature or TADF molecules is strong solvatochromism, that is, shift of emission spectra depending on solvent polarity.[26] We detected a dramatic PL redshift of 0.7 eV for SBABz4 solutions, which manifested itself in the change of emission color from deep purple in cyclohexane to bright green in methanol (see **Figure 6.2** in **Chapter 6**).

Polarization effects in solid phase result in broad featureless PL spectra even at low temperatures. Every emitter molecule of amorphous film is fixed in a slightly different surrounding. As a result, the film emission consists of many overlapping slightly displaced PL spectra from the molecular ensemble. For the same reason, the PL decay curve of amorphous SBABz4 film is described with a stretched exponential function: it is a superposition of multiple monoexponential decays with slightly different lifetimes.

TADF molecules usually have an extended twistable bond between the donor and acceptor units. Such structural design provides the narrow singlet–triplet energy gap, which is desirable for RISC. On the other hand, the twistable molecules tend to change their geometry between the ground and excited states. This conformational relaxation can provide degeneration of excited singlet and triplet states, thus increasing both TADF rate and efficiency.[25] Note that amorphous film of TADF emitters contains a large ensemble of molecules with a broad distribution of donor–acceptor torsional angles and, therefore, a broad distribution of singlet and triplet energies. Thus, the experimentally defined singlet–triplet gap is actually an average value.

Another important feature of small organic molecules is their tendency to form physical dimers and aggregates. The excited states of the adjacent emitters split because of their resonance interaction. This splitting results in formation of lower-lying states that promote nonradiative decay. Isolation of the emitter molecules in the matrix prevents aggregation and increases TADF efficiency, as we show in **Section 6.2.3** of **Chapter 6**.

Another indication of TADF is quenching by molecular oxygen, O_2, via energy transfer. O_2 has a triplet ground state and the first excited singlet state separated only by 0.98 eV.[19] Therefore, the energy transfer from the excited triplet state of TADF emitter to the adjacent oxygen molecule is extremely efficient. As a result, O_2 can completely quench TADF in solution (**Chapter 6**, **Section 6.2.2**). The excited singlet oxygen, which forms during the energy transfer, is a dangerous impurity, because it is extremely reactive and may attack π–bonds of organic semiconductors. Otherwise, the O_2 quenching is reversible: the triplet emission is restored as soon as solution is deoxygenated.

3.3. Summary

To sum up, here we discussed photophysics standing behind PL in hybrid and organic semiconductors. In the following chapters, we apply these concepts to real material systems.

3.4. References

(1) Snaith, H. J. Perovskites : The Emergence of a New Era for Low-Cost , High-. *J. Phys. Chem. Lett* **2013**, *4*, 3623−3630.

(2) Stranks, S. D.; Snaith, H. J. Metal-Halide Perovskites for Photovoltaic and Light-Emitting Devices. *Nat. Nanotechnol.* **2015**, *10*, 391–402.

(3) Stranks, S. D.; Nayak, P. K.; Zhang, W.; Stergiopoulos, T.; Snaith, H. J. Formation of Thin Films of Organic-Inorganic Perovskites for High-Efficiency Solar Cells. *Angew. Chem., Int. Ed.* **2015**, *54*, 3240–3248.

(4) Ball, J. M.; Petrozza, A. Defects in Perovskite-Halides and Their Effects in Solar Cells. *Nat. Energy* **2016**, *1*, 16149.

(5) Leijtens, T.; Eperon, G. E.; Barker, A. J.; Grancini, G.; Zhang, W.; Ball, J. M.; Kandada, A. R. S.; Snaith, H. J.; Petrozza, A. Carrier Trapping and Recombination: The Role of Defect Physics in Enhancing the Open Circuit Voltage of Metal Halide Perovskite Solar Cells. *Energy Environ. Sci.* **2016**, *9*, 3472–3481.

(6) Barker, A. J.; Sadhanala, A.; Deschler, F.; Gandini, M.; Senanayak, S. P.; Pearce, P. M.; Mosconi, E.; Pearson, A. J.; Wu, Y.; Kandada, A. R. S.; et al. Defect-Assisted Photoinduced Halide Segregation in Mixed-Halide Perovskite Thin Films. *ACS Energy Lett.* **2017**, *2*, 1416–1424.

(7) Steirer, K. X.; Schulz, P.; Teeter, G.; Stevanovic, V.; Yang, M.; Zhu, K.; Berry, J. J. Defect Tolerance in Methylammonium Lead Triiodide Perovskite. *ACS Energy Lett.* **2016**, *1*, 360–366.

(8) Yamada, Y.; Yamada, T.; Shimazaki, A.; Wakamiya, A.; Kanemitsu, Y. Interfacial Charge-Carrier Trapping in $CH_3NH_3PbI_3$-Based Heterolayered Structures Revealed by Time-Resolved Photoluminescence Spectroscopy. *J. Phys. Chem. Lett.* **2016**, *7*, 1972–1977.

(9) Chirvony, V. S.; González-Carrero, S.; Suarez, I.; Galian, R. E.; Sessolo, M.; Bolink, H. J.; Martinez-Pastor, J. P.; Pérez-Prieto, J. Delayed Luminescence in Lead Halide Perovskite Nanocrystals. *J. Phys. Chem. C* **2017**, *121*, 13381–13390.

(10) Kandada, A. R. S.; Neutzner, S.; D'Innocenzo, V.; Tassone, F.; Gandini, M.; Akkerman, Q. A.; Prato, M.; Manna, L.; Petrozza, A.; Lanzani, G. Nonlinear Carrier Interactions in Lead Halide Perovskites and the Role of Defects. *J. Am. Chem. Soc.* **2016**, *138*, 13604–13611.

(11) Lakowicz, J. R. *Principles of Fluorescence Spectroscopy*, 3rd ed.; Springer, **2006**.

(12) Tian, Y.; Peter, M.; Unger, E.; Abdellah, M.; Zheng, K.; Pullerits, T.; Yartsev, A.; Sundström, V.; Scheblykin, I. G. Mechanistic Insights into Perovskite Photoluminescence Enhancement: Light Curing with Oxygen Can Boost Yield Thousandfold. *Phys. Chem. Chem. Phys.* **2015**, *17*, 24978–24987.

(13) Motti, S. G.; Gandini, M.; Barker, A. J.; Ball, J. M.; Srimath Kandada, A. R.; Petrozza, A. Photoinduced Emissive Trap States in Lead Halide Perovskite Semiconductors. *ACS Energy Lett.* **2016**, *1*, 726–730.

(14) Brenes, R.; Guo, D.; Osherov, A.; Noel, N. K.; Eames, C.; Hutter, E. M.; Pathak, S.; Niroui, F.; Friend, R. H.; Islam, M. S.; et al. Metal Halide Perovskite Polycrystalline Films Exhibiting Properties of Single Crystals. *Joule* **2017**, *1*, 155–167.

(15) deQuilettes, D. W.; Zhang, W.; Burlakov, V. M.; Graham, D. J.; Leijtens, T.; Osherov, A.; Bulović, V.; Snaith, H. J.; Ginger, D. S.; Stranks, S. D. Photo-Induced Halide Redistribution in Organic–Inorganic Perovskite Films. *Nat. Commun.* **2016**, *7*, 11683.

(16) Chen, S.; Wen, X.; Huang, S.; Huang, F.; Cheng, Y.-B.; Green, M.; Ho-Baillie, A. Light Illumination Induced Photoluminescence Enhancement and Quenching in Lead Halide Perovskite. *Sol. RRL* **2017**, *1*, 1600001.

(17) Stoddard, R. J.; Eickemeyer, F. T.; Katahara, J. K.; Hillhouse, H. W. Correlation between Photoluminescence and Carrier Transport and a Simple in Situ Passivation Method for High-Bandgap Hybrid Perovskites. *J. Phys. Chem. Lett.* **2017**, *8*, 3289–3298.

(18) Zhang, T.; Cheung, S.-H.; Meng, X.; Zhu, L.; Bai, Y.; Ho, C. H. Y.; Xiao, S.; Xue, Q.; So, S. K.; Yang, S. Pinning Down the Anomalous Light Soaking Effect Towards High Performance and Fast Response Perovskite Solar Cells: The Ion-Migration Induced Charge Accumulation. *J. Phys. Chem. Lett.* **2017**, acs.jpclett.7b02160.

(19) Köhler, A.; Bassler, H. *Electronic Processes in Organic Semiconductors*; Wiley-VCH, **2015**.

(20) Baryshnikov, G.; Minaev, B.; Ågren, H. Theory and Calculation of the Phosphorescence Phenomenon. *Chem. Rev.* **2017**, *117*, 6500–6537.

(21) Kasha, M. Characterization of Electronic Transitions in Complex Molecules. *Disc. Faraday. Soc.* **1950**, *9*, 14–19.

(22) Vavilov, S. I. The Dependence of the Intensity of the Fluorescence of Dyes upon the Wave-Length of the Exciting Light. *London, Edinburgh, Dublin Philos. Mag. J. Sci.* **1922**, *43*, 307–320.

(23) Vandewal, K.; Benduhn, J.; Nikolis, V. C. How to Determine Optical Gaps and Voltage Losses in Organic Photovoltaic Materials. *Sustain. Energy Fuels* **2017**, *2*, 538–544.

(24) Braslavsky, S. E. Glossary of Terms Used in Photochemistry. *Pure Appl. Chem* **2007**, *79*, 293–465.

(25) Di, D.; Di, D.; Romanov, A. S.; Yang, L.; Richter, J. M.; Rivett, J. P. H.; Jones, S.; Thomas, T. H.; Jalebi, M. A.; Friend, R. H.; et al. High-Performance Light-Emitting Diodes Based on Carbene-Metal-Amides. *Science* **2017**, *4345*, 1–10.

(26) Grabowski, Z. R.; Rotkiewicz, K.; Rettig, W. Structural Changes Accompanying Intramolecular Electron Transfer: Focus on Twisted Intramolecular Charge-Transfer States and Structures. *Chem. Rev.* **2003**, *103*, 3899–4031.

Chapter 4

Impact of Interfaces and Laser Repetition Rate on Photocarrier Dynamics in Lead Halide Perovskites

ABSTRACT

We studied charge carrier recombination in methyl ammonium lead iodide (MAPI) perovskite and the impact of interfaces on the charge carrier lifetime using time-resolved photoluminescence. Pristine films and those covered with organic electron and hole transport materials (ETM and HTM) were investigated at various laser repetition rates ranging from 10 kHz to 10 MHz in order to separate the bulk and interface-affected recombination. We revealed two different components in the PL decay. The fast component (shorter than 300 ns) is assigned to interfacial processes and the slow one to bulk recombination. A high repetition pulse train was shown to shorten PL decay in pristine perovskite while significantly prolonging the photocarrier lifetime in MAPI covered by TMs. This effect can be qualitatively explained with a kinetic model taking interface traps into account. We demonstrate a significant influence of the excitation repetition rate on photocarrier lifetime, which should be considered when studying charge carrier dynamics in perovskites.

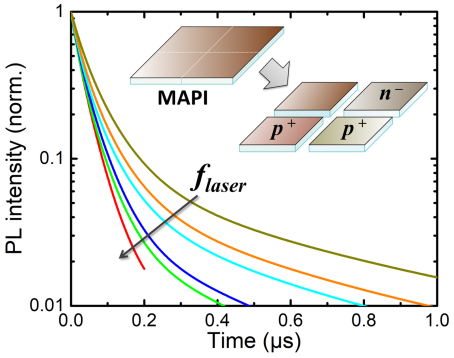

Partially based on:

Kudriashova, L. G.; Kiermasch, D.; Rieder, P.; Campbell, M.; Tvingstedt, K.; Baumann, A.; Astakhov, G. V.; Dyakonov, V. Impact of Interfaces and Laser Repetition Rate on Photocarrier Dynamics in Lead Halide Perovskites. *J. Phys. Chem. Lett.* **2017**, *8*, 4697–4703.

4.1. Introduction

Hybrid halide perovskite-based photovoltaics have sustained dramatic development over the past years, achieving solar cells with power conversion efficiencies above 22%.[1] This tremendous efficiency progress can be attributed to the appealing intrinsic properties of the lead-based (bulk) perovskites themselves, such as long charge-carrier lifetimes,[2–4] low exciton binding energy,[5] and high absorption coefficient (10^4–10^5 cm^{-1} in the visible region),[6,7] as well as the film quality of the perovskite absorber,[8,9] development of energetically suitable charge transport materials,[10] and variation of device architecture.[11] Despite the great efficiency progress, the unintentional defects formed during growth should be seriously considered, because their impact on charge carrier recombination[12] and generally on the charge transport properties inhibits the targeted production of high-performance solar cells. Scientific discussions about trap origins, their energetics in perovskites, and their impact on solar cell performance remains ongoing.

The adjacent charge transport layers in a solar cell are of particular importance because of the assumed defect tolerance of bulk halide perovskites.[13,14] The transport layers do not only determine the growing conditions and the crystallinity of the perovskite film, but also form interfaces, which can in turn lead to losses of photogenerated charge carriers. All in all, the separation of bulk and interface recombination effects is nontrivial and requires combined measurements on incomplete devices as well as on pristine films. Experimental isolation of surface and bulk effects was previously achieved in photoluminescence (PL) measurements by depositing quenching layers on perovskites[2] or varying the light penetration depth by one- and two-photon fluorescence microscopy.[15]

Steady-state and time-resolved photoluminescence (TRPL) are widely used non-contact characterization techniques for semiconductors. PL signal, being proportional to the density product of recombining electrons and holes, is sensitive to a variety of processes that change the excited-state population.[16] Coexistence of several recombination pathways — including trap-assisted first-order, band-to-band second-order, and higher order Auger recombination[16,17] — results in different decay dynamics and makes exponential fits hardly justifiable or alternatively requires numerical analysis of PL transients with a number of characteristic constants.[4] The complex charge carrier dynamics leads to ambiguity in interpretation of TRPL data and discrepancies among the published recombination models.[4,17–19] Note that nearly all recombination models include trap-assisted processes. Trap filling and depopulation are anticipated to be of crucial importance for the interpretation of transient PL in perovskites.

The role of repetition rate in the TRPL experiment and its impact on recombination dynamics has not previously been addressed. Usually, the repetition rate is fixed to a certain value between 100 kHz and 80 MHz, depending on the laser system. Here we show that one can pile up charge carriers and therefore greatly influence the carrier dynamics in perovskites by varying the laser repetition rate, f, in the TRPL experiment. A similar approach

was used by M. Saba *et al*. to investigate photoluminescence dynamics in colloidal core–shell nanocrystals.[20] Both photocharging and charge trapping were found to contribute to photoluminescence quenching.

In this Chapter, we studied methylammonium lead iodide ($CH_3NH_3PbI_3$) perovskite films formed on a glass substrate and then divided into four parts. Electron or hole transport materials (ETM or HTM) were subsequently spin-coated on top of the samples. With an ETM/HTM present, we observe significant prolongation of PL lifetime with increasing f, despite the possible formation of extrinsic defects at the interface. We explain such behavior with a quasi-stationary charge carrier population built-up at higher f and effective filling of the interfacial traps, which leads to their passivation. We discuss the impact of f on radiative emission decay in the framework of commonly used kinetic models. Here we highlight the role of the interfaces between the lead halide perovskite and the various charge transport materials. Our results illustrate the impact of the interfaces on recombination and demonstrate how the interface trap filling leads to prolongation of apparent charge carrier lifetime.

4.2. Results and Discussion

4.2.1. Bulk and Interface-Affected Recombination

We studied $CH_3NH_3PbI_3$ films (further referred to as MAPI) covered with charge transport materials widely implemented in perovskite photovoltaics: $PC_{60}BM$ (ETM, further referred to as PCBM), P3HT (HTM), and spiro-MeOTAD (HTM).

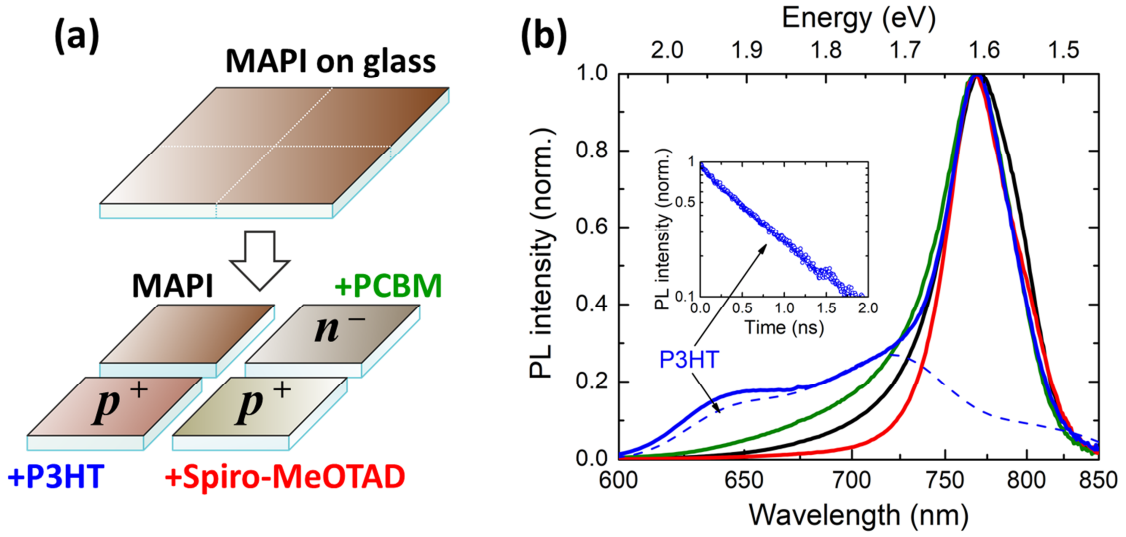

Figure 4.1. (a) Scheme of sample preparation. MAPI film (black) was prepared on a 1 × 1 in. glass substrate and then cut into four parts. Charge-selective layers (PCBM (green), spiro-MeOTAD (red), and P3HT (blue)) were deposited on top of three of them. (b) Steady-state PL spectra of pristine MAPI and MAPI with charge-selective layers. The dashed curve is a normalized PL spectrum of P3HT film. The inset shows PL decay curve of P3HT.

MAPI film was formed on a 1 x 1 in. precut glass substrate and then separated into four parts. Charge transport materials were then spin-coated on top of three of them (see **Figure 4.1a** and **Section 4.4.1**), while the fourth sample, a pristine MAPI film, was used as a reference. With this approach, we attempted to maintain the same crystallization conditions for the perovskite film in all studied samples and to isolate the influences of the interfaces between MAPI and the transport layers. Note that an interface between bulk MAPI and air-exposed MAPI can also occur in the nonencapsulated reference sample.

Figure 4.1b shows normalized PL spectra for pristine MAPI and MAPI with charge transport layers. PL was excited at 505 nm and collected from the top of every sample, that is, through the transport layers in layered films. The unchanged PL band of MAPI in all steady-state spectra indicates that the perovskite electronic structure is also maintained for samples with additional charge-selective layers.

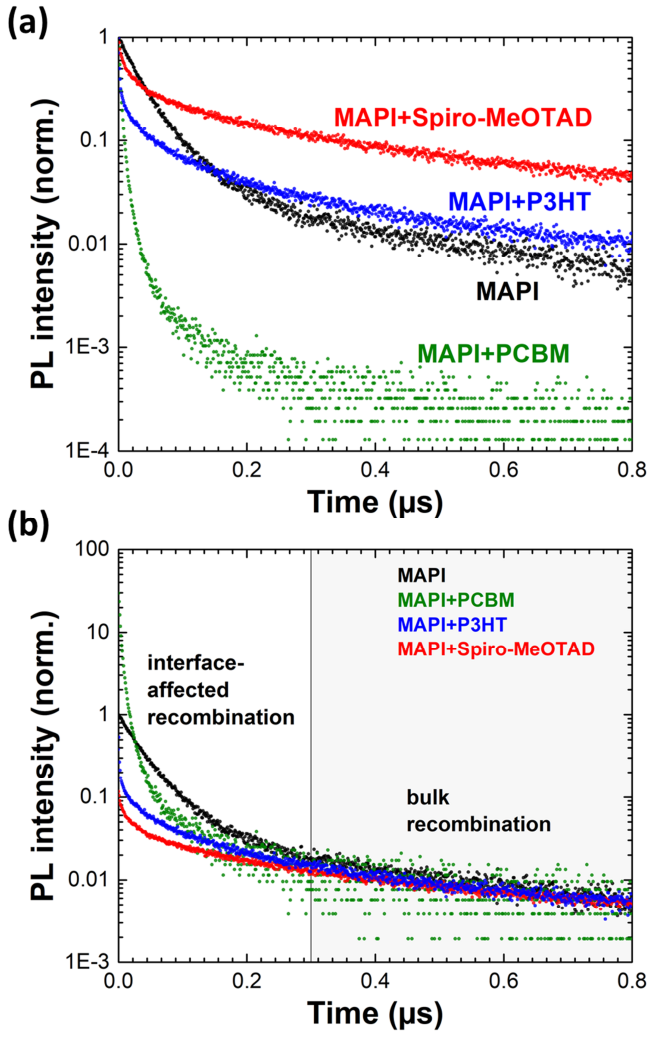

Figure 4.2. PL decay curves in the perovskite films recorded under ambient conditions at 770 nm with pulsed-laser excitation at 505 nm and laser repetition rate f = 1 MHz. The transients are normalized to the initial PL peak in (a) and to the slower decay portion of the reference MAPI sample in (b). Color coding of the experimental points corresponds to the sample type (see the legend).

PL from spiro-MeOTAD and PCBM does not overlap with the relevant region of perovskite emission. The P3HT layer shows weak PL emission at 770 nm with the exponential lifetime of only 0.8 ns (see inset in **Figure 4.1b**), which is below the time resolution of the photon-counting system used in this work (≈ 2 ns, see **Section 4.4.2**). Therefore, the excitation and detection through charge transport layers does not affect PL decay curves.

Figure 4.2a shows normalized PL transients for pristine MAPI and MAPI with charge transport layers. The transients were detected at the maximum of perovskite emission, 770 nm (see steady-state PL spectra in **Figure 4.1a**).

All four measured PL transients demonstrate an initial fast decay and an extended slower decay. Thereby, the charge transport layers noticeably change the relative magnitudes of the fast and slow portions in the recombination dynamics. PL transient decays much faster in the presence of the electron-selective PCBM layer, and PL becomes almost negligible after 300 ns. Meantime, a slow PL component dominates in the samples with hole-selective layers — spiro-MeOTAD and P3HT.

Figure 4.2b shows the same PL transients, normalized to the slower decay portion of the reference sample MAPI. The plot allows temporal separation of the two sections in the PL transient: the fast part, in which PL decay differs depending on the different interfaces, extends up to 300 ns, while the slower portion is exactly the same for all four investigated samples. The perovskite film morphology is expected to be identical for all examined samples because of identical growing conditions; therefore, we ascribe the slow PL decay to bulk recombination and the initial fast decay to interface-affected recombination.

4.2.2. Effect of Laser Repetition Rate

The laser repetition rate in the TRPL experiment is an important parameter that must be individually chosen for any system under study. The time lag between two subsequent excitation pulses should usually exceed the relaxation time of the excited state. This condition ensures that excitation of the unrelaxed system to higher energy levels is avoided, simplifying data interpretation.[21] Additionally, the pulse train with high repetition rate may pile up the charge carrier density in the sample and lead to shorter PL lifetimes in the case of second order recombination.

Figure 4.3 shows normalized PL transients taken at different rates f for every sample. The position of the sample, monochromator bandwidths, excitation beam focus, laser pulse energy, and other parameters besides the laser repetition rate were fixed for all experiments presented here. Transients in every set were taken from the slowest to the fastest laser repetition rate. **Figure 4.3** clearly demonstrates a strong influence of the laser repetition rate on the PL decay in all samples. This finding implies the existence of an optimal, sufficiently low repetition rate, f, for each individual perovskite system. Above this threshold, f begins to affect the PL decay. In other words, the repetition rate should be taken into account as a parameter influencing carrier recombination dynamics in perovskites.

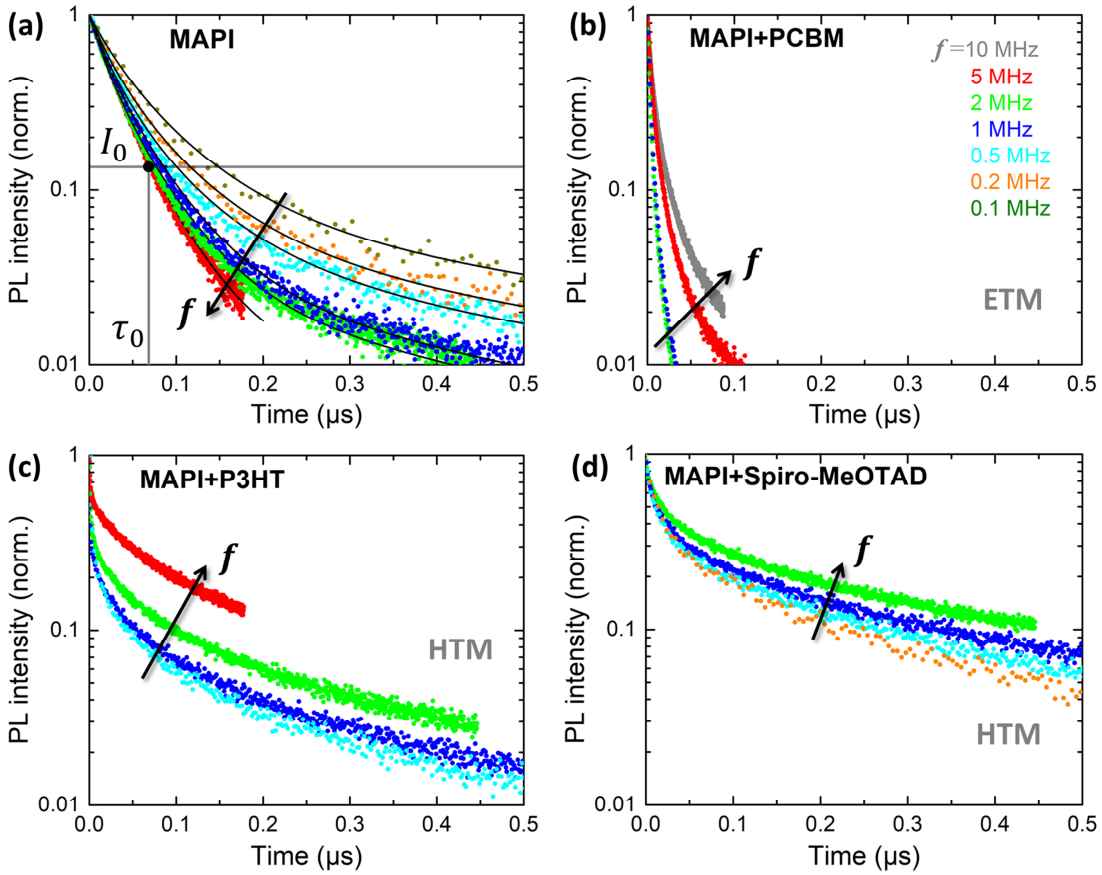

Figure 4.3. Normalized PL decay curves taken at various f values (excitation at 505 nm, detection at 770 nm). (a) Pristine MAPI, (b) MAPI with electron-selective layer PCBM, (c) MAPI with hole-selective layer P3HT, and (d) MAPI with hole-selective layer spiro-MeOTAD. Dots represent the experimental data; black curves show numerical fits for MAPI to the kinetic model of **Eq. 4.1–4.3**. Color coding of the experimental points corresponds to f (see the legend in (b)).

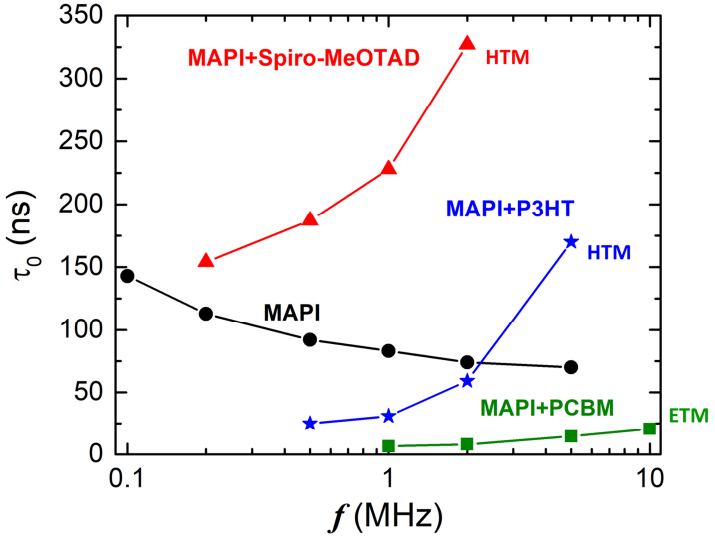

Figure 4.4. Characteristic PL lifetime τ_0 versus laser repetition rate f. Here τ_0 is taken as the time necessary for the normalized PL transients to decay to the arbitrary level I_0 (see **Figure 4.3a**) that is the same for all investigated samples.

Figure 4.4 highlights a qualitative difference between bulk recombination (pristine MAPI) and interface-affected recombination (MAPI with charge-selective layers) in the PL transients. Because the transient curves cannot be fully described by an analytical function, we choose an arbitrary level, I_0, that defines the characteristic time, τ_0, which is taken as the time necessary for the normalized PL transients to decay to the level I_0 (as assigned in **Figure 4.3a**). Remarkably, τ_0 demonstrates an opposite behavior for the reference (pristine) MAPI film compared to MAPI with charge transport materials. In the case of bulk recombination (pristine MAPI), the PL lifetime decreases with rising f, while in the case of interface-affected recombination (MAPI with transport materials) an increase of PL decay is revealed.

4.2.3. Kinetic Model for Carrier Recombination

The effect of repetition rate f on recombination dynamics of charge carriers is schematically explained in **Figure 4.5.** If f is low enough, most of the photogenerated charge carriers recombine before the consecutive laser pulse. As the frequency increases, a background population of charge carriers will built up and trap-state filling will occur. The excess of background carriers will accelerate band-to-band recombination because the probability to recombine is directly proportional to the product of charge carrier density. Simultaneously, interfacial traps remain filled, making subsequent electron capture ineffective. PL in MAPI at room temperature arises from direct band-to-band recombination of electrons and holes. A slower electron–hole recombination via indirect transition in MAPI was also proposed recently.[22,23] As long as the temperature remains constant, there is no mathematical difference between electron release via trap depopulation or indirect transition; therefore, we neglect the latter.

Now we consider charge carrier recombination in the framework of a kinetic model, including direct band-to-band recombination, electron trapping, trap depopulation via electron-hole recombination, and electron release from the traps to the conduction band.[4,18,24] Each of these processes is proportional to the charge carrier density with characteristic rate constants, as denoted in **Eq. 4.1–4.3**:

$$\frac{dn(t)}{dt} = -R_{\mathrm{np}}np - R_{\mathrm{tr}}n(N_{\mathrm{T}} - n_{\mathrm{T}}) + R_{\mathrm{rel}}n_{\mathrm{T}} \tag{4.1}$$

$$\frac{dn_{\mathrm{T}}(t)}{dt} = R_{\mathrm{tr}}n(N_{\mathrm{T}} - n_{\mathrm{T}}) - R_{\mathrm{dep}}n_{\mathrm{T}}p - R_{\mathrm{rel}}n_{\mathrm{T}} \tag{4.2}$$

$$\frac{dp(t)}{dt} = -R_{\mathrm{np}}np - R_{\mathrm{dep}}n_{\mathrm{T}}p \tag{4.3}$$

Here, n is the density of photoexcited electrons in the conduction band, p is the density of photoexcited holes in the valence band, n_{T} is the density of trapped electrons, and N_{T} is the constant density of traps in the perovskite film. R_{np}, R_{tr}, R_{dep}, and R_{rel} are the characteristic rates of band-to-band recombination, electron trapping, trap depopulation via electron-hole recombination, and electron release, respectively (see **Figure 4.5**).

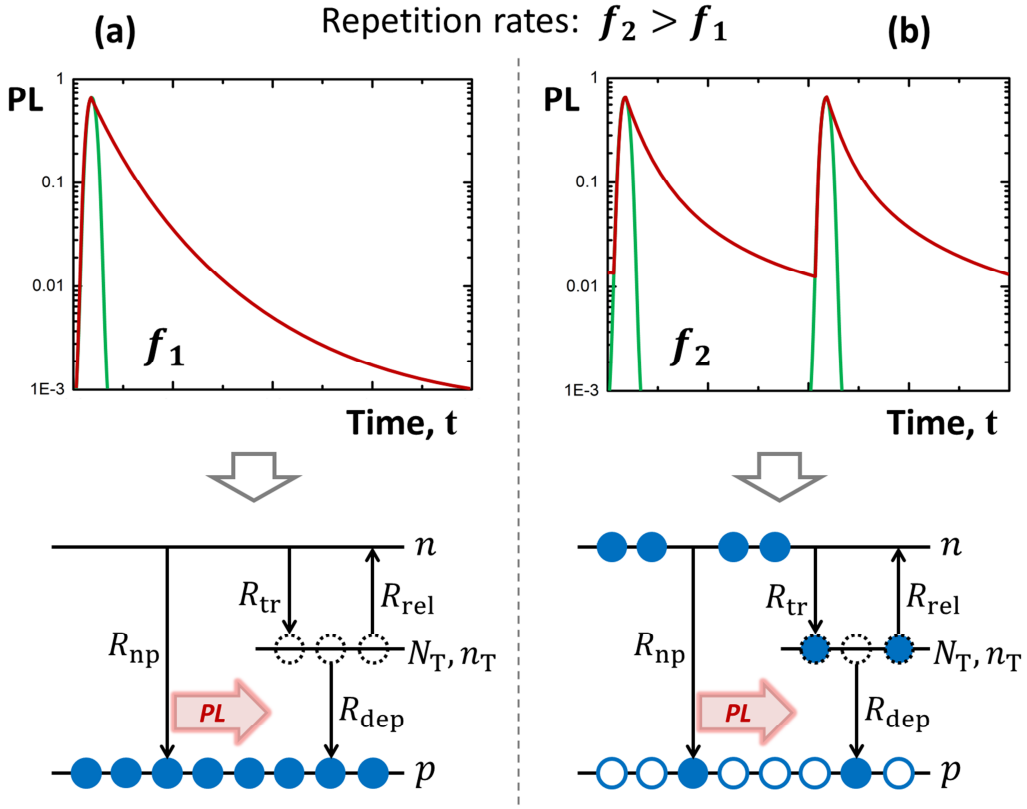

Figure 4.5. Schematic illustration of photocarrier dynamics within the regimes of low (a) and high (b) laser repetition rates f. (b) At higher f, the PL decay is incomplete (red line) and the residual population of photocarriers builds up. The conduction band and traps are partially filled by the arrival of the consecutive laser pulse. Traps are shown as a single energy level for simplicity.

Hole-trapping and charge carrier transport to the adjacent transport layers can also be included in the model, as shown in **Figure 4.6**. Then the number of parameters in the corresponding equations subsequently increases:

$$\frac{dn(t)}{dt} = -R_{np}np - R_{tr}^{n}n(N_T - n_T) + R_{rel}^{n}n_T - k_n n \tag{4.4}$$

$$\frac{dn_T(t)}{dt} = R_{tr}^{n}n(N_T - n_T) - R_{rel}^{n}n_T - R_{dep}n_T p_T \tag{4.5}$$

$$\frac{dp(t)}{dt} = -R_{np}np - R_{tr}^{p}p(P_T - p_T) + R_{rel}^{p}p_T - k_p p \tag{4.6}$$

$$\frac{dp_T(t)}{dt} = R_{tr}^{p}p(P_T - p_T) - R_{rel}^{p}p_T - R_{dep}n_T p_T. \tag{4.7}$$

Here, n is the density of photoexcited electrons in the conduction band, p is the density of photoexcited holes in the valence band, n_T and p_T are the densities of trapped electrons and holes, respectively, N_T and P_T are the constant densities of electron and hole traps in the perovskite film. R_{np}, R_{dep}, R_{tr}^{n}, R_{tr}^{p}, R_{rel}^{n}, R_{rel}^{p}, k_n, and k_p are the characteristic rates of band-to-band recombination, trap depopulation via electron-hole recombination, electron and hole trapping, release, and transfer to TM, respectively.

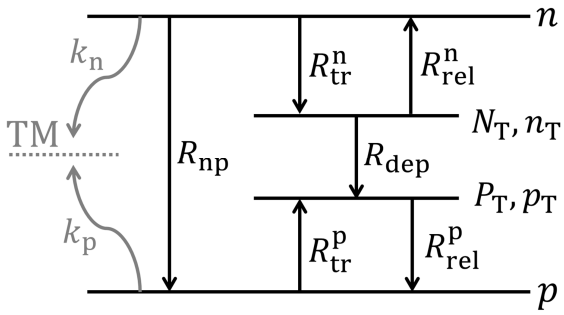

Figure 4.6. Schematic illustration of photocarrier dynamics taking into account hole trapping and charge transfer to the transport materials (TM).

Such increase in the number of equations and parameters does not change the fits qualitatively, but makes the numerical modeling more complicated. Therefore, for the sake of clarity, we consider only the simplified **Eq. 4.1–4.3** further on.

4.2.4. Numerical Modeling of PL Decay

The effect of laser repetition rate can be included in the model through the initial conditions for charge carrier densities: $n(0) = n_{inj} + n_0$; $p(0) = p_{inj} + p_0$; $n_T(0) = n_{T0}$. Here, $n_{inj} = p_{inj} = \text{const}$ are densities of electrons and holes generated with a single laser pulse; n_0, p_0, and n_{T0} are the excess of free and trapped carrier populations built up by the previous laser pulses. In the case of bulk recombination — when no interface states are involved — much faster PL decay with f can be attributed to the term $R_{np}np$ (**Eq. 4.1–4.3**). Both n and p increase with f; therefore, their product increases accordingly and the excited-state depopulation occurs faster.

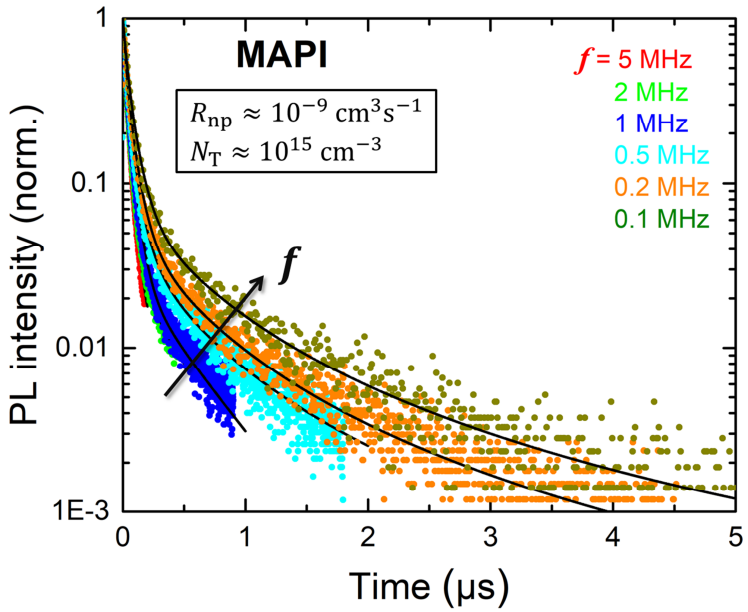

Figure 4.7. Normalized PL decays taken at different f in pristine MAPI (excitation at 505 nm, detection at 770 nm). Dots represent the experimental data; black curves show numerical fits to the kinetic model of **Eq. 4.1–4.3**. Color coding of the experimental points corresponds to f (see the legend).

In case of interface-affected recombination, slowing down of the PL decay with rising f is related to the interfacial trap filling, which reduces the number of unoccupied trap states, that is, $(N_T - n_T) \rightarrow 0$ in the case of trapped electrons. As a result, both interfacial charge trapping and interface-assisted recombination become less probable with increasing f, and the bulk interface-free transient is restored.

Figure 4.7 shows experimental transients in pristine MAPI, which were numerically modeled with the kinetic **Eq. 4.1–4.3** (see also **Figure 4.3a**). All characteristic constants, namely $R_{np}, N_T, R_{tr}, R_{rel,}$ and R_{dep}, were extracted from the fit of the PL decay at the lowest f = 0.1 MHz and kept constant during modeling at higher repetition rates. Thus, any transient variations at higher f can be attributed to the change of excess carrier densities n_0, p_0, and n_{T0}.

The values of characteristic rates and trap densities deduced from the numerical fit of TRPL in **Figure 4.7** are R_{np}~10^{-9} cm^3 s^{-1}, N_T~10^{15} cm^{-3}. However, we would like to emphasize that the PL transients can also be modeled with another sets of parameters (see **Figure 4.8**). Trap depopulation can be excluded from the model ($R_{dep} = 0$) without an apparent effect on PL transients (see **Figure 4.7** and **Figure 4.8**). Some of the parameters, for example, R_{np} and n_0 or R_{tr} and N_T, appear in **Eq. 4.1–4.3** as a product. These parameters are not mathematically independent and thus cannot be extracted separately. Additional processes, which we do not consider here, can be taken into account while modeling the transient PL in the case of MAPI with transport layers (see **Figure 4.6** and **Eq. 4.4.–4.7**).[25]

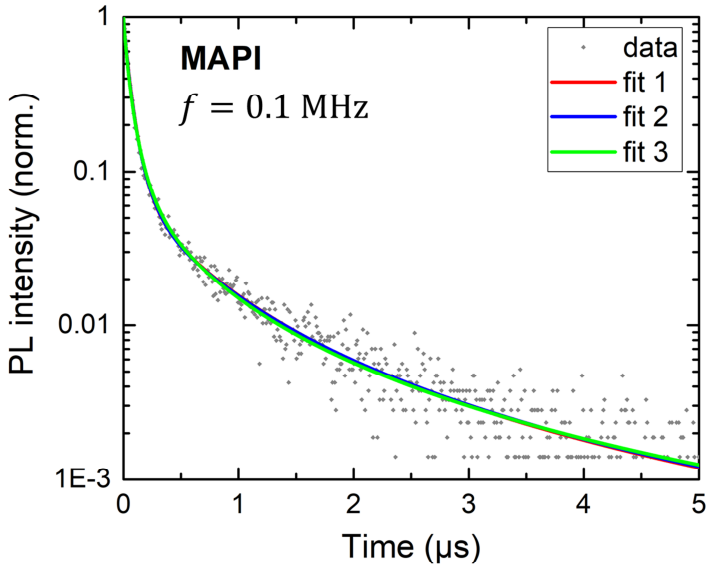

	R_{np} (cm^3 s^{-1})	N_T (cm^{-3})	R_{tr} (cm^3 s^{-1})	R_{rel} (s^{-1})	R_{dep} (cm^3 s^{-1})
Fit 1	4.14x10^{-9}	8.27x10^{15}	6.14x10^{-10}	2.73x10^6	2.80x10^{-10}
Fit 2	4.49x10^{-9}	2.39x10^{15}	1.99x10^{-9}	2.70x10^6	0
Fit 3	4.49x10^{-9}	1.09x10^{15}	5.82x10^{-9}	2.70x10^6	0

Figure 4.8. Three identical numerical fits built with different sets of parameters for PL decay in pristine MAPI taken at f = 0.1 MHz. Table shows the corresponding fit parameters.

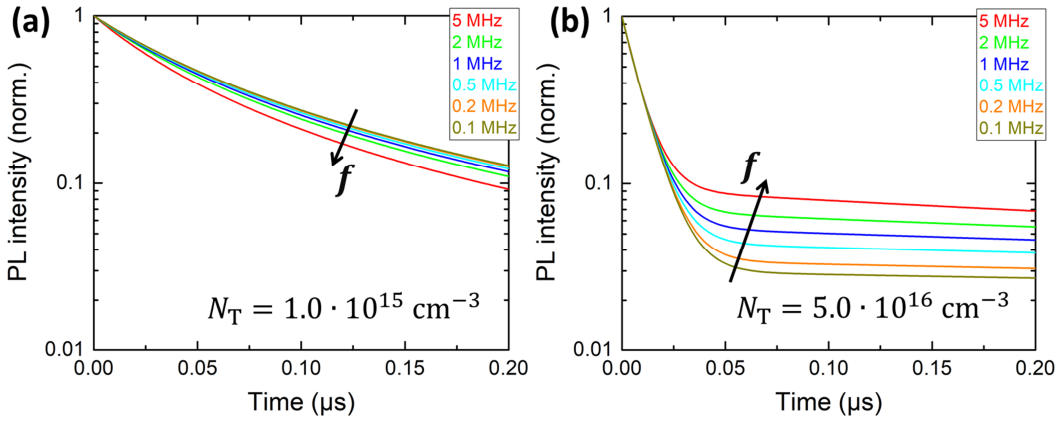

	R_{np} (cm^3 s^{-1})	N_T (cm^{-3})	R_{tr} (cm^3 s^{-1})	R_{rel} (s^{-1})	R_{dep} (cm^3 s^{-1})
(a)	4.0x10^{-9}	1.0x10^{15}	2.0x10^{-9}	2.8x10^{6}	0
(b)	4.0x10^{-9}	5.0x10^{16}	2.0x10^{-9}	2.8x10^{6}	0

Figure 4.9. Graph modeling the effect of pulse repetition rate on charge carrier dynamics. Transients (a) and (b) are calculated according to the kinetic model (**Eq. 4.1–4.3**) with the same set of parameters besides the number of electron traps N_T (see the table under the plot).

Nonetheless, **Figure 4.9** demonstrates that all major features and tendencies of PL transients, such as the fast and slow decay or the effects of repetition rate, can be qualitatively explained by solely varying the trap density N_T in the simplified set of kinetic **Eq. 4.1–4.3**.

Aside from varying the laser repetition rate, the intensity-dependent TRPL measurements can provide additional interesting information. However, we used moderate laser intensity in order to avoid sample damage and stay within solar cell operating conditions in our experiments. Instead, we performed a numerical modeling of the effect of pump intensity (or density of injected carriers, denoted as n_{inj}) on PL decay time using the kinetic model, as shown in **Figure 4.10**.

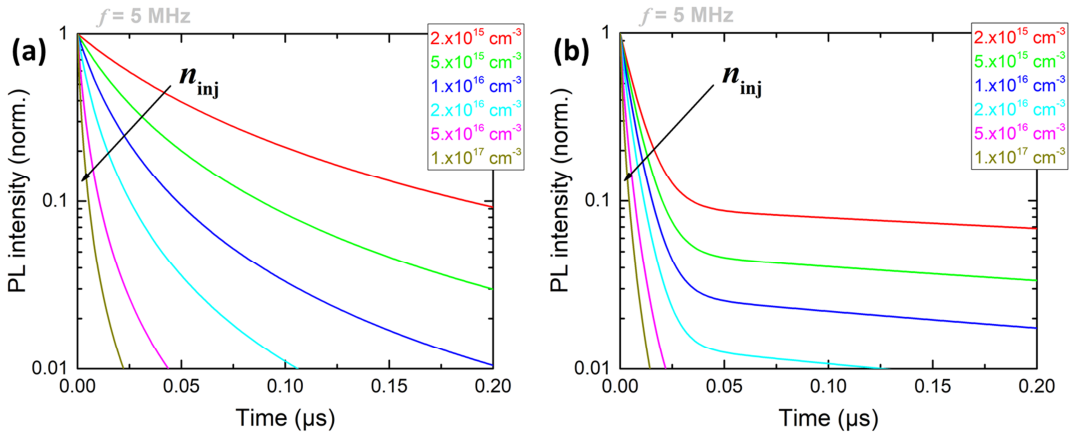

Figure 4.10. Graph modeling the effect of injected charge carrier density on decay dynamics. Transients (a) and (b) are calculated according to the kinetic model (**Eq. 4.1–4.3**) with the same set of parameters as in **Figure 4.9**, besides the varying number of injected electrons n_{inj}. Laser repetition rate was fixed at f = 5 MHz.

As follows from the modeling, increase of the pump light intensity leads to the same qualitative effect in the systems with low and high trap densities N_T. The initial free charge carrier densities and, according to **Eq. 4.1–4.3**, the recombination rate increases with the pump light intensity, which may superimpose the effect of trap filling. Therefore, increase of the pump light intensity does not lead to the same effects as increase of the laser repetition rate f.

4.3. Conclusion

In this chapter, we investigated the effect of laser repetition rate on charge carrier recombination dynamics in methylammonium lead-iodide perovskite films. The TRPL technique was used to study the charge carrier recombination in both pristine MAPI film and MAPI films with organic ETM or HTM on top, namely PCBM, spiro-MeOTAD, and P3HT. Bulk- and interface-affected recombination was separated in our TRPL experiment. The fast component of PL decay (up to 300 ns) is assigned to interfacial processes and the slower one to bulk perovskite recombination. Laser repetition rate was shown to shorten PL decay in pristine perovskite while significantly prolonging the charge carrier lifetime in MAPI with additional interfaces. We qualitatively explained this effect in the frame of a commonly used kinetic model. It was demonstrated that the PL lifetime in a broad range can be obtained for the same sample by optical trap filling. This study emphasizes the significant influence of laser repetition rate on charge carrier lifetime, which should be taken into account when studying charge carrier recombination dynamics in perovskites.

4.4. Materials and Methods

4.4.1. Sample Preparation

A perovskite layer was processed on a 1 x 1 in. glass substrate without any modifications. This substrate was cleaned in a sequence of deionized water, acetone, and isopropanol for 10 min each in an ultrasonic bath before use. Perovskite film was synthesized with a two-step interdiffusion process.[26] In the first step, we used a 400 mg/mL PbI_2 solution (N,N-dimethylformamide) with a small amount of CH_3NH_3I (molar ratio of 0.2 in reference to PbI_2). After spin-coating, the substrate was annealed for 15 min at 70°C. Afterwards, CH_3NH_3I (40 mg/mL dissolved in 2-propanol) was spin-coated and heated at 100°C for 60 min in a DMSO atmosphere to form the perovskite layer. After cooling down to room temperature, the substrate was broken into four parts. One part was used without any further preparation as a reference, while the other substrates were covered with different charge transport materials, commonly used in planar and mesoporous perovskite solar cells. PC60BM was used as the ETM. It was spin-coated from a 20 mg/mL 1,2-dichlorbenzene solution and subsequently annealed at 100°C for 60 min. The third perovskite film was covered with spiro-MeOTAD (80 mg/mL in chlorobenzene doped with bis(trifluoromethanesulfonyl)imide in acetonitrile, *tert*-butylpyridine, and FK209 (tris(2-(1H-pyrazol-1-yl)-4-*tert*-butylpyridine)- cobalt(III) tris(bis(trifluoromethylsulfonyl)imide) in acetonitrile) according to the procedure described elsewhere.[27] The last sample was spin-coated with P3HT dissolved in chlorobenzene with a concentration of 15 mg/mL and an annealing time of 5 min at 100°C.

4.4.2. PL Measurements

PL and transient PL were measured with a calibrated fluorescence spectrometer FLS980 (Edinburgh Instruments), equipped with two excitation sources: a continuous broad-spectrum xenon lamp Xe1 and a pulsed green laser EPL-510 (wavelength 505.2 nm, pulse width 105 ps). The laser repetition rate was tunable

with discrete steps ranging from 10 kHz to 10 MHz. Laser pulse fluence was 7.6 nJ/cm^2, which corresponds to a photogenerated carrier density of 2.0x10^{15} cm^{-3} for the given wavelength in CH_3NH_3I film. Time resolution for TRPL measurement was 1.6 ns (taken as full width at half-maximum of the setup response function).

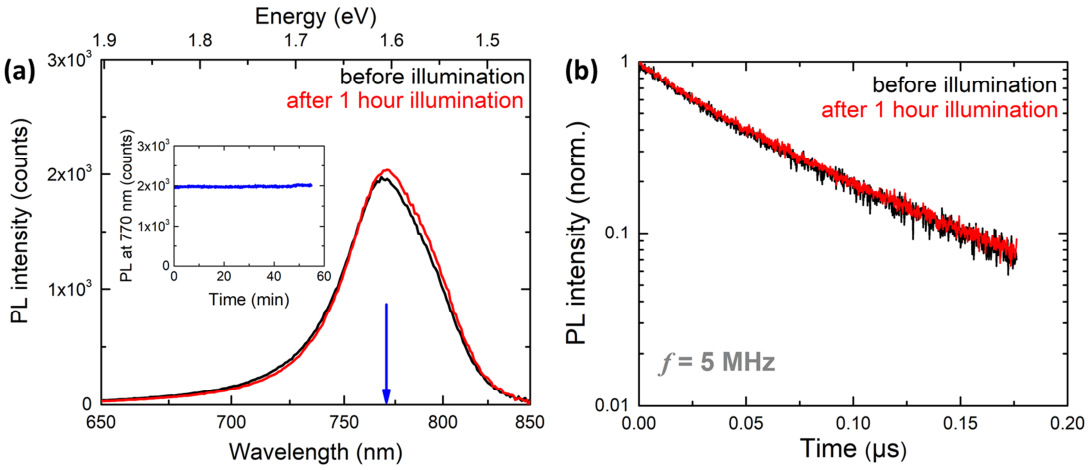

Figure 4.11. (a) PL spectra of a pristine uncovered MAPI film before illumination and after 1 h under illumination. Inset: absolute PL intensity at 770 nm during 1 h of illumination. (b) PL decay curves of the pristine uncovered MAPI film before illumination and after 1 h under illumination.

During the PL measurements, samples were exposed to ambient air and 40% humidity at room temperature. The acquisition time for every transient presented was 10 min. Thus, the total measurement time for every sample did not exceed 1 h. **Figure 4.11** demonstrates that PL spectrum, its absolute intensity, and decay shape remained unaltered within 1 h under illumination. Therefore, we do not consider here perovskite damage.

4.5. References

(1) National Renewable Energy Laboratory. *Research Cell Record Efficiency Chart.* https://www.nrel.gov/pv/assets/images/efficiency-chart.png (accessed Aug 8, 2018).

(2) Stranks, S. D.; Eperon, G. E.; Grancini, G.; Menelaou, C.; Alcocer, M. J. P.; Leijtens, T.; Herz, L. M.; Petrozza, A.; Snaith, H. J. Electron-Hole Diffusion Lengths Exceeding 1 Micrometer in an Organometal Trihalide Perovskite Absorber. *Science* **2014**, *342*, 341–344.

(3) Yamada, Y.; Nakamura, T.; Endo, M.; Wakamiya, A.; Kanemitsu, Y. Photocarrier Recombination Dynamics in Perovskite $CH_3NH_3PbI_3$ for Solar Cell Applications. *J. Am. Chem. Soc.* **2014**, *136*, 11610–11613.

(4) Stranks, S. D.; Burlakov, V. M.; Leijtens, T.; Ball, J. M.; Goriely, A.; Snaith, H. J. Recombination Kinetics in Organic-Inorganic Perovskites: Excitons, Free Charge, and Subgap States. *Phys. Rev. Appl.* **2014**, *2*, 1–8.

(5) Miyata, A.; Mitioglu, A.; Plochocka, P.; Portugall, O.; Wang, J. T.-W.; Stranks, S. D.; Snaith, H. J.; Nicholas, R. J. Direct Measurement of the Exciton Binding Energy and Effective Masses for Charge Carriers in Organic–inorganic Tri-Halide Perovskites. *Nat. Phys.* **2015**, *11*, 582–587.

(6) Stranks, S. D.; Snaith, H. J. Metal-Halide Perovskites for Photovoltaic and Light-Emitting Devices. *Nat. Nanotechnol.* **2015**, *10*, 391–402.

(7) De Wolf, S.; Holovsky, J.; Moon, S. J.; Löper, P.; Niesen, B.; Ledinsky, M.; Haug, F. J.; Yum, J. H.; Ballif, C. Organometallic Halide Perovskites: Sharp Optical Absorption Edge and Its Relation to Photovoltaic Performance. *J. Phys. Chem. Lett.* **2014**, *5*, 1035–1039.

(8) Zhang, Y.; Grancini, G.; Feng, Y.; Asiri, A. M.; Nazeeruddin, M. K. Optimization of Stable Quasi-Cubic

$FA_xMA_{1-x}PbI_3$ Perovskite Structure for Solar Cells with Efficiency beyond 20%. *ACS Energy Lett.* **2017**, *2*, 802–806.

(9) Jeon, N. J.; Noh, J. H.; Yang, W. S.; Kim, Y. C.; Ryu, S.; Seo, J.; Seok, S. Il. Compositional Engineering of Perovskite Materials for High-Performance Solar Cells. *Nature* **2015**, *517*, 476–480.

(10) Rakstys, K.; Paek, S.; Gao, P.; Gratia, P.; Marszalek, T.; Grancini, G.; Cho, K. T.; Genevicius, K.; Jankauskas, V.; Pisula, W.; et al. Molecular Engineering of Face-on Oriented Dopant-Free Hole Transporting Material for Perovskite Solar Cells with 19% PCE. *J. Mater. Chem. A* **2017**, *5*, 7811–7815.

(11) Tan, H.; Jain, A.; Voznyy, O.; Lan, X.; García de Arquer, F. P.; Fan, J. Z.; Quintero-Bermudez, R.; Yuan, M.; Zhang, B.; Zhao, Y.; et al. Efficient and Stable Solution-Processed Planar Perovskite Solar Cells via Contact Passivation. *Science* **2017**, *355*, 722–726.

(12) Ball, J. M.; Petrozza, A. Defects in Perovskite-Halides and Their Effects in Solar Cells. *Nat. Energy* **2016**, *1*, 16149.

(13) Steirer, K. X.; Schulz, P.; Teeter, G.; Stevanovic, V.; Yang, M.; Zhu, K.; Berry, J. J. Defect Tolerance in Methylammonium Lead Triiodide Perovskite. *ACS Energy Lett.* **2016**, *1*, 360–366.

(14) Kang, J.; Wang, L. W. High Defect Tolerance in Lead Halide Perovskite $CsPbBr_3$. *J. Phys. Chem. Lett.* **2017**, *8*, 489–493.

(15) Wen, X.; Sheng, R.; Ho-Baillie, A. W. Y.; Benda, A. A.; Woo, S.; Ma, Q.; Huang, S.; Green, M. A. Morphology and Carrier Extraction Study of Organic–Inorganic Metal Halide Perovskite by One- and Two-Photon Fluorescence Microscopy. *J. Phys. Chem. Lett.* **2014**, *5*, 3849–3853.

(16) Staub, F.; Hempel, H.; Hebig, J. C.; Mock, J.; Paetzold, U. W.; Rau, U.; Unold, T.; Kirchartz, T. Beyond Bulk Lifetimes: Insights into Lead Halide Perovskite Films from Time-Resolved Photoluminescence. *Phys. Rev. Appl.* **2016**, *6*, 1–13.

(17) Srimath Kandada, A. R.; Neutzner, S.; D'Innocenzo, V.; Tassone, F.; Gandini, M.; Akkerman, Q. A.; Prato, M.; Manna, L.; Petrozza, A.; Lanzani, G. Nonlinear Carrier Interactions in Lead Halide Perovskites and the Role of Defects. *J. Am. Chem. Soc.* **2016**, *138*, 13604–13611.

(18) Yamada, Y.; Yamada, T.; Shimazaki, A.; Wakamiya, A.; Kanemitsu, Y. Interfacial Charge-Carrier Trapping in $CH_3NH_3PbI_3$-Based Heterolayered Structures Revealed by Time-Resolved Photoluminescence Spectroscopy. *J. Phys. Chem. Lett.* **2016**, *7*, 1972–1977.

(19) Manger, L. H.; Rowley, M. B.; Fu, Y.; Foote, A. K.; Rea, M. T.; Wood, S. L.; Jin, S.; Wright, J. C.; Goldsmith, R. H. Global Analysis of Perovskite Photophysics Reveals Importance of Geminate Pathways. *J. Phys. Chem. C* **2017**, *121*, 1062–1071.

(20) Saba, M.; Aresti, M.; Quochi, F.; Marceddu, M.; Loi, M. A.; Huang, J.; Talapin, D. V.; Mura, A.; Bongiovanni, G. Light-Induced Charged and Trap States in Colloidal Nanocrystals Detected by Variable Pulse Rate Photoluminescence Spectroscopy. *ACS Nano* **2013**, *7*, 229–238.

(21) Prasankumar, R. P.; Taylor, A. J. *Optical Techniques for Solid State Materials Characterization*; CRC Press: Boca Raton, **2012**.

(22) Hutter, E. M.; Gélvez-Rueda, M. C.; Osherov, A.; Bulović, V.; Grozema, F. C.; Stranks, S. D.; Savenije, T. J. Direct–Indirect Character of the Bandgap in Methylammonium Lead Iodide Perovskite. *Nat. Mater.* **2016**, *16*, 115–121.

(23) Kirchartz, T.; Rau, U. Decreasing Radiative Recombination Coefficients via an Indirect Band Gap in Lead Halide Perovskites. *J. Phys. Chem. Lett.* **2017**, *8*, 1265–1271.

(24) Chirvony, V. S.; González-Carrero, S.; Suarez, I.; Galian, R. E.; Sessolo, M.; Bolink, H. J.; Martinez-Pastor, J. P.; Pérez-Prieto, J. Delayed Luminescence in Lead Halide Perovskite Nanocrystals. *J. Phys. Chem. C* **2017**, *121*, 13381–13390.

(25) Hutter, E. M.; Hofman, J.-J.; Petrus, M. L.; Moes, M.; Abellon, R. D.; Docampo, P.; Savenije, T. J. Charge Transfer from Methylammonium Lead Iodide Perovskite to Organic Transport Materials: Efficiencies, Transfer Rates, and Interfacial Recombination. *Adv. Energy Mater.* **2017**, 1–8.

(26) Xiao, Z.; Bi, C.; Shao, Y.; Dong, Q.; Wang, Q.; Yuan, Y.; Wang, C.; Gao, Y.; Huang, J. Efficient, High Yield Perovskite Photovoltaic Devices Grown by Interdiffusion of Solution-Processed Precursor Stacking Layers. *Energy Environ. Sci.* **2014**, *7*, 2619.

(27) Bi, D.; Tress, W.; Dar, M. I.; Gao, P.; Luo, J.; Renevier, C.; Schenk, K.; Abate, A.; Giordano, F.; Correa Baena, J.-P.; et al. Efficient Luminescent Solar Cells Based on Tailored Mixed-Cation Perovskites. *Sci. Adv.* **2016**, *2*, e1501170.

Chapter 5

Photon Propagation and Recycling in Perovskite Films by Spatially Resolved Photoluminescence

ABSTRACT

The photon recycling effect changes the photoluminescence (PL) spectrum within the perovskite film, which cannot be described solely by Lambert–Beer law. Using double-objective PL spectroscopy, we recorded emission spectra in methylammonium lead iodide (MAPI) and formamidinium lead iodide (FAPI) thin films at various distances from the excitation. PL was detected as far as 70 µm away from the excitation spot. Complex interplay between the intrinsic PL peak and emerging red-shifted emission was observed. Herein, we propose a general model that takes into account both photon propagation and recycling. Numerical simulation based on this model fit the experimental data very well for both studied materials, MAPI and FAPI. The proposed model can be applied to any particular perovskite film, because it uses easily measurable PL and absorption spectra as seeding parameters.

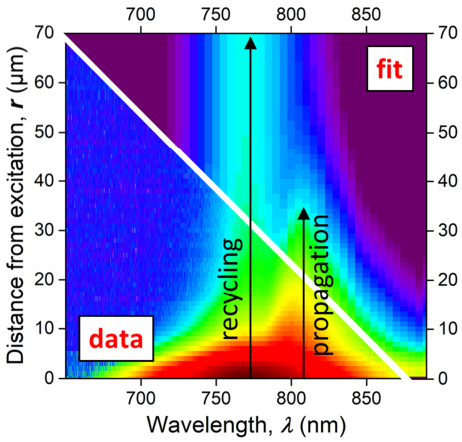

Partially based on:

Kudriashova, L. G.; Merkel, M. T.; Baianov, V.; Berger, S.; Tvingstedt, K.; Astakhov, G. V.; Baumann, A.; Dyakonov, V. Photon Propagation and Recycling in Perovskite Films by Spatially Resolved Photoluminescence. *In preparation.*

5.1. Introduction

Perovskite thin films owe their outstanding performance as solar cell absorbers[1] to long charge carrier lifetimes,[2–4] high internal luminescence quantum yields,[5–7] strong sharp-edge optical absorption,[8] and long carrier diffusion lengths.[9,10] The same properties facilitate photon confinement within the smooth and uniform perovskite film. In combination with high emission–absorption energetic overlap,[11–13] this confinement increases probability of self-absorption. The self-absorbed photons then produce new electron–hole pairs, some of which recombine radiatively, thus giving rise to a new generation of photons inside the film. Such interplay between photons and electron–hole pairs caused by self-absorption is usually referred to as the photon recycling effect.

Photon recycling has an indisputable importance for solar cells. It was shown to reduce the effective recombination current and therefore boost open-circuit voltage V_{OC} in gallium arsenide,[14] as well as in perovskite-based devices.[15] Taking photon recycling into account resolves an apparent discrepancy between Shockley's diode equation and the Shockley–Queisser limit in photovoltaics.[16] Photon recycling changes externally measured recombination parameters from intrinsic ones,[17,18] which leads to overestimated radiative recombination rates and underestimated photoluminescence (PL) quantum efficiencies and causes vast disagreement among the published values.

Magnitude of the photon recycling effect depends not only on intrinsic physical properties of material, but also on geometrical factors defining light-outcoupling: surface quality, relative refractive indexes of surrounding layers, film thickness, *etc*. For instance, external PL quantum yield of thin MAPI film was changed from 5% to 27% by Friend and coauthors using optimized light-outcoupling.[19] At the same time, Fang *et al.* reported negligible photon recycling in MAPI single crystals.[20] Therefore, a more general description of the effect, which will suit a broad range of samples, is challenging.

Phenomena related to light propagation in thin film can be visualized and quantified by double-objective spatially resolved PL spectroscopy,[10,21,22] where emission is collected at an arbitrary distance from the excitation spot. In such experiments, photon recycling was shown to manifest itself as a significant transformation of the luminescence spectrum, appearance of an additional PL peak with large red-shift (~20–30 nm), and photons detected at unusually long distances from excitation (exceeding 50 µm in thin films and 100 µm in microwires).[21,22] The Lambert–Beer law alone failed to describe spectral changes caused by photon recycling in their whole complexity.[21]

In the current Chapter, we applied double-objective spatially resolved PL spectroscopy in order to reveal light propagation in methylammonium lead iodide (MAPI) and formamidinium lead iodide (FAPI) thin films. Spatially resolved PL maps, which were recorded within 5 orders of magnitude in intensity as far as 70 µm away from the excitation spot, resolved two distinct peaks in local PL spectra. Here we propose a general quantitative

model that describes the spatial transformation of PL spectra in perovskite films. The model considers two main contributions: light propagation with subsequent absorption according to Lambert–Beer law and photon recycling mediated by diffusion of charge carriers. The intrinsic PL spectrum and macroscopic absorption coefficient of a perovskite film serve as seeding parameters for the numerical simulation. Therefore, the model can be readily applied to a particular sample under consideration without explicit regard to perovskite type or light-outcoupling efficiency.

5.2. Results and Discussion

5.2.1. Spatial Transformation of PL Spectra

Figure 5.1a shows a simplified scheme of relative objective–sample motion in our experiment. PL was excited with laser beam from the bottom (excitation) objective through a sapphire substrate. Both the excitation objective and the sample were attached to a movable piezo-stage, so that the laser position remained fixed during PL imaging, while the top (detection) objective was scanning the sample in horizontal plane. For further experimental details consult **Section 5.4**.

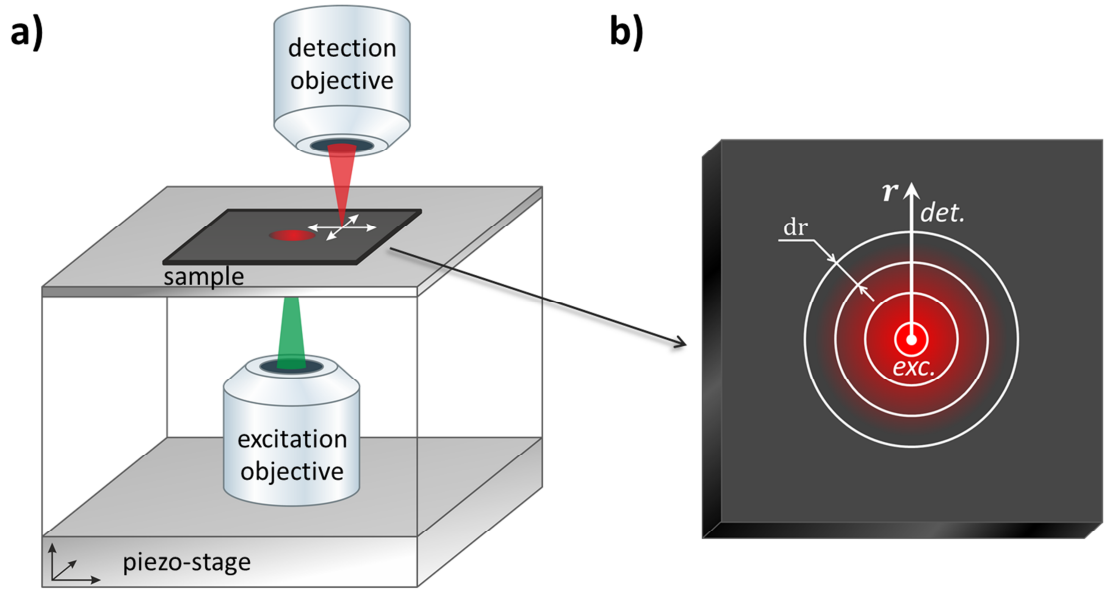

Figure 5.1. (a) Motion of the excitation and detection objectives relative to the sample. The detection spot moves in the sample plane, while the relative position of the excitation is fixed. (b) The cylindrical frame at the sample surface. The origin of coordinates is at the excitation spot; the detection position moves along the radial axis. The sample is divided into the concentric rings of infinitesimal thicknesses dr.

The films were illuminated for at least 5 min prior to every scan in order to exclude influence of the so-called light-soaking effect on experimental results.[10,23–25] Emission from both materials reached saturation after 4 min under illumination for the applied laser fluence (see **Figure 5.2**).

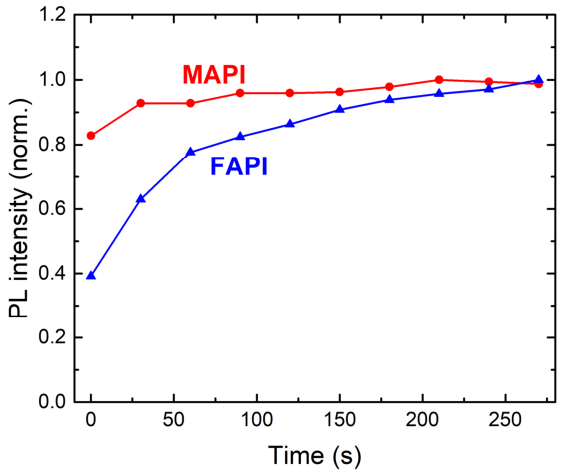

Figure 5.2. PL intensity of MAPI (red) and FAPI (blue) perovskite films saturating with time (light-soaking effect).

Figure 5.3 represents the resulting normalized PL spectra at various distances from the excitation. Intrinsic PL spectrum taken at the center of excitation (0 µm) has a single maximum at 770 nm. A second red-shifted peak at 800 nm appears 10 µm away from the excitation center. Nevertheless, the original PL persists, which leads to a doubled emission peak for intermediate distances of 10–40 µm from the excitation. Farther away, the original PL maximum at 770 nm again outweighs the red-shifted one.

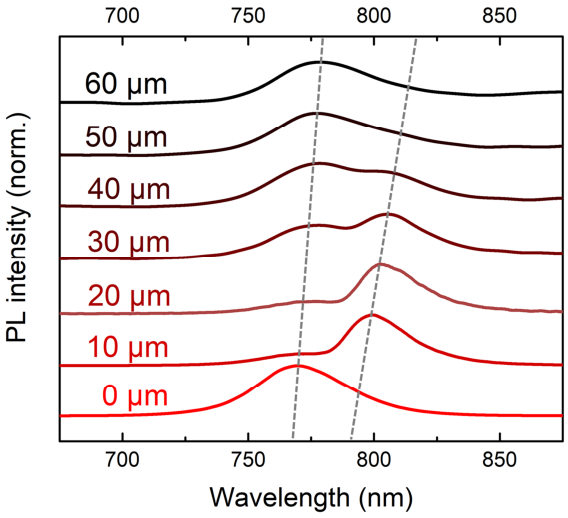

Figure 5.3. PL spectra taken at increasing distances from the excitation spot in MAPI film and normalized to the maximum value. The grey dashed lines show the approximate positions of two distinct PL peaks.

The abrupt red shift of the emission within the first 10 µm is caused by the sharp onset of absorption spectrum and its partial energetic overlap with the emission (see **Figure 5.4a**). Note that the absorption coefficient of MAPI film has a very low, but still nonzero value above 800 nm, which might be caused by sub-gap defect states previously observed for perovskites.[26] Knowing the absorption spectrum, one can quantitatively describe the red shift with Lambert–Beer equation in cylindrical coordinates.

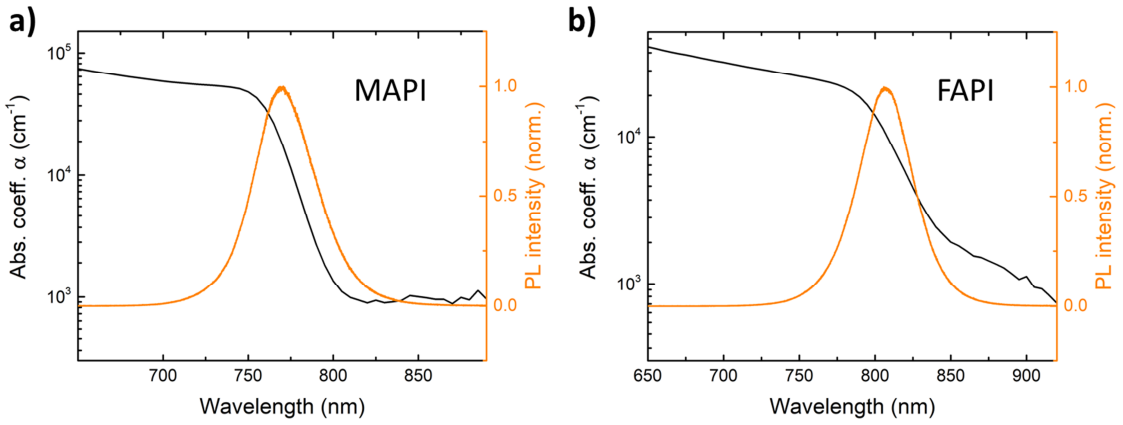

Figure 5.4. Absorption coefficient and normalized PL spectra of MAPI (a) and FAPI (b) films. Note, that the absorption coefficient is shown in logarithmic scale and has non-zero value in the infra-red region.

5.2.2. Lambert–Beer Law for Self-Absorption

We considered a cylindrical frame with the origin of coordinates placed in the center of the excitation spot (see **Figure 5.1b**). The horizontal scale of PL detection (~µm) was significantly larger than the film thickness (420 nm). Therefore, the vertical Z–axis was not considered. The configuration was also angle-independent in the sample plane, because the disorder of polycrystalline film made it uniform in all directions. The only remaining variable was the distance r from excitation.

First, we considered discrete concentric rings of radius r and infinitesimal width dr. Energy conservation law for such a ring is

$$I|_{\mathrm{r}}(\lambda)2\pi rh\,dt - I|_{\mathrm{r+dr}}(\lambda)2\pi(r+dr)h\,dt - I|_{\mathrm{r}}(\lambda)\alpha(\lambda)dr\cdot 2\pi rh\,dt = d\varepsilon \qquad (5.1)$$

Here $I|_{\mathrm{r}}$ is the intensity of light entering the layer dr, $I|_{\mathrm{r+dr}}$ is the intensity of light leaving it, h is the thickness of the film, dt is an arbitrary time interval, and $\alpha(\lambda)$ is the measured absorption coefficient.

In the stationary mode under continuous excitation, the total energy of the layer remains constant: $d\varepsilon = 0$. Thus, **Eq. 5.1** can be rewritten as the first order differential equation:

$$\frac{dI(\lambda)}{dr} + \frac{1}{r}I(\lambda) = -\alpha(\lambda)I(\lambda) \qquad (5.2)$$

Integration along the r–axis gives the solution for intensity of light propagating through the film:

$$I(r,\lambda) = I_0(\lambda)\frac{r_0}{r}\mathrm{e}^{-\alpha(\lambda)(r-r_0)} \qquad (5.3)$$

Here $I_0(\lambda)$ corresponds to the measured PL spectrum at the center of excitation and r_0 is the radius of laser spot. **Eq. 5.3** is Lambert–Beer law on cylindrical frame.

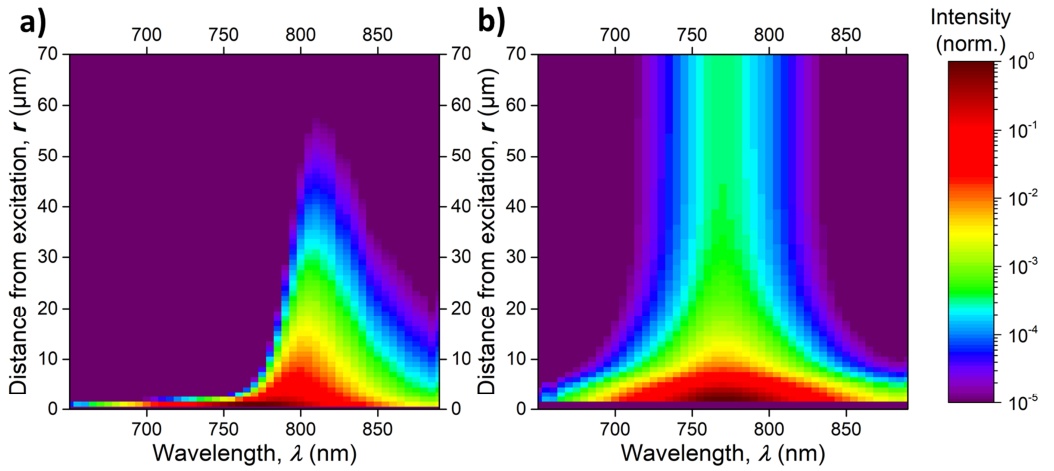

Figure 5.5. (a) Simulated PL map in MAPI film showing spectra at increasing distance r from excitation spot. Here, the emission is caused by photon propagation through the perovskite film. (b) Simulated PL map in MAPI film showing spectra at increasing distance r from excitation spot. Here, the emission is caused by photon recycling. Note, that the intensity scale is logarithmic.

Figure 5.5a shows an emission map simulated with **Eq. 5.3**. The seeding parameters for the numerical simulation are initial PL spectrum, $I_0(\lambda)$, normalized to maximal value and the measured absorption coefficient, $\alpha(\lambda)$.

The simulation describes the red-shifted emission component very well. Nevertheless, it predicts that the original PL at 770 nm rapidly decays after approximately 2 µm (**Figure 5.5a**), because the emitted photons propagate in the highly absorptive media. However, the PL peak was experimentally observed farther than 50 µm from the excitation (**Figure 5.3**). We assign this discrepancy to photon recycling effect: the secondary diffused charge carriers recombine and emit PL farther away from excitation.

5.2.3. Differential Model for Photon Recycling

We would like to emphasise that the distance at which PL is detected depends on detector sensitivity and acquisition time, that is, on the measurement parameters. Therefore, the distances can be conclusive only if the data are time- or spectrally resolved. The accurate statement in our case writes: the original PL peak persists at a twice longer distance from the excitation than the red-shifted one, which cannot be explained solely by Lambert–Beer prediction.

According to **Eq. 5.1**, the energy absorbed in one ring, $d\varepsilon_{\mathrm{abs}}$, is given by

$$d\varepsilon_{\mathrm{abs}} = I|_{\mathrm{r}}(\lambda)\alpha(\lambda)dr \cdot 2\pi rh\, dt \tag{5.4}$$

Substitution of $I|_{\mathrm{r}}(\lambda)$ with the **Eq. 5.3** gives

$$d\varepsilon_{\mathrm{abs}} = I_0(\lambda)\frac{r_0}{r}\mathrm{e}^{-\alpha(\lambda)(r-r_0)}\alpha(\lambda)dr \cdot 2\pi rh\, dt \tag{5.5}$$

Then, under the presumption that each absorbed photon creates a free electron–hole pair, the density of secondary electrons generated per unit time, $n_{\mathrm{sec}}(r)$, amounts to

$$n_{\mathrm{sec}}(r) = \int_{\lambda_{\min}}^{\lambda_{\max}} \frac{\lambda}{2\pi\hbar c} I_0(\lambda) \frac{r_0}{r} \alpha(\lambda) \mathrm{e}^{-\alpha(\lambda)(r-r_0)}\, d\lambda \tag{5.6}$$

Here $2\pi\hbar c/\lambda$ is the energy of an absorbed photon of wavelength λ. Hereafter, we normalize the resulting curve for $n_{\mathrm{sec}}(r)$ to its maximum value (the blue plot in **Figure 5.6**), because the emission intensity $I_0(\lambda)$ was recorded in arbitrary units.

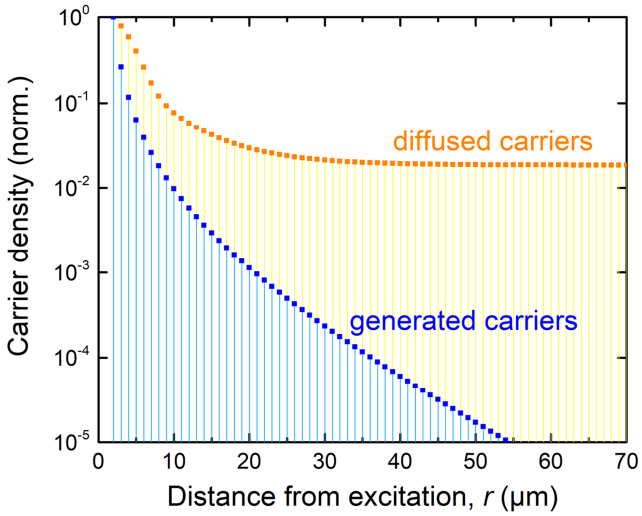

Figure 5.6. Calculated number of charge carriers generated via self-absorption (blue) and subsequently diffused (orange) at the distance r from excitation in MAPI film. The plots are normalized to the peak value.

Besides self-absorption with subsequent generation of secondary charge carriers, several other processes change the total number of electrons, dN, in one concentric ring of width dr: diffusion against the gradient of carrier density, recombination with holes, and trapping. Then, the overall change in the total number of electrons is described with the following equation:

$$D\frac{dn}{dr}\Big|_{\mathrm{r}} 2\pi r h\, dt - D\frac{dn}{dr}\Big|_{\mathrm{r+dr}} 2\pi(r+dr)h\, dt - \\ -kn^2|_{\mathrm{r}} 2\pi r h\, dr\, dt - qn|_{\mathrm{r}} 2\pi r h\, dr\, dt + S(r) 2\pi r h\, dr\, dt = dN \tag{5.7}$$

Here D is diffusion coefficient, n is the total density of electrons, k is the rate of radiative recombination, q is the rate of electron trapping, and $S(r)$ is the volume source of electrons (density of electrons generated per unit time).

Again, we consider only the stationary mode. Then $dN = 0$, $S(r)$ is time-independent, and $qn|_{\mathrm{r}} = 0$ effectively, because density of trapped and released carriers cancel each other in the stationary case. The resulting differential form of **Eq. 5.7** is

$$D\frac{d^2n}{dr^2} - D\frac{1}{r}\frac{dn}{dr} = -kn^2 + S(r) \tag{5.8}$$

Characteristic diffusion time for the two-dimensional case is $\tau_{\text{diff}} = {L_{\text{diff}}}^2/2D$, where L_{diff} is the corresponding characteristic length. The diffusion parameters for MAPI polycrystalline film earlier determined by Stranks *et al.* ($D = 0.017$ cm^{2}s^{-1} and $L_{\text{diff}} = 129$ nm)[9] result in $\tau_{\text{diff}} \approx 5$ ns.

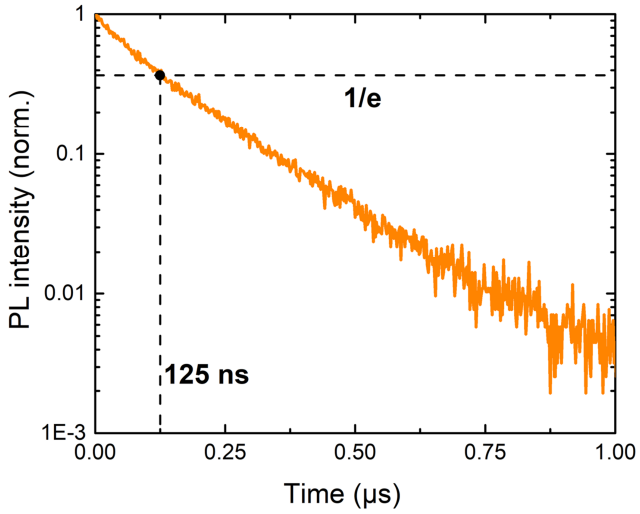

Figure 5.7. Transient PL curve in MAPI film. Characteristic decay time (125 nm) is assigned to the 1/e level.

Characteristic recombination time, τ_{rec}, was estimated from transient PL (**Figure 5.7**). τ_{rec} was defined as the time until PL decays to $1/\text{e}$ of its initial intensity, which was 125 ns. These estimations show that charge carrier diffusion in the MAPI film occurred significantly faster than recombination ($\tau_{\text{diff}} \ll \tau_{\text{rec}}$). Therefore, the item describing electron–hole recombination, kn^2, can be omitted in the first approximation of **Eq. 5.8**:

$$D\frac{d^2n}{dr^2} - D\frac{1}{r}\frac{dn}{dr} = S(r) \tag{5.9}$$

A substitution $\gamma = dn/dr$ linearizes the **Eq. 5.9**:

$$D\frac{d\gamma}{dr} - D\frac{1}{r}\gamma = S(r) \tag{5.10}$$

The homogenous equation corresponding to **Eq. 5.10** has an analytical solution:

$$\gamma(r) = \frac{r_0\gamma_0}{r} \equiv \frac{C}{r} \tag{5.11}$$

Here C is a constant independent of r. The solution of the inhomogeneous differential **Eq. 5.10** can be now expressed via $\gamma(r)$, but this time with C dependent on r:

$$\gamma(r) = \frac{C(r)}{r} \tag{5.12}$$

$$\frac{d\gamma(r)}{dr} = \frac{1}{r}\frac{dC(r)}{dr} - \frac{C(r)}{r^2} \tag{5.13}$$

Substitution of **Eq. 5.12**–**5.13** into **Eq. 5.10** results in a differential equation for $C(r)$:

$$\frac{dC(r)}{dr} = \frac{rS(r)}{D} \tag{5.14}$$

Since analytical form of $S(r)$ is unknown, the resulting solutions for $C(r)$, $\gamma(r)$, and $n(r)$ will be expressed via definite integrals:

$$C(r) = \frac{1}{D}\int_{r_0}^{r} S(\rho)\rho\, d\rho + C_0 \tag{5.15}$$

$$\gamma(r) = \frac{1}{rD}\int_{r_0}^{r} S(\rho)\rho\, d\rho + \frac{C_0}{r} \tag{5.16}$$

$$n(r) = \int_{r_0}^{r} \frac{C(\rho)}{\rho}\, d\rho + n_0 \tag{5.17}$$

So far, $n(r)$ is dependent on three parameters, D, C_0, and n_0. Hereafter, we consider physical border conditions in order to omit unnecessary constants.

For high distances ($r \to \infty$), no new electrons are generated via self-absorption, because the internal photon density there is extremely low. $S(r)$, thus, approaches 0 and the integral in **Eq. 5.15** approaches a constant value, S_0:

$$S_0 \equiv \int_{r_0}^{\infty} S(\rho)\rho\, d\rho \tag{5.18}$$

$$C(r \to \infty) = \frac{S_0}{D} + C_0 \tag{5.19}$$

Carrier density and their diffusive flux become negligible at high distances. Therefore, it is natural to assume that $n(r \to \infty) = 0, \gamma \equiv dn/dr\ (r \to \infty) = 0$, and, subsequently, $C(r \to \infty) = 0$. Then, the parameter C_0 can be expressed from **Eq. 5.19**:

$$C_0 = -\frac{S_0}{D} \tag{5.20}$$

Substitution of **Eq. 5.18** and **5.20** into **Eq. 5.15** gives the solution for $C(r)$:

$$C(r) = -\frac{1}{D}\int_{r}^{\infty} S(\rho)\rho\, d\rho \tag{5.21}$$

The **Eq. 5.17** for charge carrier density then will be rewritten as

$$n(r) = -\frac{1}{D}\int_{r_0}^{r} \frac{1}{x}\left(\int_{r}^{\infty} S(\rho)\rho\, d\rho\right) dx + n_0 \tag{5.22}$$

The first addend in **Eq. 5.22** reaches a constant limit, M, at $r \to \infty$:

$$M \equiv -\frac{1}{D}\int_{r_0}^{\infty}\frac{1}{x}\left(\int_{r}^{\infty} S(\rho)\rho\, d\rho\right)dx \tag{5.23}$$

Eq. 5.22 and **5.23** in combination with the border condition $n(r \to \infty) = 0$ result in a simple expression for n_0:

$$n_0 = -M \tag{5.24}$$

Then, the final simplified form for the solution $n(r)$ of the initial **Eq. 5.9** is

$$n(r) = -\frac{1}{D}\int_{r}^{\infty}\frac{1}{x}\left(\int_{r}^{\infty} S(\rho)\rho\, d\rho\right)dx \tag{5.25}$$

The only remaining parameter in **Eq. 5.25** is the diffusion coefficient D. For further numerical simulations, D was defined as 1, because it is a constant bare factor in **Eq. 5.25**.

The density of electrons generated in the film per unit time, $S(r)$, here is equivalent to the density of secondary electrons produced by self-absorption, $n_{\mathrm{sec}}(r)$, which was calculated earlier in **Eq. 5.6**. The integrals in **Eq. 5.25** can be rewritten to sums for discreet steps Δr along the r axis:

$$n(r) = \frac{1}{D}\sum_{x=r}^{r_{max}}\frac{1}{x}\left(\sum_{\rho=x}^{x_{max}} n_{\mathrm{sec}}(\rho)\rho\,\Delta\rho\right)\Delta x \tag{5.26}$$

Here, r_{max}, or else x_{max}, is the maximal distance from the center of excitation, for which the simulation is performed. Therefore, the numerical solution for **Eq. 5.26** is more accurate if the calculated n_{sec} extends farther away from the excitation spot. In our case, the densities of secondary carriers, n_{sec}, and subsequently diffused carriers, $n(r)$, were calculated up to 70 µm (see **Figure 5.6**). The step of discrete solution was $\Delta x = \Delta\rho = 1$ µm.

The simulation considers the laser excitation as a point source, which was not the case in the experiment. Therefore, the calculated $n(r)$ curve was convolved with a 5 µm-wide Gaussian curve in order to account for actual shape of the laser spot and the measured apparatus function of the setup (see **Section 5.4.3**).

5.2.4. Numerical Modeling of PL Map in MAPI

The process that concludes photon recycling is the radiative recombination of the diffused secondary charge carriers. The item $kn^2(r)$, which we omitted in the first approximation of **Eq. 5.8**, accounts for the radiative recombination. Hence, the resulting spectral map of recycled photons was calculated as $I_0(\lambda)\cdot n^2(r)$ and normalized to the maximum value (**Figure 5.5a**).

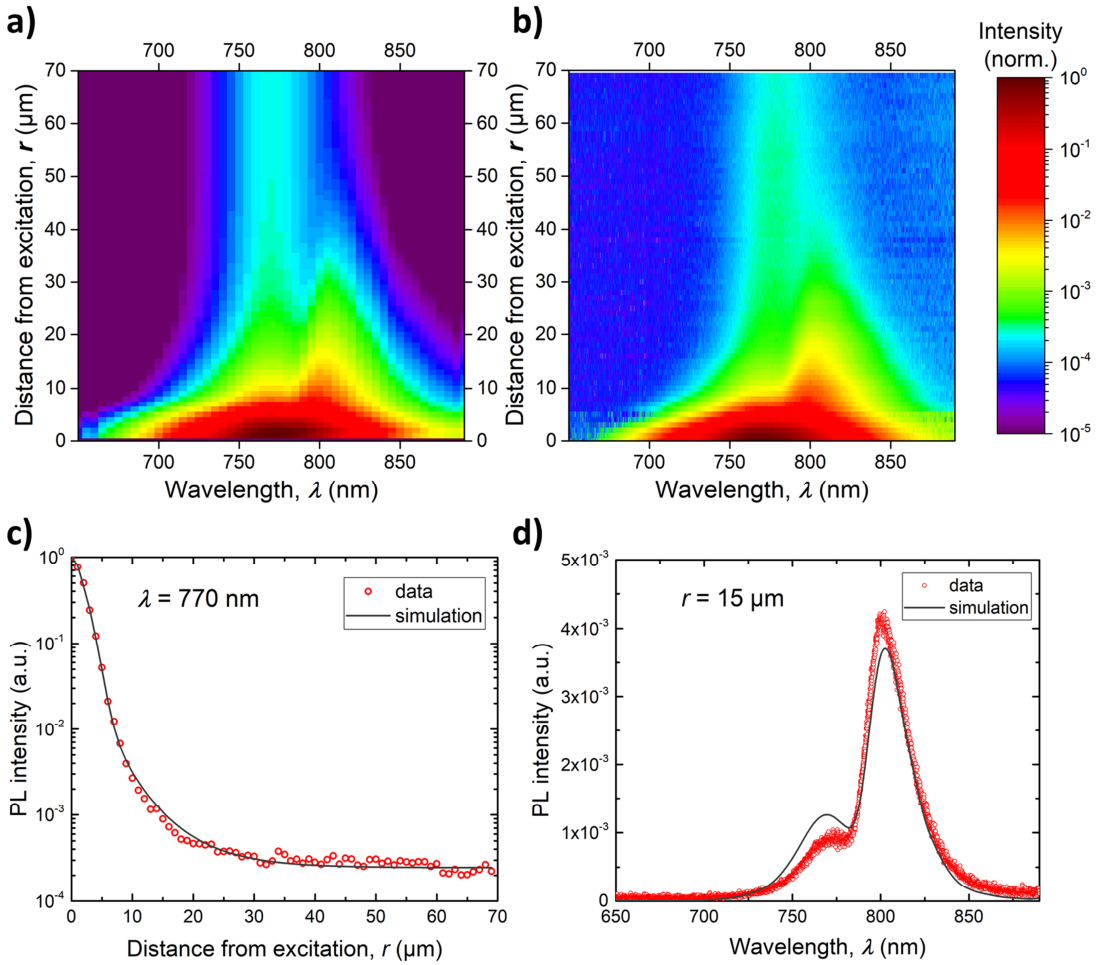

Figure 5.8. (a) Complete simulated PL map including both effects of light propagation and photon recycling in MAPI film. (b) The corresponding experimental PL map. (c) Comparison of the measured and simulated radial PL decay at 770 nm. (d) Comparison of the measured and simulated PL spectra 15 μm away from the excitation spot.

The sum of the emission due to photon propagation and due to recycling gives the complete PL map. The ratio of the two components in this sum has to be adjusted to optimally resemble the measured data, because all intermediate values were calculated in arbitrary units. **Figure 5.8a** shows the result of the simulation next to the experimental PL map (**Figure 5.8b**) presented in the same way, which emphasizes their excellent resemblance. The emission peak corresponding to photon recycling persists for much longer distances than the red-shifted one, both in the modelled and experimental PL maps. Note that the intensity scale in **Figure 5.8** is logarithmic and covers 5 orders of magnitude. **Figure** 5.8**c** provides an accurate visual comparison for the spatial decay of emission and the respective numerical fit at 770 nm. **Figure 5.8d**, in turn, demonstrates an emission spectrum taken 15 μm away from the excitation center. As can be seen, the proposed model, based on self-absorption and photon recycling, describes spatial transformation of emission in MAPI film very well.

5.2.5. Numerical Modeling of PL Map in FAPI

Figure 5.9 shows analogous PL scan for thin FAPI film. Although the emission from FAPI film was lower, which deteriorated the scan quality, the PL map was recorded up to 60 µm. Again, two distinct peaks in the PL map were observed. The image qualitatively resembled the experimental scan for MAPI film, though the intrinsic FAPI emission peaked at ~810 nm and the FAPI sample had stronger parasitic sub-gap absorption (**Figure 5.4b**).

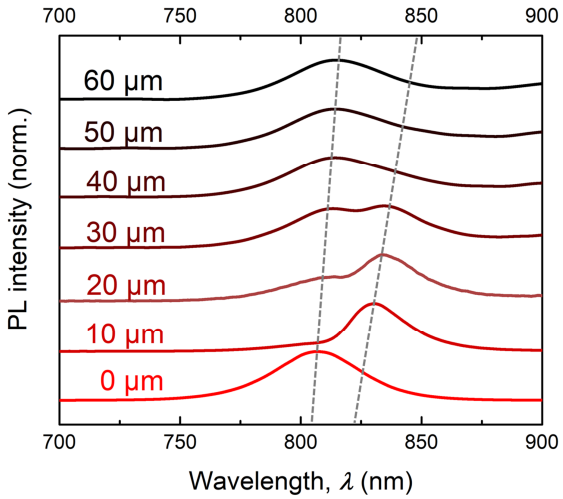

Figure 5.9. PL spectra taken at increasing distances from the excitation spot in FAPI film and normalized to the maximum value. The grey dashed lines show the approximate positions of two distinct PL peaks.

Data were successfully simulated with the model for light propagation and photon recycling we propose here (see **Figure 5.10** and **5.11**). Therefore, the same physical processes define the changes in local PL spectra both in MAPI and FAPI thin films.

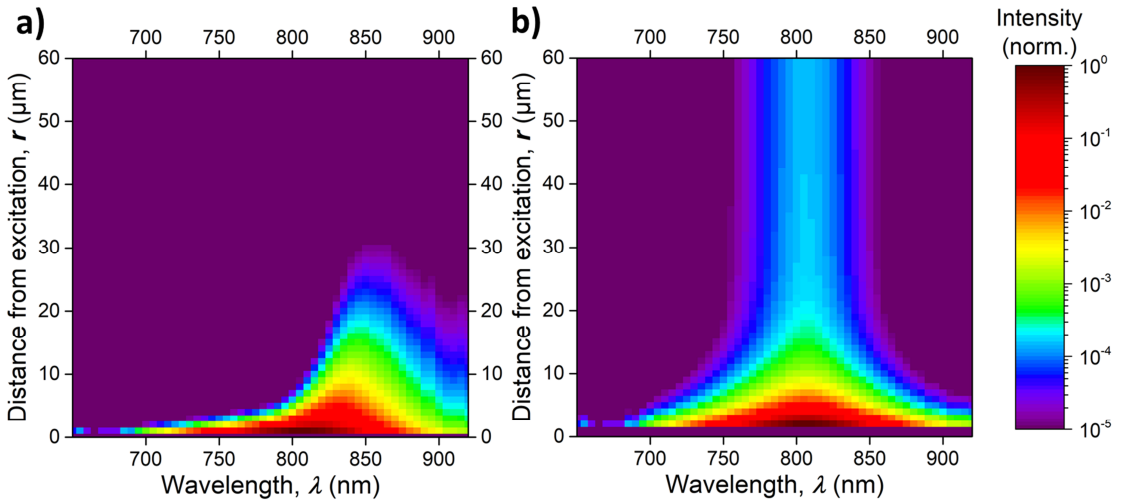

Figure 5.10. (a) Simulated PL map in FAPI film showing spectra at increasing distance *r* from excitation spot. Here, the emission is caused by photon propagation through the perovskite film. (b) Simulated PL map in FAPI film showing spectra at increasing distance *r* from excitation spot. Here, the emission is caused by photon recycling. Note, that the intensity scale is logarithmic.

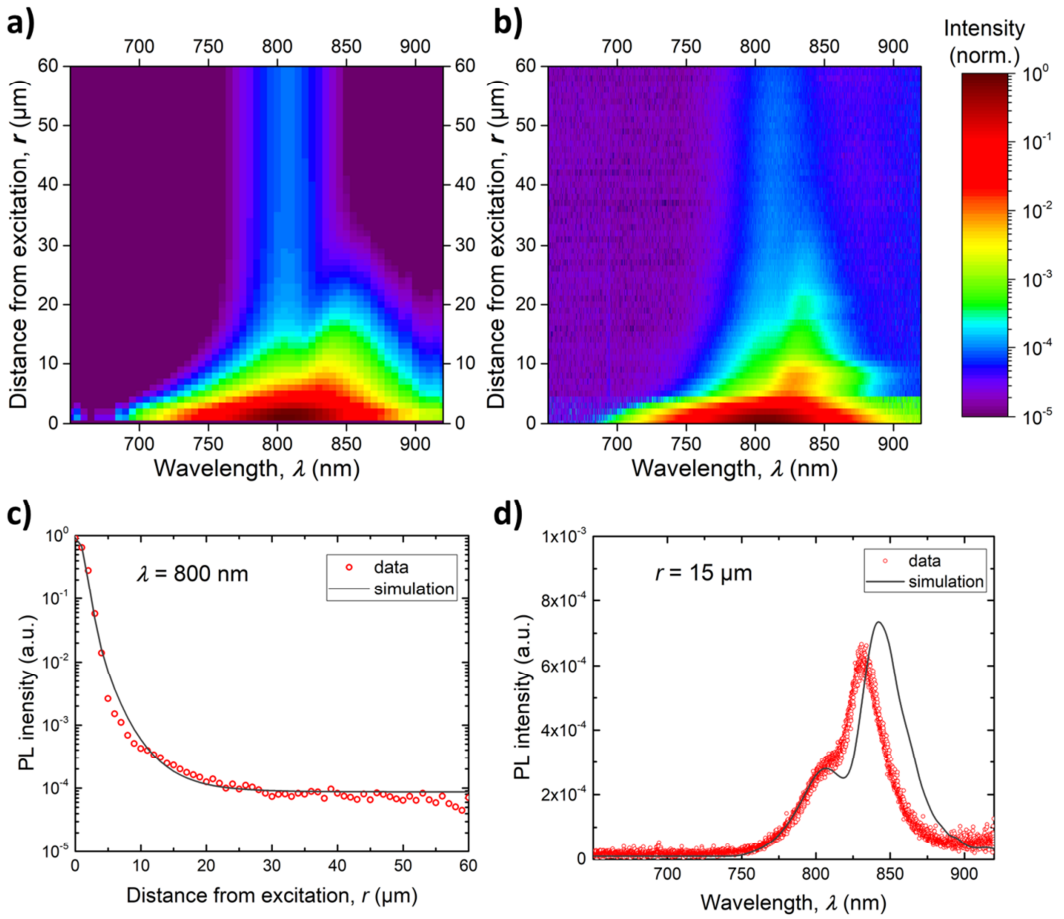

Figure 5.11. (a) Complete simulated PL map including both effects of light propagation and photon recycling in FAPI film. (b) The corresponding experimental PL map. (c) Comparison of the measured and simulated radial PL decay at 800 nm. (d) Comparison of the measured and simulated PL spectra 15 μm away from the excitation spot.

5.3. Conclusion

We measured the spatial transformation of PL spectra in MAPI and FAPI thin films at various distances from the excitation. PL was recorded within 5 orders of magnitude in intensity up to 70 μm away from the excitation spot. We propose a general model that takes into account photon propagation with subsequent self-absorption and photon recycling mediated by diffusion of secondary charge carriers. Numerical simulation based on this model showed excellent resemblance with the experimental data in perovskites of two different compositions, MAPI and FAPI. The proposed model can be applied to various perovskite films, because it uses easily measurable intrinsic PL spectrum and absorption coefficient as seeding parameters.

5.4. Materials and Methods

5.4.1. Sample Preparation

Perovskite film was synthesized via one-step deposition procedure. The entire deposition process and preparation of precursor solutions were carried out in the nitrogen atmosphere of a glovebox.

The precursor solution for MAPI film consisted of PbI_2 (lead iodide), CH_3NH_3I (methylammonium iodide, MAI), DMSO (dimethyl sulfoxide), and DMF (N,N-dimethylformamide) mixed in a molar ratio of 1:1:1:9.16. The precursor solution for FAPI film consisted of PbI_2, $CH(NH_2)_2I$ (formamidinium iodide, FAI), DMSO, and DMF mixed in a molar ratio of 1:1.03:1:9.44. The prepared solutions were stirred over night at room temperature.

Afterwards, the precursor solutions were spin-coated on a 1 x 1 in. 0.45 mm thick sapphire substrates. The substrates were cleansed in a sequence of deionized water, acetone and isopropanol for 10 min each in an ultrasonic bath before use. The spin-coater was operated at 4000 rpm for 30 seconds. At the 9th second of the spin-coating process, 200 µL of chlorobenzene (C_6H_5Cl) was dropped on the spinning substrate in order to abruptly wash out the DMF and provide formation of smooth and uniform film.

Immediately after spin-coating, MAPI film was placed at a 60^{o}C hot plate for 1 min in order to be purified from the remaining DMSO. Subsequent annealing at a hot plate of both MAPI (at 100^{o}C for 20 min) and FAPI (at 160^{o}C for 30 min) samples completed the precursor reaction and formation of perovskite layers. The precursor reaction manifested itself in a change of film color, from transparent or yellowish just after spin-coating to dark brown or black after annealing.

5.4.2. Spatially Resolved PL Imaging

The experimental setup was based on a confocal optical microscope LabRAM HR (Horiba Scientific). Raster-scan of the sample surface was provided with a piezo-stage.

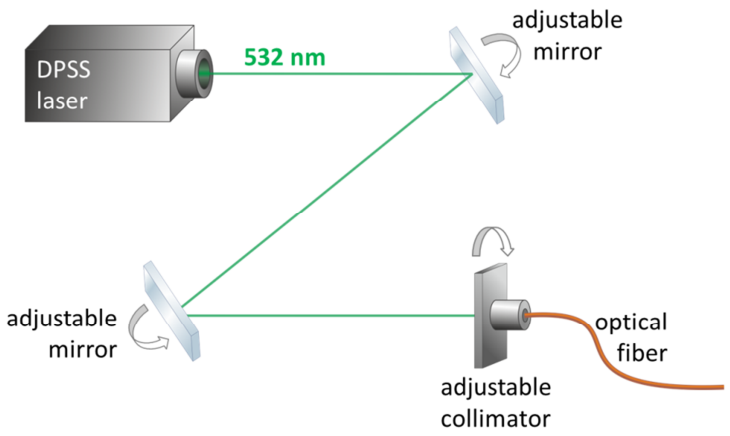

Figure 5.12. Scheme of laser coupling at the setup excitation shoulder.

A continuous wave Nd:YAG (neodymium-doped yttrium aluminium garnet) laser with $\lambda_{exc} = 532$ nm was used as a PL excitation source. The laser was coupled to a single mode optical fiber (see **Figure 5.12**) that in turn was connected to the excitation optics underneath the sample (see **Figure 5.13**). Excitation flux density at the fiber output was 80 µW µm^{-2}. Additionally, this light underwent slight unintended attenuation by the excitation optics and by the sample substrate.

Figure 5.13 shows the scheme of optical coupling for the excitation (bottom) objective. The horizontally incoming light is reflected by a right-angle prism to enter a 100x objective with numerical aperture $NA = 0.85$. The excitation objective is adjustable in the Z–direction in order to control the excitation depth in the sample and provide optimal focal positioning. The sample is placed horizontally right above the objective. Since both excitation objective and the sample are attached to a movable piezo-stage, the position of the laser spot at the sample remains fixed. At the same time, the detection (top) objective moves relative to the piezo-stage, allowing detection at various distances from the excitation spot.

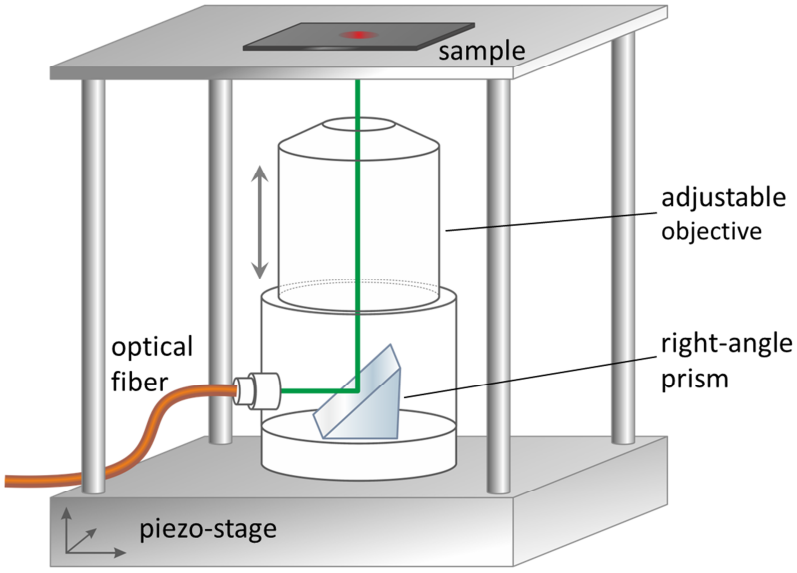

Figure 5.13. Excitation scheme. Both the excitation objective and the sample are attached to the same piezo-stage, so that their relative position is fixed.

5.4.3. Spatial Resolution

In the case of two separate objectives, spatial resolution of the setup is determined both by the focal diameter of the laser spot and the optical resolution of the detection system.

Given that the first mode of the laser is coupled into the fiber, one can estimate the focal size r of the excitation spot according to Rayleigh's criterion: $\delta = 0.61\lambda/\mathrm{NA}$, where λ is the excitation wavelength and NA is the numerical aperture of the objective. Using $\lambda_{\mathrm{exc}} = 532$ nm and $\mathrm{NA} = 0.85$, we obtained $\delta = 382$ nm.

Multiple factors, such as slight laser defocusing, tilt of sample surface, light propagation and scattering within the substrate, or possible imperfections of the excitation optics, can increase the actual laser spot far beyond the estimated diffraction-limited value δ. Furthermore, the overall spatial resolution of the setup is also affected by the detection optics.

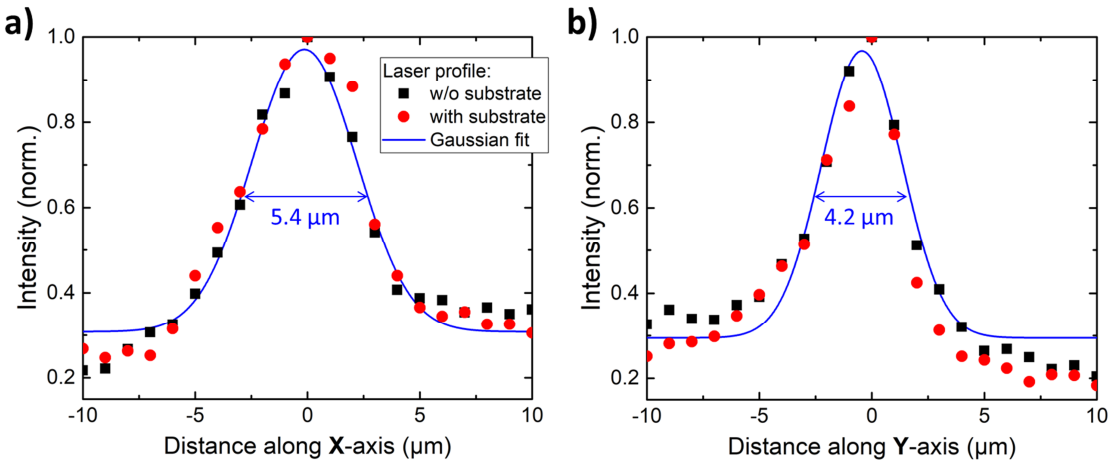

Figure 5.14. Laser profiles recorded without substrate (black squares) and with sapphire substrate (red circles) in the X (a) and Y (b) directions. Blue lines show Gaussian fit and the corresponding full-width at half-maximum (FWHM).

Therefore, we determined the spatial resolution of our system experimentally from the scan of laser profile with and without the sapphire substrate (see **Figure 5.14**). Note, that the substrate does not distort the recorded excitation profile, which was only the case for sapphire slides in our experiments. Hence, the sapphire substrates were preferred to glass or quartz slides in the current work.

The measured laser profile corresponded to the convolution of the laser spot in the focal plane and the apparatus function of the detection system. The full-width at half-maximum (FWHM) of the Gaussian fit to the profile were taken as the spatial resolution of the complete setup (5.4 µm in X–direction and of 4.2 µm in Y–direction). All sample scans were then conducted in Y–direction in order to attain better spatial resolution.

5.4.4. Measurement of Absorption Coefficient

We calculated absorption coefficient using transmission and reflection curves recorded in the 150 mm integrating sphere PELA 1001 (PerkinElmer, see **Figure 5.15**).

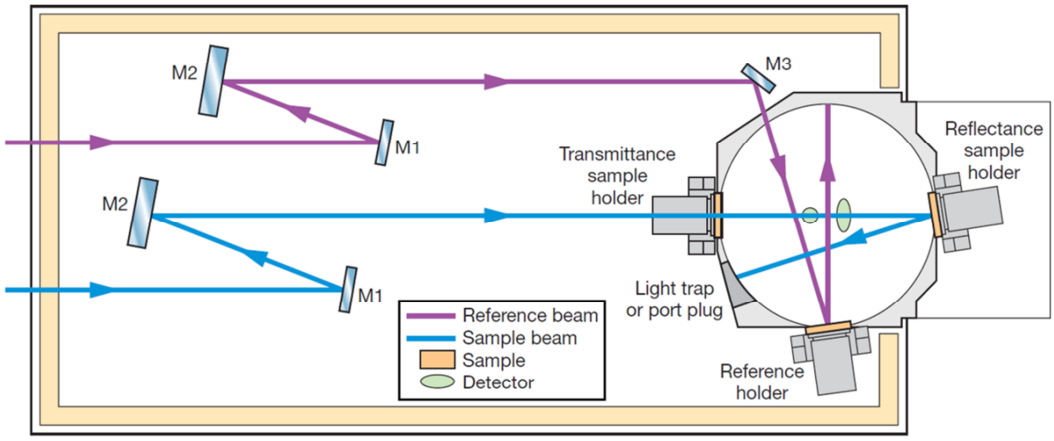

Figure 5.15. Optical design of 150 mm integrating sphere (adopted from www.perkinelmer.com).

Intensity of transmitted, I_{trans}, and reflected, I_{refl}, light of the broad-spectrum source was recorded for a perovskite layer on a sapphire substrate, as well as for the corresponding bare substrate. All measured values were normalized to the intensity I_0 of the reference source in order to obtain the total sample transmittance ($T \equiv I_{\text{trans}}/I_0$) and reflectance ($R \equiv I_{\text{refl}}/I_0$). In following, T_{S} is the transmittance of the bare sapphire slide, R_{S} is the reflectance of the bare sapphire slide, T_{PS} is the transmittance of the perovskite-on-sapphire sample, R_{PS} is the reflectance of perovskite-on-sapphire sample when perovskite is facing the incoming light, and R_{SP} is the reflectance of perovskite-on-sapphire sample when sapphire is facing the incoming light.

Lambert–Beer law for each experimental configuration writes

$$T_{\text{S}} = (1-\rho_{\text{S}})^2 \text{e}^{-\beta h} + \dots \quad (5.27)$$

$$R_{\text{S}} = \rho_{\text{S}} + \rho_{\text{S}}(1-\rho_{\text{S}})^2 \text{e}^{-2\beta h} + \dots \quad (5.28)$$

$$T_{\text{PS}} = (1-\rho_{\text{P}})(1-\rho_{\text{PS}})(1-\rho_{\text{S}})\text{e}^{-\alpha d}\text{e}^{-\beta h} + \dots \quad (5.29)$$

$$R_{\text{PS}} = \rho_{\text{P}} + \rho_{\text{PS}}(1-\rho_{\text{P}})^2 \text{e}^{-2\alpha d} + \dots \quad (5.30)$$

$$R_{\text{SP}} = \rho_{\text{S}} + \rho_{\text{PS}}(1-\rho_{\text{S}})^2 \text{e}^{-2\beta h} + \dots \quad (5.31)$$

Here, α and β are the absorption coefficients of sapphire substrate and perovskite layer, respectively; h and d are their thicknesses; ρ_{S} is the reflectance at sapphire–air interface; ρ_{P} is the reflectance at perovskite–air interface; ρ_{PS} is reflectance at the perovskite–sapphire interface. Note that here we use Greek letters for surface reflectance, that is, intensity of light reflected by an interface in a single reflection event divided by the intensity of the incident light. This value is not to be confused with the total reflectance of the sample, which is denoted with R.

We solved the system of **Eq. 5.27–5.31** numerically and obtained perovskite absorption coefficient, α.

Thickness d of perovskite film was probed with Dektak 150 Surface Profiler (Veeco) and averaged between 3–5 different positions on the sample for better accuracy.

5.4.5. Steady-State and Transient PL

PL and transient PL were measured with a calibrated fluorescence spectrometer FLS980 (Edinburgh Instruments). Steady-state PL was excited with a continuous xenon lamp at 505 nm. Transient PL was excited with a pulsed green laser EPL-510 (wavelength 505.2 nm, pulse width 105 ps, repetition rate 1 MHz). Laser pulse fluence was 7.6 nJ/cm^2, which corresponded to photogenerated carrier density of 2.0x10^{15} cm^{-3} for the given wavelength in MAPI film. During all PL measurements, samples were exposed to the ambient air of 40% humidity at room temperature.

5.5. References

(1) National Renewable Energy Laboratory. *Research Cell Record Efficiency Chart.* https://www.nrel.gov/pv/assets/images/efficiency-chart.png (accessed Aug 8, 2018).

(2) Stranks, S. D.; Burlakov, V. M.; Leijtens, T.; Ball, J. M.; Goriely, A.; Snaith, H. J. Recombination Kinetics in Organic-Inorganic Perovskites: Excitons, Free Charge, and Subgap States. *Phys. Rev. Appl.* **2014**, *2*, 1–8.

(3) deQuilettes, D. W.; Vorpahl, S. M.; Stranks, S. D.; Nagaoka, H.; Eperon, G. E.; Ziffer, M. E.; Snaith, H. J.; Ginger, D. S. Impact of Microstructure on Local Carrier Lifetime in Perovskite Solar Cells. *Science* **2015**, *348*, 683–686.

(4) Bi, Y.; Hutter, E. M.; Fang, Y.; Dong, Q.; Huang, J.; Savenije, T. J. Charge Carrier Lifetimes Exceeding 15 μs in Methylammonium Lead Iodide Single Crystals. *J. Phys. Chem. Lett.* **2016**, *7*, 923–928.

(5) Deschler, F.; Price, M.; Pathak, S.; Klintberg, L. E.; Jarausch, D. D.; Higler, R.; Hüttner, S.; Leijtens, T.; Stranks, S. D.; Snaith, H. J.; et al. High Photoluminescence Efficiency and Optically Pumped Lasing in Solution-Processed Mixed Halide Perovskite Semiconductors. *J. Phys. Chem. Lett.* **2014**, *5*, 1421–1426.

(6) deQuilettes, D. W.; Koch, S.; Burke, S.; Paranji, R. K.; Shropshire, A. J.; Ziffer, M. E.; Ginger, D. S. Photoluminescence Lifetimes Exceeding 8 μs and Quantum Yields Exceeding 30% in Hybrid Perovskite Thin Films by Ligand Passivation. *ACS Energy Lett.* **2016**, *1*, 438–444.

(7) Abdi-Jalebi, M.; Andaji-Garmaroudi, Z.; Cacovich, S.; Stavrakas, C.; Philippe, B.; Richter, J. M.; Alsari, M.; Booker, E. P.; Hutter, E. M.; Pearson, A. J.; et al. Maximizing and Stabilizing Luminescence from Halide Perovskites with Potassium Passivation. *Nature* **2018**, *555*, 497–501.

(8) De Wolf, S.; Holovsky, J.; Moon, S. J.; Löper, P.; Niesen, B.; Ledinsky, M.; Haug, F. J.; Yum, J. H.; Ballif, C. Organometallic Halide Perovskites: Sharp Optical Absorption Edge and Its Relation to Photovoltaic Performance. *J. Phys. Chem. Lett.* **2014**, *5*, 1035–1039.

(9) Stranks, S. D.; Eperon, G. E.; Grancini, G.; Menelaou, C.; Alcocer, M. J. P.; Leijtens, T.; Herz, L. M.; Petrozza, A.; Snaith, H. J. Electron-Hole Diffusion Lengths Exceeding 1 Micrometer in an Organometal Trihalide Perovskite Absorber. *Science* **2014**, *342*, 341–344.

(10) Handloser, K.; Giesbrecht, N.; Bein, T.; Docampo, P.; Handloser, M.; Hartschuh, A. Contactless Visualization of Fast Charge Carrier Diffusion in Hybrid Halide Perovskite Thin Films. *ACS Photonics* **2016**, *3*, 255–261.

(11) Tvingstedt, K.; Malinkiewicz, O.; Baumann, A.; Deibel, C.; Snaith, H. J.; Dyakonov, V.; Bolink, H. J. Radiative Efficiency of Lead Iodide Based Perovskite Solar Cells. *Sci. Rep.* **2015**, *4*, 6071.

(12) Tress, W.; Marinova, N.; Inganäs, O.; Nazeeruddin, M. K.; Zakeeruddin, S. M.; Graetzel, M. Predicting the Open-Circuit Voltage of $CH_3NH_3PbI_3$ Perovskite Solar Cells Using Electroluminescence and Photovoltaic Quantum Efficiency Spectra: The Role of Radiative and Non-Radiative Recombination. *Adv. Energy Mater.* **2015**, *5*, 1–6.

(13) Yao, J.; Kirchartz, T.; Vezie, M. S.; Faist, M. A.; Gong, W.; He, Z.; Wu, H.; Troughton, J.; Watson, T.; Bryant, D.; et al. Quantifying Losses in Open-Circuit Voltage in Solution-Processable Solar Cells. *Phys. Rev. Appl.* **2015**, *4*, 1–10.

(14) Durbin, S. M.; Gray, J. L. Numerical Modeling of Photon Recycling in Solar Cells. *IEEE Trans. Electron Devices* **1994**, *41*, 239–245.

(15) Kirchartz, T.; Staub, F.; Rau, U. Impact of Photon-Recycling on the Open-Circuit Voltage of Metal Halide Perovskite Solar Cells. *ACS Energy Lett.* **2016**, *1*, 731–739.

(16) Martí, A.; Balenzategui, J. L.; Reyna, R. F. Photon Recycling and Shockley's Diode Equation. *J. Appl. Phys.* **1997**, *82*, 4067–4075.

(17) Staub, F.; Hempel, H.; Hebig, J. C.; Mock, J.; Paetzold, U. W.; Rau, U.; Unold, T.; Kirchartz, T. Beyond Bulk Lifetimes: Insights into Lead Halide Perovskite Films from Time-Resolved Photoluminescence. *Phys. Rev. Appl.* **2016**, *6*, 1–13.

(18) Staub, F.; Kirchartz, T.; Bittkau, K.; Rau, U. Manipulating the Net Radiative Recombination Rate in Lead Halide Perovskite Films by Modification of Light Outcoupling. *J. Phys. Chem. Lett.* **2017**, *8*, 5084–5090.

(19) Richter, J. M.; Abdi-Jalebi, M.; Sadhanala, A.; Tabachnyk, M.; Rivett, J. P. H.; Pazos-Outón, L. M.; Gödel, K. C.; Price, M.; Deschler, F.; Friend, R. H. Enhancing Photoluminescence Yields in Lead Halide Perovskites by Photon Recycling and Light Out-Coupling. *Nat. Commun.* **2016**, *7*, 13941.

(20) Fang, Y.; Wei, H.; Dong, Q.; Huang, J. Quantification of Re-Absorption and Re-Emission Processes to Determine Photon Recycling Efficiency in Perovskite Single Crystals. *Nat. Commun.* **2017**, *8*, 1–9.

(21) Pazos-Outon, L. M.; Szumilo, M.; Lamboll, R.; Richter, J. M.; Crespo-Quesada, M.; Abdi-Jalebi, M.; Beeson, H. J.; Vru ini, M.; Alsari, M.; Snaith, H. J.; et al. Photon Recycling in Lead Iodide Perovskite Solar Cells. *Science* **2016**, *351*, 1430–1433.

(22) Dursun, I.; Zheng, Y.; Guo, T.; De Bastiani, M.; Turedi, B.; Sinatra, L.; Haque, M. A.; Sun, B.; Zhumekenov, A. A.; Saidaminov, M. I.; et al. Efficient Photon Recycling and Radiation Trapping in Cesium Lead Halide Perovskite Waveguides. *ACS Energy Lett.* **2018**, *3*, 1492–1498.

Chapter 6

Photophysics of Deep Blue OLED Emitter Employing Thermally Activated Delayed Fluorescence

ABSTRACT

We designed and synthesized a new organic light-emitting diode (OLED) emitter, SBABz4, containing spiro-biacridine donor (D) in the core surrounded by two benzonitrile acceptors (A). The dual A–DxD–A structure is shown to provide pure-blue emission in relation to its single A–D counterpart. Time-resolved photoluminescence (TRPL) recorded in the broad dynamic range from solutions and solid films revealed three emission components: prompt fluorescence, phosphorescence, and efficient thermally activated delayed fluorescence (TADF). The last is independently proven by temperature dependent TRPL and oxygen-quenching PL experiment. From the PL lifetimes and quantum yield, we estimated maximum external quantum efficiency of 7.1% in SBABz4-based OLEDs and demonstrated 6.8% in a test device.

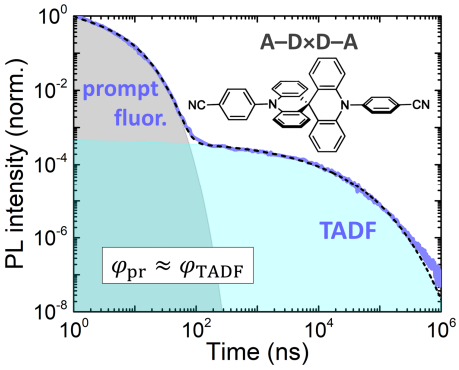

Partially based on:

Drigo, N. A.; Kudriashova, L. G.; Weissenseel, S.; Sperlich, A.; Huckaba, A. J.; Nazeeruddin, M. K.; Dyakonov, V. Photophysics of Deep Blue Acridane- and Benzonitrile-Based Emitter Employing Thermally Activated Delayed Fluorescence. *J. Phys. Chem. C* **2018**, *122*, 22796–22801.

6.1. Introduction

Thermally activated delayed fluorescence (TADF) changed the field of organic optoelectronics since the first reports by Adachi and coauthors in 2011.[1,2] Internal electroluminescence quantum efficiencies close to 100% and outstanding external quantum efficiencies (EQE) above 30% were achieved in the number of organic light-emitting diodes (OLEDs) employing metal-free TADF emitters.[3–8] This tremendous research progress was caused by high application potential of the new OLED generation, as well as by fascinating TADF photophysics.

Electrical injection of carriers produces singlet and triplet excitons with 1:3 branching ratio, reducing the emission probability to 25% of the entire excited population in organic semiconductors. Therefore, maximum internal electroluminescence efficiency of conventional OLED emitters does not exceed 25%, imposing a theoretical limit of 5–7.5% on EQE of the devices with 20–30% light outcoupling. Along with the triplet–triplet annihilation[9,10] and heavy-metal-complex phosphorescence,[11–14] TADF was shown to take advantage of dark triplet states, subsequently improving internal electroluminescence efficiency. TADF opened the way to fully overcome the efficiency-limiting spin statistics by thermally activated triplet-to-singlet up-conversion.

The efficiency of the triplet up-conversion, which occurs via reverse intersystem crossing (RISC), increases with decreasing singlet–triplet energy splitting, ΔE_{ST}.[15] ΔE_{ST} is commonly rendered low by a large dihedral angle between donor (D) and acceptor (A) moieties and consequently small HOMO–LUMO spatial overlap. This conformational requirement significantly limits the variety of possible donor–acceptor pairs for intramolecular TADF. On the other hand, energies of the HOMO and LUMO, together with the spatial overlap of the orbitals, define the optical properties essential for applications, emission color in particular. Molecular design of pure blue emitters is especially challenging since they should combine wide optical gap, narrow luminescence spectrum, and sufficient radiative efficiency. Therefore, despite the vast demand of organic optoelectronics, deep blue TADF emitters remain scarce.[5,7,16–18]

The majority of intramolecular TADF emitters currently presented in literature have a D–A–D structure with one or several donor moieties attached to a single acceptor in the core. Alternatively, molecules with dual emissive cores were shown to be superior in performance to their single-core analogs.[19,20] Moreover, several spiro-linked donors were developed to provide rigid stick-like structure and partial self-orientation of the molecules.[5,6] This approach enhanced light outcoupling, resulting in an efficiency breakthrough in the blue TADF-based OLEDs. However, photophysics of TADF emitters with a double donor in the core, as well as the role of spiro-linkage, is yet to be revealed.

Herein we present a novel compact deep-blue TADF emitter with a spiro-biacridine double donor core surrounded by two benzonitrile acceptors. We determine the correlation

between structure and luminescence properties of this dual A–DxD–A compound in relation to its single A–D counterpart. The spiro-bi-donor shifts the emission to the deep blue region. The blue emitter combines phosphorescence at low temperature with TADF at room temperature. We show that the emitter is applicable for OLEDs and demonstrates $\mathrm{EQE_{max}} = 6.8\%$ in a test device. We also compared photophysical properties of the neat emitters with those diluted in a (bis[2-(diphenylphosphino)phenyl]ether oxide) (DPEPO) matrix[21] in order to study the luminescence quenching effects and the influence of molecular environment.

6.2. Results and Discussion

6.2.1. Spiro-Donor for Deep Blue Emission

Figure 6.1a shows the molecular structures of 4,4'-(10*H*,10'*H*-9,9'-spirobi[acridine]-10,10'-diyl)dibenzonitrile (SBABz4) and its monomer counterpart, 4-(9,9-dimethylacridin-10(9*H*)-yl)benzonitrile (DMABz4). The deep HOMO of SBA or DMA donor was combined with shallow LUMO of benzonitrile acceptor to provide a wide optical gap sufficient for emission in the blue-green region.[5,22,23]

Mutual arrangement of H atoms at the *peri*-position of the acridine and at *o*-position of the acceptor's phenyl ring impedes D–A rotation, resulting in a semifrozen conformation with a large dihedral angle between the acridine and benzonitrile planes.[22] This nearly orthogonal D–A orientation is expected to break the HOMO–LUMO spatial overlap, thus decreasing the ΔE_{ST} and giving rise to TADF.

Figure 6.1b displays normalized photoluminescence (PL) and electroluminescence (EL) spectra of SBABz4, recorded in a neat film, a doped 5 wt % SBABz4:DPEPO matrix, dilute dichloromethane (DCM) solution, and SBABz4-based OLED. SBABz4 has pure blue emission peaking at 435 nm for the neat film. EL from the SBABz4-based device is in excellent agreement with the PL from the corresponding doped matrix. The pronounced red shift of PL from solid film to solution is caused by difference in the dielectric constants of the surrounding media ($\varepsilon_{\mathrm{film}} \approx 3$, while $\varepsilon_{\mathrm{DCM}} = 8.93$), which redistributes the electronic density of the excited state dipole. Significant positive solvatochromism is a general feature of emission from CT state.[24–26] **Figure 6.2** shows normalized PL spectra of SBABz4 recorded in solvents of various polarities. Here as well, the structureless luminescence spectra with pronounced spectral shift indicate the emission from CT state.

Figure 6.1b also compares PL spectra of DMABz4 and SBABz4 dilute solutions in DCM. Whereas SBABz4 shows blue emission ($\lambda_{\mathrm{max}} =$ 470 nm), emission from the DMABz4 is blue-green ($\lambda_{\mathrm{max}} =$ 500 nm). Photoluminescence quantum yields (PLQYs) of the deoxygenated SBABz4 and DMABz4 solutions are 55.7% and 83.8% respectively (**Table 6.1**). Altogether, spiro-linkage in the SBABz4 core provides blue shift of the emission while preserving reasonably high PLQY.

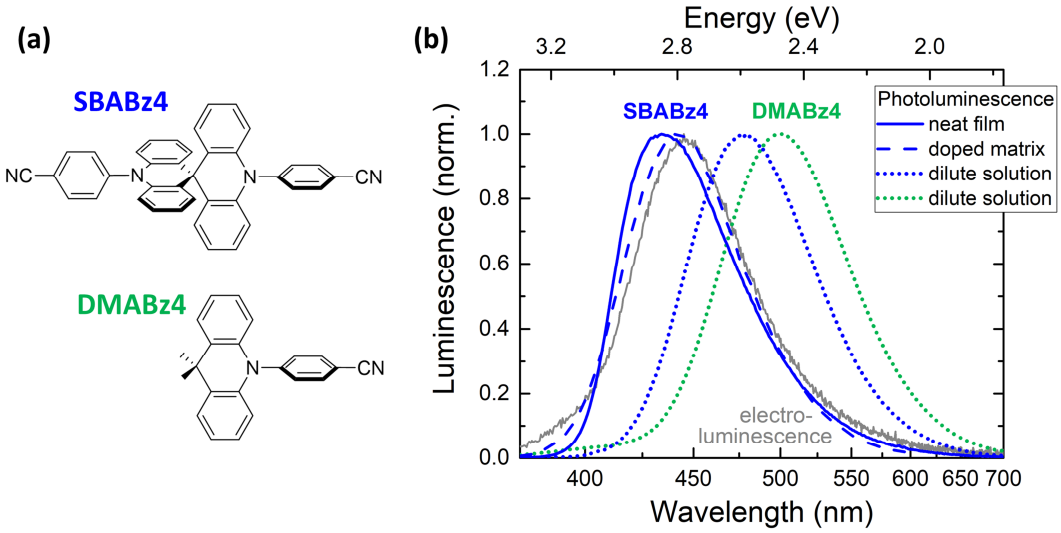

Figure 6.1. Structural formulas of SBABz4 and DMABz4 emitters. (b) Normalized PL spectra of SBABz4 (blue) and DMABz4 (green). Solid, dashed, and dotted colored lines represent neat film, doped 5 wt % SBABz4:DPEPO matrix, and dilute solutions in dichloromethane (DCM), respectively. Gray solid line shows electroluminescence from SBABz4-based OLED.

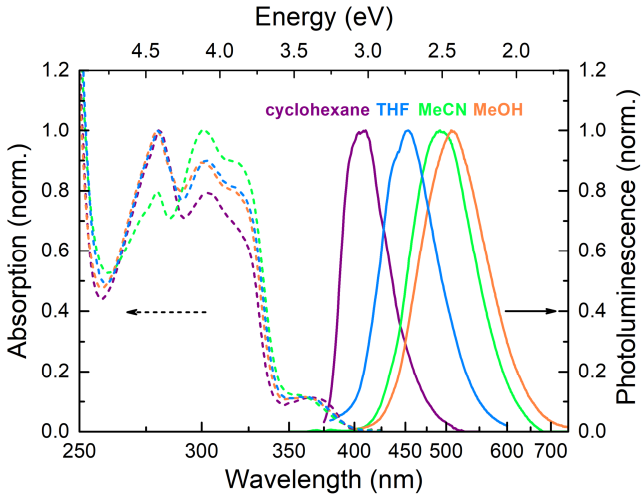

Figure 6.2. UV–vis absorption (dashed) and fluorescence (solid) spectra of SBABz4 normalized at the peak value. The strong bands below 345 nm is attributed to π-π* transition of a singlet locally excited state (^{1}LE). A weaker structureless band between 345–400 nm is ascribed to the intramolecular charge transfer (CT) from the acridine to the benzonitrile.

Currently prevailing TADF design with core-acceptor allows PLQY improvement via an increase in the number of donor units or the donor conjugation length.[2,18,23,27] The resulting bulky donor inevitably causes a red shift of luminescence, because of less localized and/or less stabilized HOMO. Alternatively, the rigid spiro-linkage maintains a large dihedral angle between the acridine subunits in the SBABz4 core, thus breaking the overlap between donor parts and introducing the desired blue shift into the emission. At the same time, the doubled number of emissive units still provides high luminescence efficiency. Therefore, SBABz4 was chosen for further study and fabrication of pure blue OLEDs.

Parameter	DMABz4	SBABz4
λ_{abs}, nm	280, 363	280, 302, 363
λ_{em}, nm[a]	411, 468, 500, 517, 532	407, 453, 475, 493, 509
PLQY[b] sol. w/o O_2	(83.8 ± 2.0)%	(55.7 ± 1.3)%
PLQY[b] sol. with O_2	(3.3 ± 0.5)%	(8.2 ± 0.2)%
PLQY neat film	—	(27.0 ± 1.7)%
PLQY 5 wt % in DPEPO	—	(40 ± 3)%

[a] Emission peak values for the dilute solutions in cyclohexane, tetrahydrofuran (THF), dichloromethane (DCM), acetonitrile, and methanol, respectively.
[b] Measured for the dilute solutions in DCM.

Table 6.1. Basic emission properties of SBABz4 and DMABz4.

6.2.2. PL from SBABz4 Dilute Solution

Figure 6.3 shows steady-state and time-resolved emission from a dilute solution of SBABz4 in DCM before and after oxygen exposure. Whereas the shape and position of PL spectrum remained unchanged under oxygen exposure, PLQY decreased 7-fold (from 55.7% to 8.2%, **Figure 6.3a** and **Table 6.1**). Note that the corresponding decay curves were recorded in the broad dynamic range of 5 orders of magnitude in time and 6 orders of magnitude in intensity. The transient PL contains prompt and delayed components (**Figure 6.3b**) with identical spectra (**Figure 6.3b**, inset). The fast component remains unaltered in the presence of oxygen. Therefore, we ascribe it to prompt fluorescence from ^{1}CT. In contrast, the slow component is substantially quenched by oxygen. Therefore, we assign it to TADF from ^{1}CT level populated via RISC. **Figure 6.3c** shows the same PL decay curve from the deoxygenated solution on a semilogarithmic scale, where the straight lines indicate the purely monoexponential character of both decay processes. Characteristic time constants (16.5 ns for the prompt fluorescence and 19.6 μs for TADF) were extracted from the double-exponential fit, fully consistent with luminescence from simple three-level system with triplet up-conversion.

Contribution of the prompt and delayed components in the total PLQY can be calculated numerically as the area under the decay curve or, in the simple case of monoexponential fit, expressed through the magnitudes and lifetimes of the components. Double exponential fit for normalized PL decay curve:

$$\mathrm{PL}_{\mathrm{norm}}(t) = A_{\mathrm{pr}} \exp\left(-\frac{t}{\tau_{\mathrm{pr}}}\right) + A_{\mathrm{TADF}} \exp\left(-\frac{t}{\tau_{\mathrm{TADF}}}\right) \quad (6.1)$$

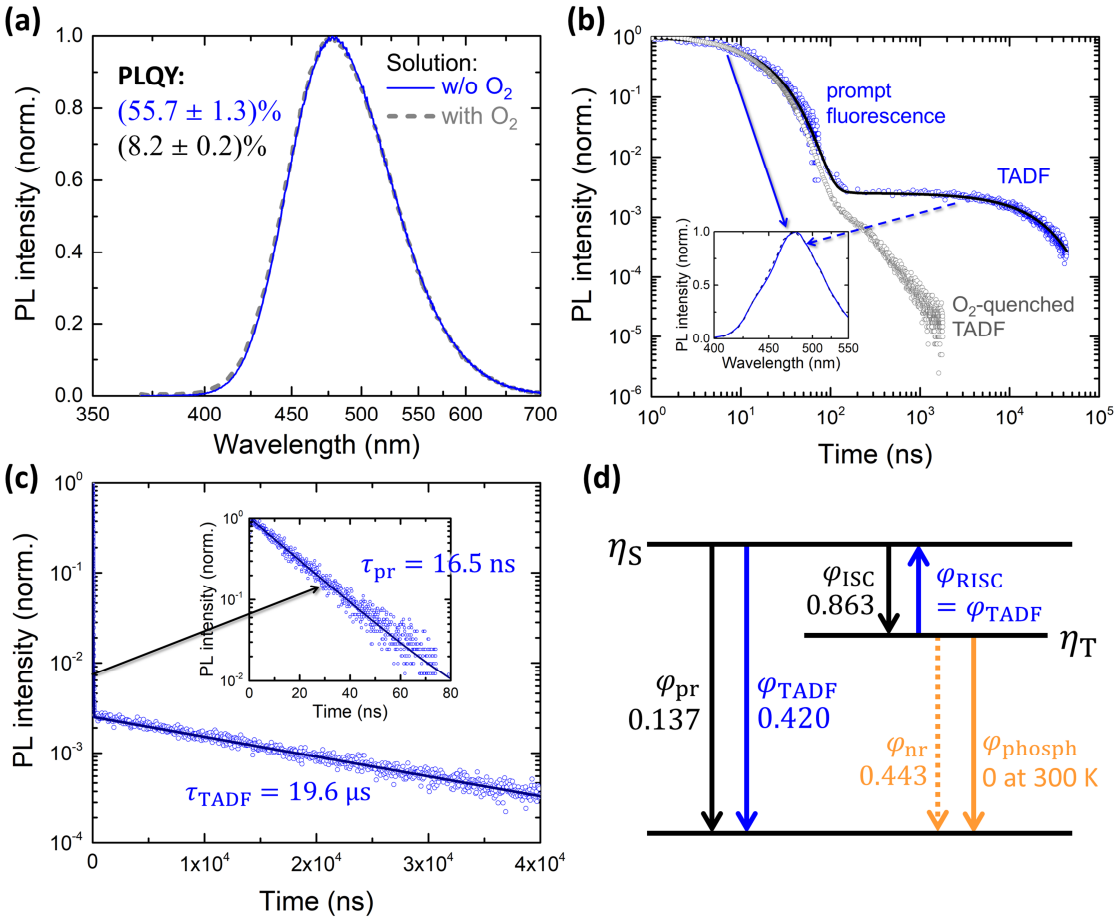

Figure 6.3. Steady-state and transient PL of dilute (10^{-5} mol L^{-1}) oxygenated (gray) and deoxygenated (blue) solutions of SBABz4 in DCM at room temperature. (a) PL spectra normalized at the peak value. (b) Transient PL detected at 475 nm. The inset: normalized PL spectra recorded within 0–25 ns (solid) and 150–1500 ns (dashed) of the decay. (c) Transient PL of the deoxygenated solution on a semilogarithmic scale. Inset: the prompt component. (d) Energy diagram depicting quantum efficiencies of the involved processes.

Contribution of the prompt fluorescence to the total PLQY:

$$\varphi_{\mathrm{pr}} = \frac{\int_0^\infty A_{\mathrm{pr}} \exp\left(-t/\tau_{\mathrm{pr}}\right) dt}{\int_0^\infty A_{\mathrm{pr}} \exp\left(-t/\tau_{\mathrm{pr}}\right) dt + \int_0^\infty A_{\mathrm{TADF}} \exp\left(-t/\tau_{\mathrm{TADF}}\right) dt} \cdot \mathrm{PLQY} \tag{6.2}$$

$$\Longrightarrow \varphi_{\mathrm{pr}} = \frac{A_{\mathrm{pr}}\tau_{\mathrm{pr}}}{A_{\mathrm{pr}}\tau_{\mathrm{pr}} + A_{\mathrm{TADF}}\tau_{\mathrm{TADF}}} \cdot \mathrm{PLQY} \tag{6.3}$$

Contribution of the delayed fluorescence to the total PLQY:

$$\varphi_{\mathrm{TADF}} = \frac{\int_0^\infty A_{\mathrm{TADF}} \exp\left(-t/\tau_{\mathrm{TADF}}\right) dt}{\int_0^\infty A_{\mathrm{pr}} \exp\left(-t/\tau_{\mathrm{pr}}\right) dt + \int_0^\infty A_{\mathrm{TADF}} \exp\left(-t/\tau_{\mathrm{TADF}}\right) dt} \cdot \mathrm{PLQY} \tag{6.4}$$

$$\Longrightarrow \varphi_{\mathrm{TADF}} = \frac{A_{\mathrm{TADF}}\tau_{\mathrm{TADF}}}{A_{\mathrm{pr}}\tau_{\mathrm{pr}} + A_{\mathrm{TADF}}\tau_{\mathrm{TADF}}} \cdot \mathrm{PLQY} \tag{6.5}$$

Here φ_{pr} and φ_{TADF} are quantum efficiencies of the prompt fluorescence and TADF;

A_{pr} and A_{TADF} are magnitudes of the decaying exponents; τ_{pr} and τ_{TADF} are respective lifetimes; PLQY is the measured total photoluminescence quantum yield. According to the **Eq. 6.3** and **6.5** and fitting parameters, quantum efficiency of TADF in the SBABz4 ($\varphi_{\mathrm{TADF}} = 0.420$) significantly exceeds that of prompt fluorescence ($\varphi_{\mathrm{pr}} = 0.137$). Now, under the assumption that phosphorescence is not present at room temperature, quantum efficiencies of ISC, RISC, and non-radiative triplet decay can be expressed via φ_{pr} and φ_{TADF}: $\varphi_{\mathrm{ISC}} = 1 - \varphi_{\mathrm{pr}}$, $\varphi_{\mathrm{RISC}} = \varphi_{\mathrm{TADF}}$, and $\varphi_{\mathrm{nr}} = \varphi_{\mathrm{ISC}} - \varphi_{\mathrm{TADF}}$ (**Figure 6.3d**). With that, maximum internal electroluminescence efficiency of the emitter in OLED can be expressed as following:[1]

$$\Phi_{\mathrm{EL,int}} = \eta_{\mathrm{S}}\varphi_{\mathrm{pr}} + \eta_{\mathrm{S}}\varphi_{\mathrm{ISC}}\varphi_{\mathrm{RISC}} + \eta_{\mathrm{T}}\varphi_{\mathrm{RISC}} \qquad (6.6)$$

Here η_{S} and η_{T} are portions of singlets and triplets produced via electrical injection (0.25 and 0.75, respectively). We obtained $\Phi_{\mathrm{EL,int}} = 44\%$ for SBABz4, which results in the estimation of $\mathrm{EQE}_{\mathrm{max}} = 8.8\%$ in the devices with assumed 20% light outcoupling. The estimation exceeds the 5% limit for first generation OLEDs. A fabricated SBABz4-based device with nonoptimized layer thicknesses and doping concentration showed $\mathrm{EQE}_{\mathrm{max}} = 6.8\%$ close to the estimation (**Figure 6.8**).

One may argue, than any estimate for device performance derived from solution properties is unreasonable. Indeed, the emitting layer of OLED is a solid thin film. Nevertheless, photophysical properties of any solid film are strongly affected by molecular aggregation, level of disorder, orientation of the emitters within the film, and so on. The reported photophysical parameters of solid films usually vary from publication to publication because of slightly different film preparation conditions. On contrary, the photophysical parameters measured for dilute solution are defined by intrinsic properties of the compound and provide clear idea for performance of the emitter itself. In any case, we will discuss the corresponding estimates for the solid films in the following sections.

6.2.3. PL from SBABz4 Thin Films

Figure 6.4 demonstrates transient PL and normalized PL spectra at different stages of decay for a solid 5 wt % SBABz4:DPEPO film at room (298 K) and low (77 K) temperatures. Transient PL at both temperatures contains fast and slow components. The fast component, peaking at 435 nm, dominates within the first 100 ns of decay regardless of the temperature. We ascribe this component to the prompt fluorescence from the ^{1}CT level. PL spectrum of the slow component at 77 K has noticeable red shift relative to the prompt one. Therefore, we assume that the slow component at low temperature is phosphorescence from lower-lying triplet. In contrast, the spectrum of the slow PL component at room temperature practically coincides with the prompt fluorescence. Thus, the delayed emission at room temperature originates from the same ^{1}CT level as the prompt fluorescence. Therefore, we assign it to TADF, mediated by slow reverse intersystem crossing. The corresponding energy diagram is depicted in the **Figure 6.4**. Neat SBABz4 film qualitatively showed the same behavior (**Figure 6.5**).

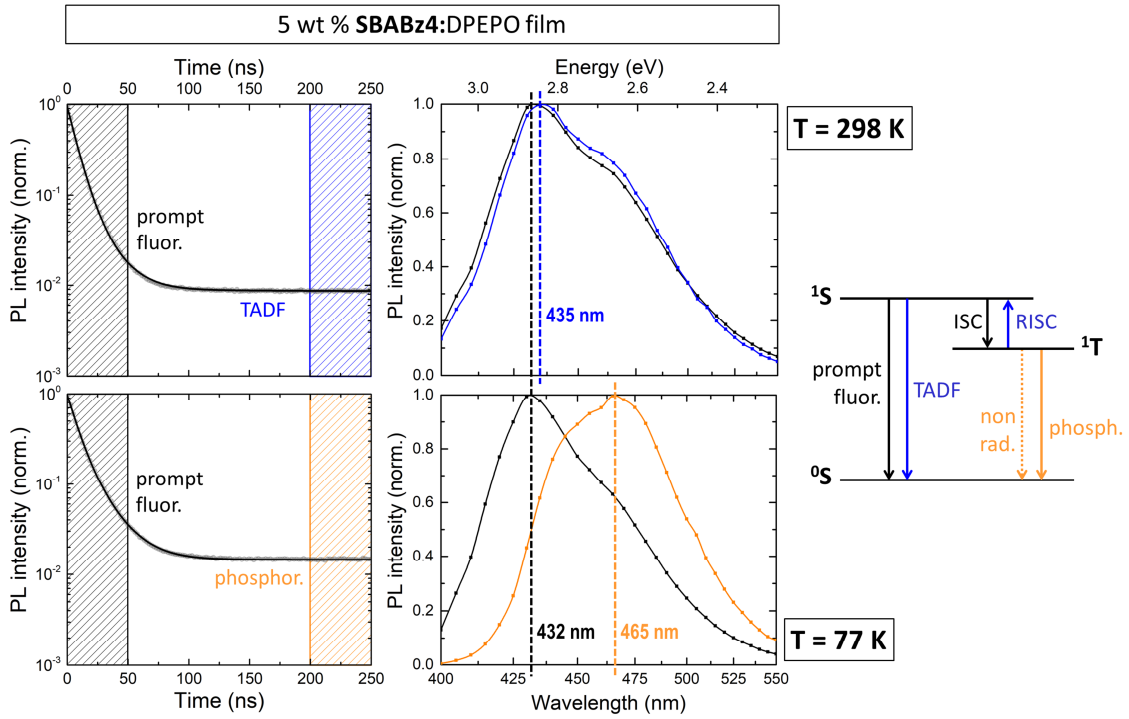

Figure 6.4. PL decay curves and the corresponding normalized PL spectra at different stages of decay in 5 wt % SBABz4:DPEPO film at 298 K (upper plots) and 77 K (lower plots). Prompt components (black curves) were integrated within 0–50 ns, delayed (blue) and phosphorescence (orange) within 200–250 ns. Right: proposed energy diagram of the respective processes.

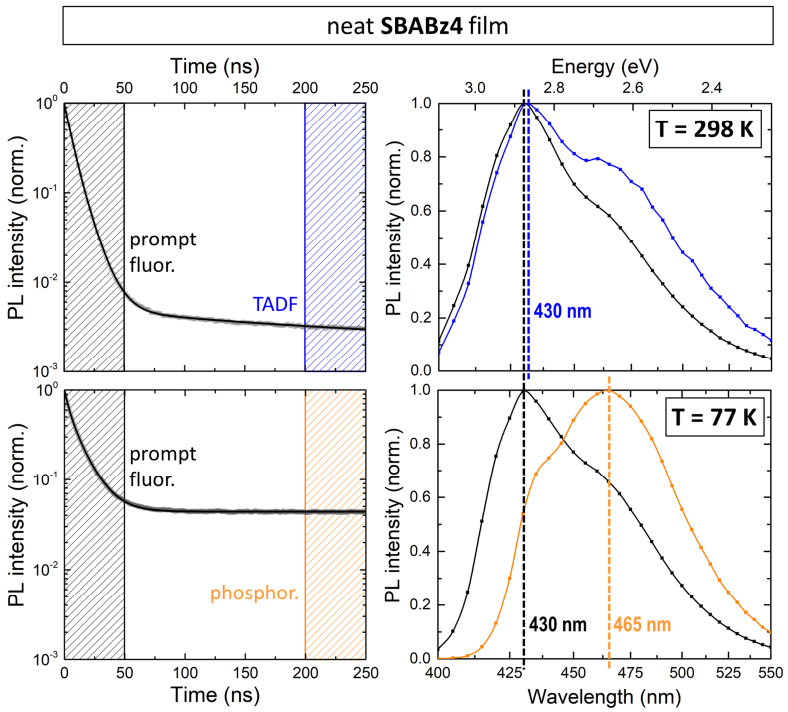

Figure 6.5. PL decay curves and the corresponding normalized PL spectra at different stages of decay in neat SBABz4 film at 298 K (upper plots) and 77 K (lower plots). Prompt components (black curves) were integrated within 0–50 ns, delayed (blue) and phosphorescence (orange) within 200–250 ns.

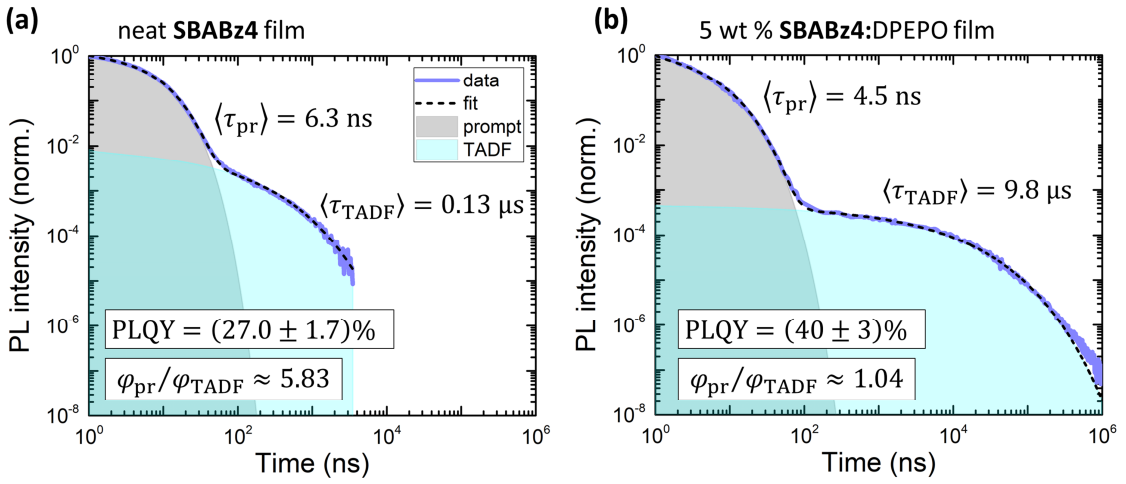

Figure 6.6. PL decay curves of the neat SBABz4 (a) and 5 wt % SBABz4:DPEPO (b) films detected at 435 nm at room temperature. Fit (dashed) is the sum of two stretched decaying exponents.

Figure 6.6 demonstrates PL decay curves of the neat SBABz4 film and 5 wt % SBABz4:DPEPO film recorded in a wide dynamic range at room temperature. Transient PL in both films clearly shows two distinctive components: prompt fluorescence and TADF. Both components deviate from the purely exponential decay behavior observed previously in the dilute solution (**Figure 6.3c**). We found out that a stretched exponent provided an excellent fit for both prompt and delayed components. Hence, the normalized decay curves were fitted with a sum of two stretched exponents:

$$\mathrm{PL}_{\mathrm{norm}}(t) = A_{\mathrm{pr}} \exp\left(-\left(\frac{t}{\tau_{\mathrm{pr}}}\right)^{\beta_{\mathrm{pr}}}\right) + A_{\mathrm{TADF}} \exp\left(-\left(\frac{t}{\tau_{\mathrm{TADF}}}\right)^{\beta_{\mathrm{TADF}}}\right) \tag{6.7}$$

Then, the statistical averages for decay times write:

$$\langle\tau_{\mathrm{pr}}\rangle = \int_0^{\infty} \exp\left(-\left(\frac{t}{\tau_{\mathrm{pr}}}\right)^{\beta_1}\right) dt = \tau_{\mathrm{pr}} \cdot \frac{1}{\beta_{pr}} \Gamma\left(\frac{1}{\beta_{pr}}\right) \tag{6.8}$$

$$\langle\tau_{\mathrm{TADF}}\rangle = \int_0^{\infty} \exp\left(-\left(\frac{t}{\tau_{\mathrm{TADF}}}\right)^{\beta_2}\right) dt = \tau_{\mathrm{TADF}} \cdot \frac{1}{\beta_{TADF}} \Gamma\left(\frac{1}{\beta_{TADF}}\right) \tag{6.9}$$

Here $\Gamma(x)$ is Gamma–function. The characteristic lifetimes given by **Eq. 6.8** and **6.9** are not directly comparable to the lifetimes of single-exponential PL decay in the solution; therefore, we denoted them with angle brackets: $\langle\tau_{\mathrm{pr}}\rangle$ and $\langle\tau_{\mathrm{TADF}}\rangle$.

Notably, delayed fluorescence in the neat film decays 2 orders of magnitude faster than in the host matrix (0.13 and 9.8 µs, respectively). We assign the increased decay rate in the neat SBABz4 film to molecular aggregation with subsequent increase of nonradiative decay rate. For the same reason, PLQY of the doped matrix is higher than this of the neat film (40% and 27%, respectively; **Figure 6.6** and **Table 6.1**).

Parameter	neat SBABz4 film		5 wt % SBABz4:DPEPO film	
	prompt	TADF	prompt	TADF
A, a.u.	1.01	0.0085	1.02	0.00046
τ, ns	5.8	46	3.45	2750
β	0.85	0.42	0.67	0.39
$\langle\tau\rangle$, ns	6.3	134.4	4.6	9815
S, a.u.	6.47	1.11	4.71	4.51
$\varphi_{pr}/\varphi_{TADF}$	5.83		1.04	

Table 6.2. Fit parameters for the normalized PL decay curves of SBABz4 thin films.

The ratio between quantum efficiencies of the prompt and delayed components, $\varphi_{pr}/\varphi_{TADF}$, was calculated as the ratio of the areas under the corresponding stretched exponents, S_{pr}/S_{TADF} (**Table 6.2**). Remarkably, prompt fluorescence in the neat film outperforms TADF ($\varphi_{pr}/\varphi_{TADF} \approx 5.83$), whereas both components equally contribute to the emission of the doped matrix ($\varphi_{pr}/\varphi_{TADF} \approx 1.04$).

Now, using the measured values for PLQY, one can extract absolute quantum efficiencies of the involved processes for thin films (**Figure 6.7**). TADF efficiency increases dramatically in the doped matrix ($\varphi_{TADF} \approx 0.196$) in comparison to the neat film ($\varphi_{TADF} \approx 0.040$). All in all, isolating and immobilizing the emitter molecules in the host matrix significantly improve TADF lifetime and efficiency, which is essential for OLED performance.

We applied **Eq. 6.6** in order to obtain performance estimates for SBABz4-based OLEDs from photophysical constants of thin films (**Table 6.3**). Resulting maximum internal EL efficiency of 5 wt % SBABz4:DPEPO film exceeds that of the neat film more than twice (0.237 and 0.095, respectively).

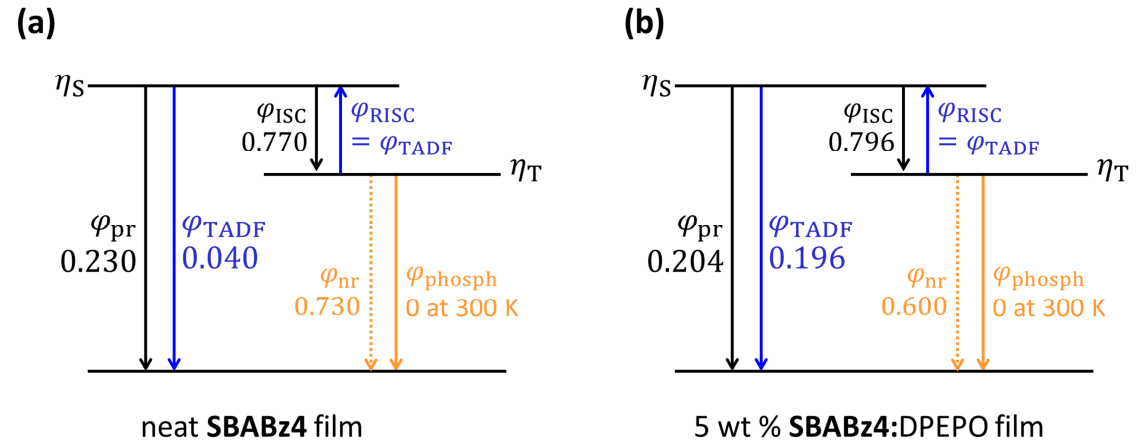

Figure 6.7. Energy diagram depicting quantum efficiencies of various processes in the neat SBABz4 (a) and 5 wt % SBABz4:DPEPO (b) films.

Parameter	neat SBABz4 film	5 wt % SBABz4:DPEPO film
$\Phi_{EL,int}$	0.095	**0.237**
$EQE_{max,20\%}$[a]	1.9%	**4.7%**
$EQE_{max,30\%}$[b]	2.9%	**7.1%**

[a] EQE of corresponding OLED estimated for 20% light outcoupling.
[b] EQE of corresponding OLED estimated for 30% light outcoupling.

Table 6.3. Maximum external electroluminescence efficiencies and external quantum efficiencies estimated from photophysical parameters for SBABz4-based $OLED_S$.

We applied **Eq. 6.6** in order to obtain performance estimates for SBABz4-based OLEDs from photophysical constants of thin films (**Table 6.3**). Resulting maximum internal EL efficiency of 5 wt % SBABz4:DPEPO film exceeds that of the neat film more than twice (0.237 and 0.095, respectively).

The estimated EQE for the OLED based on the doped matrix ($\mathrm{EQE_{max}} = 7.1\%$) is in excellent agreement with the corresponding experimental value ($\mathrm{EQE_{max}} = 6.8\%$; see **Figure 6.8**), as long as the light outcoupling of 30% is assumed (**Table 6.3**). Therefore, we propose that the light outcoupling of SBABz4-based OLEDs exceeds conventional 20%, as it was shown earlier for other stick-like emitters.[5,6,28]

The preliminary measurements performed in the group of Prof. Wolfgang Brütting revealed the degree of horizontal orientation of 80% (molecules mostly lie flat), which is somewhat below the best values reported for other TADF systems, but well above the isotropic orientation. However, self-orientation of the SBABz4 emitter lies outside the scope of this work; and the problem needs to be elucidated in future studies.

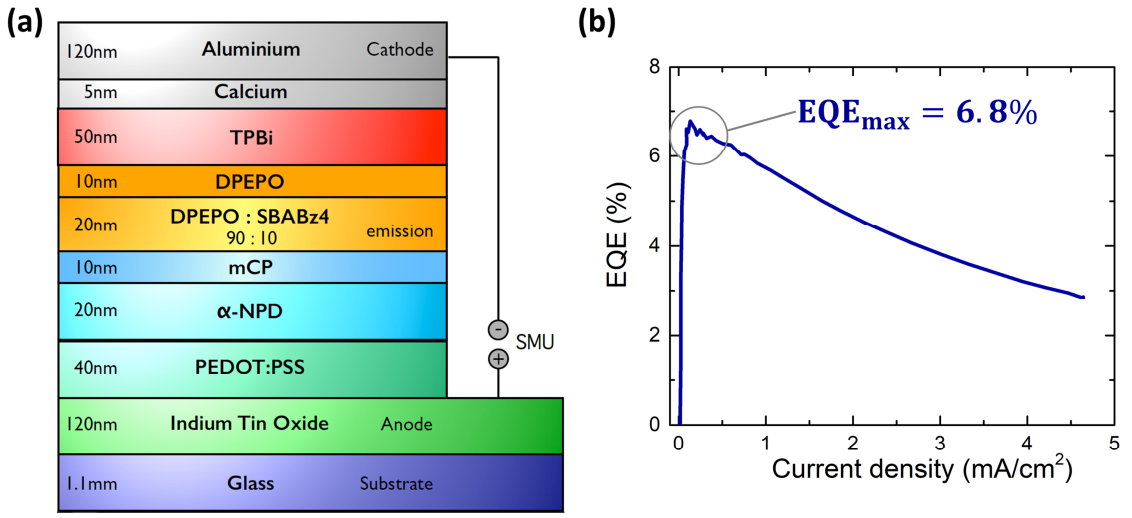

Figure 6.8. (a) OLED layout. Emitting 10 wt % SBABz4:DPEPO layer was co-evaporated. (b) EQE of the SBABz4-based OLED operating at 5 V.

6.2.4. Singlet–Triplet Energy Gap from TRPL

Temperature-dependent TRPL in combination with absolute PLQY measurements allows calculation of the energy splitting ΔE_{ST} for the singlet and triplet levels involved in TADF process.[29]

Let us consider three-level system with ISC and RISC between the excited singlet and triplet levels. **Figure 6.9** shows the corresponding rate constants, where k denotes radiative and intersystem processes, q nonradiative. Densities of singlet and triplet excitons are shown with n and m, respectively.

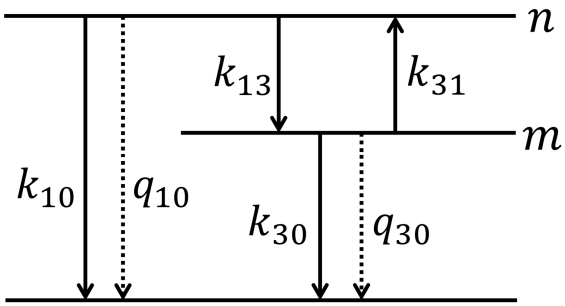

Figure 6.9. Energy diagram for three-level system with RISC process (k_{31}). Rates of radiative and intersystem transitions are denoted with k, nonradiative with q.

Rate equations for this TADF system are

$$\frac{dn}{dt} = -(k_{10} + q_{10} + k_{13})n + k_{31}m, \tag{6.10}$$

$$\frac{dm}{dt} = k_{13}n - (k_{30} + q_{30} + k_{31})m. \tag{6.11}$$

Initial conditions at optical excitation:

$$n(0) = n_0, \tag{6.12}$$

$$m(0) = 0. \tag{6.13}$$

Let us denote:

$$\begin{pmatrix} a & b \\ c & d \end{pmatrix} \equiv \begin{pmatrix} k_{10} + q_{10} + k_{13} & k_{31} \\ k_{13} & k_{30} + q_{30} + k_{31} \end{pmatrix} \tag{6.14}$$

Then, the characteristic equation for the system of **Eq. 6.10–6.11** will write:

$$\lambda_{1,2} = \frac{1}{2}\left(a + d \pm \sqrt{(a+d)^2 - 4(ad - bc)}\right) = \frac{1}{2}(a + d \pm \xi) \tag{6.15}$$

where

$$\xi \equiv \sqrt{(a+d)^2 - 4(ad - bc)} \tag{6.16}$$

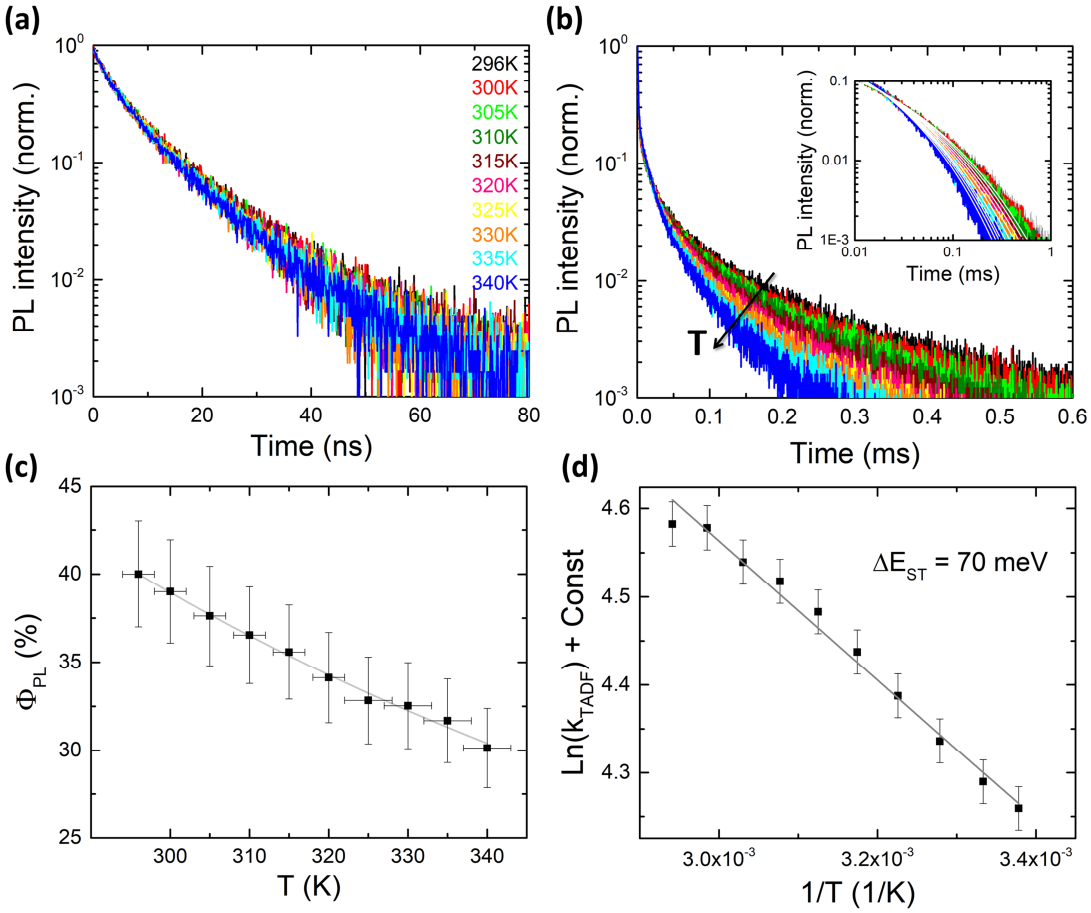

Figure 6.10. TRPL from 5 wt % SBABz4:DPEPO film above the room temperature. (a) Prompt fluorescence. (b) Delayed fluorescence. The inset shows stretched exponential fit (white lines) on double logarithmic scale. (c) Absolute PLQY measured at growing temperature in the inert atmosphere. (d) Arrhenius-like plot for k_{TADF}.

Exact solutions of the **Eq. 6.10–6.11** are

$$n(t) = n_0 \frac{1}{\xi}\left((\lambda_1 - d)\mathrm{e}^{-\lambda_1 t} + (d - \lambda_2)\mathrm{e}^{-\lambda_2 t}\right) \tag{6.17}$$

$$m(t) = n_0 \frac{c}{\xi}\left(\mathrm{e}^{-\lambda_1 t} - \mathrm{e}^{-\lambda_2 t}\right) \tag{6.18}$$

Rate of photon emission $d\nu_{\mathrm{em}}/dt$ from the singlet level (includes both prompt fluorescence and TADF) is

$$\frac{d\nu_{\mathrm{em}}}{dt} = k_{10} n(t) \tag{6.19}$$

External PLQY is defined as ratio between the number of emitted photons and the number of absorbed photons. If the radiative decay from triplet (k_{30}, phosphorescence) is negligible, then the total PLQY in such system is

$$\mathrm{PLQY} = \frac{\nu_{\mathrm{em}}}{\nu_{\mathrm{abs}}} = \frac{\nu_{\mathrm{em}}}{n_0} \tag{6.20}$$

Here we assume that every absorbed photon creates an exciton ($\nu_{\mathrm{abs}} = n_0$).

In light of the solution derived above for the singlet exciton density $n(t)$, the number of emitted photons will write:

$$\nu_{\mathrm{em}} = \int_0^\infty \frac{d\nu_{\mathrm{em}}}{dt} dt = \int_0^\infty k_{10} n(t) dt = n_0 \frac{k_{10}}{\xi}\left(\frac{\lambda_1 - d}{\lambda_1} + \frac{d - \lambda_2}{\lambda_2}\right) \tag{6.21}$$

Then the exact expression for PLQY is

$$\mathrm{PLQY} = \frac{k_{10}}{\xi}\left(\frac{\lambda_1 - d}{\lambda_1} + \frac{d - \lambda_2}{\lambda_2}\right) \tag{6.22}$$

where the prompt and delayed components are

$$\varphi_{\mathrm{pr}} = \frac{k_{10}}{\xi} \cdot \frac{\lambda_1 - d}{\lambda_1} \tag{6.23}$$

$$\varphi_{\mathrm{TADF}} = \frac{k_{10}}{\xi} \cdot \frac{d - \lambda_2}{\lambda_2} \tag{6.24}$$

Now, we can make several approximations following from physical properties of our TADF system in order to simplify the solution and make it applicable for experimental results. Hereafter we assume

- $q_{10} = 0$ (only radiative decay from singlet, since the prompt PL component is temperature-independent; **Figure 6.10a**);
- $k_{30} = 0$ (phosphorescence was not observed at room temperature);
- $k_{10} \sim k_{13}$ (rate of radiative decay from the singlet is in the order of ISC rate, since the triplet is effectively populated);
- $k_{31} \sim k_{30}$ (rate of RISC is in the order of triplet nonradiative rate, since both processes are observed);
- $k_{10} \gg k_{31}$ (rate of singlet radiative decay significantly exceeds RISC, since the observed prompt decay is much faster than TADF).

The accepted approximations will lead to

$$\begin{pmatrix} a & b \\ c & d \end{pmatrix} \approx \begin{pmatrix} k_{10} + k_{13} & k_{31} \\ k_{13} & q_{30} + k_{31} \end{pmatrix} \tag{6.25}$$

where $a \sim c$; $b \sim d$; $a, c \gg b, d$.

Therefore

$$\lambda_1 \approx \xi \approx a, \ \lambda_2 \approx d - \frac{bc}{a}, \ \mathrm{PLQY} \approx \frac{k_{10}}{a}\left(1 + \frac{bc}{a} \cdot \frac{1}{\lambda_2}\right). \tag{6.26}$$

Then the measurables will be expressed via characteristic rates:

$$\lambda_1 \approx k_{10} + k_{13} \tag{6.27}$$

$$\lambda_2 \approx q_{30} + k_{31}\left(1 - \frac{k_{13}}{k_{10} + k_{13}}\right) \tag{6.28}$$

$$\mathrm{PLQY} \approx \frac{k_{10}}{k_{10} + k_{13}}\left(1 + \frac{k_{13}k_{31}}{k_{10} + k_{13}}\left(q_{30} + k_{31}\left(1 - \frac{k_{13}}{k_{10} + k_{13}}\right)\right)^{-1}\right) \tag{6.29}$$

In such TADF system, only the rates $k_{31}$and q_{30} are temperature-dependent; namely, both rates grow with temperature. According to **Eq. 6.29**, PLQY grows with RISC rate (k_{31}) and decreases with increase of nonradiative losses (q_{30}). Such correlation could have been predicted on intuitive grounds. More importantly, **Eq. 6.29** also shows that the PLQY is much more sensitive to q_{30}, than to k_{31}. Therefore, the measured PLQY can drop with temperature, even though RISC is getting more efficient.

The previously stated assumptions will also lead to the following ratio between prompt and delayed components

$$\frac{\varphi_{\mathrm{pr}}}{\varphi_{\mathrm{TADF}}} \approx \frac{\lambda_1\lambda_2}{k_{13}k_{31}} \tag{6.30}$$

Then the rate of RISC will write:

$$k_{\mathrm{RISC}} \equiv k_{31} \approx \frac{\lambda_1\lambda_2}{k_{13}} \cdot \frac{\varphi_{\mathrm{TADF}}}{\varphi_{\mathrm{pr}}} \tag{6.31}$$

$$\ln(k_{\mathrm{RISC}}) \approx \ln\left(\frac{\lambda_1\lambda_2}{k_{13}} \cdot \frac{\varphi_{\mathrm{TADF}}}{\varphi_{\mathrm{pr}}}\right) = \ln(\lambda_2\varphi_{\mathrm{TADF}}) + \ln\left(\frac{\lambda_1}{k_{13}} \cdot \frac{1}{\varphi_{\mathrm{pr}}}\right) \tag{6.32}$$

Here only the $\ln(\lambda_2\varphi_{\mathrm{TADF}})$ depends on temperature, while the $\ln(\lambda_1/k_{13}\varphi_{\mathrm{pr}})$ is temperature-independent. Therefore, one can write

$$\ln(k_{\mathrm{RISC}}) \approx \ln(\lambda_2\varphi_{\mathrm{TADF}}) + \mathrm{const} \tag{6.33}$$

At the same time,

$$k_{\mathrm{RISC}} \propto \exp\left(\frac{\Delta E_{\mathrm{ST}}}{k_{\mathrm{B}}T}\right) \tag{6.34}$$

$$\Rightarrow \ln(k_{\mathrm{RISC}}) = \frac{\Delta E_{\mathrm{ST}}}{k_{\mathrm{B}}} \cdot \frac{1}{T} + \mathrm{const} \tag{6.35}$$

Therefore

$$\ln(\lambda_2\varphi_{\mathrm{TADF}}) = \frac{\Delta E_{\mathrm{ST}}}{k_{\mathrm{B}}} \cdot \frac{1}{T} + \mathrm{const} \tag{6.36}$$

Now ΔE_{ST} can be expressed via measurables (λ_2, φ_{TADF}, and T) and Boltzmann constant (see **Figure 6.10**).

We obtained $\Delta E_{\mathrm{ST}} \approx 70$ meV for 5 wt % SBABz4:DPEPO film. This energy difference

is sufficiently low ($\Delta E_{ST} \sim k_B T$) to provide experimentally observed efficient TADF. ΔE_{ST} can be further decreased via judicious variation of acceptor units. On the other hand, stronger acceptors were shown to cause red shift of emission in similar systems,[5] whereas the emission from SBABz4 is deep blue.

6.3. Conclusion

Here, we addressed photophysics of a novel compact deep blue OLED emitter, SBABz4, containing spiro-biacridine and benzonitrile units, and its monomer counterpart DMABz4. We showed that the spiro-linkage in the double-donor core of SBABz4 renders its luminescence pure blue relative to the single-donor DMABz4 while preserving efficient TADF. Therefore, core-donor provides desirable for applications color tuning in the deep blue region, as opposed to the commonly used TADF molecular design with core-acceptor. The SBABz4 emitter combines prompt fluorescence, phosphorescence at low temperature, and TADF at room temperature. The last was independently proven by oxygen-quenching of the delayed PL component and temperature-dependent TRPL measurements. We estimated $\mathrm{EQE_{max}} = 7.1\%$ in SBABz4-based OLEDs from the PL lifetimes and efficiencies and obtained $\mathrm{EQE_{max}} = 6.8\%$ in an operating test device. Transient PL was recorded from the solutions and solid films in the broad dynamic range covering up to 8 orders of magnitude in intensity and 6 orders of magnitude in time. The stretched exponent is shown to fit the transient PL in the films very well, whereas PL decay in dilute solution is found to be purely exponential. Immobilization and isolation of the emitter molecules in the DPEPO host matrix maintain the efficient TADF. Finally, we show that SBABz4 emitter doped in the host matrix demonstrates superior photophysical properties over the neat film.

6.4. Materials and Methods

6.4.1. Solution Preparation

Deoxygenated solutions of SBABz4 and DMABz4 in dichloromethane (DCM) with concentration 10^{-5} mol L^{-1} were prepared in a glove box under nitrogen atmosphere.

Deoxygenated solutions of SBABz4 for UV–vis absorption and luminescence measurements in different solvents were obtained by bubbling nitrogen and sealing with a J. Young valve. Spectroscopic grade solvents were used without further purification.

6.4.2. Film Preparation

Films for optical measurements were prepared in a glove box with nitrogen atmosphere. Neat SBABz4 and SBABz4:DPEPO films were processed on a 0.5 x 0.5 in. glass substrates without modification. The substrates were sequentially cleaned with deionized water, acetone, and isopropanol for 10 min each in an ultrasonic bath and plasma-etched for 30 s before use. Solutions of SBABz4 (or SBABz4:DPEPO with the desired weight ratio) in DCM with concentration 5 mg mL^{-1} were spin-coated at 3000 rpm during 1 min. After spin-coating, the substrates were annealed on a hot plate at 100°C for 10 min.

6.4.3. PL Measurements

PL spectra and transients of solutions and films were recorded with calibrated fluorescence spectrometer FLS980 (Edinburgh Instruments), equipped with three excitation sources: continuous broad-

spectrum xenon lamp Xe1, pulsed violet diode laser EPL-375 (wavelength 375.0 nm, pulse width 80 ps), and microsecond xenon flash lamp µF920. Laser repetition rate was tunable with discrete steps in the range from 2.5 kHz to 20 MHz. Spectral resolution of the system was 0.1 nm. Temporal resolution for time-resolved measurements varied from 2 to 50 ns, depending on the recorded time range. Emission recorded at different time scales was merged to improve temporal resolution for the prompt component. All measurements for solid films at room and low temperatures were carried out in active vacuum (10^{-5} mbar) in Janis ST-100 cryostat. Measurements at room temperature were performed beforehand for every sample. PLQYs were measured with the calibrated integrating sphere F-M01 in FLS980 spectrometer. All measurements for solutions were conducted in a standard (10 x 10 mm) quartz cuvette with a tight screw cap. Solid films for PLQY measurements were sealed in a quartz cuvette under nitrogen atmosphere.

6.5. References

(1) Endo, A.; Sato, K.; Yoshimura, K.; Kai, T.; Kawada, A.; Miyazaki, H.; Adachi, C. Efficient Up-Conversion of Triplet Excitons into a Singlet State and Its Application for Organic Light Emitting Diodes. *Appl. Phys. Lett.* **2011**, *98*, 2009–2012.

(2) Uoyama, H.; Goushi, K.; Shizu, K.; Nomura, H.; Adachi, C. Highly Efficient Organic Light-Emitting Diodes from Delayed Fluorescence. *Nature* **2012**, *492*, 234–238.

(3) Kaji, H.; Suzuki, H.; Fukushima, T.; Shizu, K.; Suzuki, K.; Kubo, S.; Komino, T.; Oiwa, H.; Suzuki, F.; Wakamiya, A.; et al. Purely Organic Electroluminescent Material Realizing 100% Conversion from Electricity to Light. *Nat. Commun.* **2015**, *6*, 1–8.

(4) Zhang, Q.; Tsang, D.; Kuwabara, H.; Hatae, Y.; Li, B.; Takahashi, T.; Lee, S. Y.; Yasuda, T.; Adachi, C. Nearly 100% Internal Quantum Efficiency in Undoped Electroluminescent Devices Employing Pure Organic Emitters. *Adv. Mater.* **2015**, *27*, 2096–2100.

(5) Liu, M.; Komatsu, R.; Cai, X.; Hotta, K.; Sato, S.; Liu, K.; Chen, D.; Kato, Y.; Sasabe, H.; Ohisa, S.; et al. Horizontally Orientated Sticklike Emitters: Enhancement of Intrinsic Out-Coupling Factor and Electroluminescence Performance. *Chem. Mater.* **2017**, *29*, 8630–8636.

(6) Lin, T.-A.; Chatterjee, T.; Tsai, W.-L.; Lee, W.-K.; Wu, M.-J.; Jiao, M.; Pan, K.-C.; Yi, C.-L.; Chung, C.-L.; Wong, K.-T.; et al. Sky-Blue Organic Light Emitting Diode with 37% External Quantum Efficiency Using Thermally Activated Delayed Fluorescence from Spiroacridine-Triazine Hybrid. *Adv. Mater.* **2016**, *28*, 6976–6983.

(7) Rajamalli, P.; Senthilkumar, N.; Huang, P. Y.; Ren-Wu, C. C.; Lin, H. W.; Cheng, C. H. New Molecular Design Concurrently Providing Superior Pure Blue, Thermally Activated Delayed Fluorescence and Optical Out-Coupling Efficiencies. *J. Am. Chem. Soc.* **2017**, *139*, 10948–10951.

(8) Byeon, S. Y.; Kim, J.; Lee, D. R.; Han, S. H.; Forrest, S. R.; Lee, J. Y. Nearly 100% Horizontal Dipole Orientation and Upconversion Efficiency in Blue Thermally Activated Delayed Fluorescent Emitters. *Adv. Opt. Mater.* **2018**, *1701340*, 1701340.

(9) Kondakov, D. Y. Characterization of Triplet-Triplet Annihilation in Organic Light-Emitting Diodes Based on Anthracene Derivatives. *J. Appl. Phys.* **2007**, *102*, 114504.

(10) Hu, J. Y.; Pu, Y. J.; Satoh, F.; Kawata, S.; Katagiri, H.; Sasabe, H.; Kido, J. Bisanthracene-Based Donor-Acceptor-Type Light-Emitting Dopants: Highly Efficient Deep-Blue Emission in Organic Light-Emitting Devices. *Adv. Funct. Mater.* **2014**, *24*, 2064–2071.

(11) Baldo, M. A.; O'Brien, D. F.; You, Y.; Shoustikov, A.; Sibley, S.; Thompson, M. E.; Forrest, S. R. Highly Efficient Phosphorescent Emission from Organic Electroluminescent Devices. *Nature* **1998**, *395*, 151–154.

(12) Ma, Y.; Zhang, H.; Shen, J.; Che, C. Electroluminescence from Triplet Metal—Ligand Charge-Transfer Excited State of Transition Metal Complexes. *Synth. Met.* **1998**, *94*, 245–248.

(13) Adachi, C.; Baldo, M. A.; Thompson, M. E.; Forrest, S. R. Nearly 100% Internal Phosphorescence Efficiency in an Organic Light Emitting Device. *J. Appl. Phys.* **2001**, *90*, 5048–5051.

(14) Köhler, A.; Wilson, J. S.; Friend, R. H. Fluorescence and Phosphorescence in Organic Materials. *Adv. Mater.* **2002**, *14*, 701–707.

(15) Beljonne, D.; Shuai, Z.; Pourtois, G.; Bredas, J. L. Spin-Orbit Coupling and Intersystem Crossing in Conjugated Polymers: A Configuration Interaction Description. *J. Phys. Chem. A* **2001**, *105*, 3899–3907.

(16) Numata, M.; Yasuda, T.; Adachi, C. High Efficiency Pure Blue Thermally Activated Delayed Fluorescence Molecules Having 10*H*-Phenoxaborin and Acridan Units. *Chem. Commun.* **2015**, *51*, 9443–9446.

(17) Dos Santos, P. L.; Ward, J. S.; Bryce, M. R.; Monkman, A. P. Using Guest-Host Interactions to Optimize the Efficiency of TADF OLEDs. *J. Phys. Chem. Lett.* **2016**, *7*, 3341–3346.

(18) Chan, C.-Y.; Cui, L.-S.; Kim, J. U.; Nakanotani, H.; Adachi, C. Rational Molecular Design for Deep-Blue Thermally Activated Delayed Fluorescence Emitters. *Adv. Funct. Mater.* **2018**, 1706023.

(19) Cho, Y. J.; Jeon, S. K.; Chin, B. D.; Yu, E.; Lee, J. Y. The Design of Dual Emitting Cores for Green Thermally Activated Delayed Fluorescent Materials. *Angew. Chem., Int. Ed.* **2015**, *54*, 5201–5204.

(20) Kim, M.; Jeon, S. K.; Hwang, S. H.; Lee, S. S.; Yu, E.; Lee, J. Y. Correlation of Molecular Structure with Photophysical Properties and Device Performances of Thermally Activated Delayed Fluorescent Emitters. *J. Phys. Chem. C* **2016**, *120*, 2485–2493.

(21) Han, C.; Zhao, Y.; Xu, H.; Chen, J.; Deng, Z.; Ma, D.; Li, Q.; Yan, P. A Simple Phosphine-Oxide Host with a Multi-Insulating Structure: High Triplet Energy Level for Efficient Blue Electrophosphorescence. *Chem. Eur. J.* **2011**, *17*, 5800–5803.

(22) Zhang, Q.; Li, B.; Huang, S.; Nomura, H.; Tanaka, H.; Adachi, C. Efficient Blue Organic Light-Emitting Diodes Employing Thermally Activated Delayed Fluorescence. *Nat. Photonics* **2014**, *8*, 326–332.

(23) Noda, H.; Kabe, R.; Adachi, C. Blue Thermally Activated Delayed Fluorescence Molecule Having Acridane and Cyanobenzene Units. *Chem. Lett.* **2016**, *45*, 1463–1466.

(24) Ghoneim, N.; Suppan, P. Solvation of TICT* States in Solvent Mixtures. *Pure Appl. Chem* **1993**, *65*, 1739–1743.

(25) Grabowski, Z. R.; Rotkiewicz, K.; Rettig, W. Structural Changes Accompanying Intramolecular Electron Transfer: Focus on Twisted Intramolecular Charge-Transfer States and Structures. *Chem. Rev.* **2003**, *103*, 3899–4031.

(26) Marini, A.; Muñoz-Losa, A.; Biancardi, A.; Mennucci, B. What Is Solvatochromism? *J. Phys. Chem. B* **2010**, *114*, 17128–17135.

(27) Ryoo, C. H.; Cho, I.; Han, J.; Yang, J. H.; Kwon, J. E.; Kim, S.; Jeong, H.; Lee, C.; Park, S. Y. Structure-Property Correlation in Luminescent Indolo[3,2-*b*]Indole (IDID) Derivatives: Unraveling the Mechanism of High Efficiency Thermally Activated Delayed Fluorescence (TADF). *ACS Appl. Mater. Interfaces* **2017**, *9*, 41413–41420.

(28) Mayr, C.; Lee, S. Y.; Schmidt, T. D.; Yasuda, T.; Adachi, C.; Brütting, W. Efficiency Enhancement of Organic Light-Emitting Diodes Incorporating a Highly Oriented Thermally Activated Delayed Fluorescence Emitter. *Adv. Funct. Mater.* **2014**, *24*, 5232–5239.

(29) Goushi, K.; Yoshida, K.; Sato, K.; Adachi, C. Organic Light-Emitting Diodes Employing Efficient Reverse Intersystem Crossing for Triplet-to-Singlet State Conversion. *Nat. Photonics* **2012**, *6*, 253–258.

Chapter 7

Summary

In this work, we elucidated recombination kinetics in organic and hybrid semiconductors by steady-state and time-resolved PL spectroscopy. Using these simple and very flexible experimental techniques, we probed the infrared emission from recombining free charge carriers in metal–halide perovskites, as well as the deep blue luminescence from intramolecular charge-transfer states in novel OLED emitters. We showed that similar state diagrams and kinetic models accurately describe the dynamics of excited species in these very different material systems.

In **Chapters 4** and **5**, we focused on lead iodide perovskites (MAPI and FAPI), whose comparatively developed deposition techniques suited the systematic material research. In MAPI, we harnessed the anomalous dependence of transient PL on the laser repetition rate in order to investigate the role of interfaces with the commonly used charge-selective layers: $PC_{60}BM$, spiro-MeOTAD, and P3HT. The film was deposited on a large precut substrate and separated into several parts, which were then covered with the charge-selective layers. Thereby, the same bulk perovskite structure was maintained for all samples. Consequently, we were able to isolate interface-affected and bulk carrier recombination. The first one dominated the fast component of PL decay up to 300 ns, whereas the last was assigned to the remaining slow component. The laser repetition rate significantly prolonged PL decay in MAPI with additional interfaces while shortening the charge carrier lifetime in the pristine film. We qualitatively explained this effect by a kinetic model that included radiative electron–hole recombination and nonradiative trap-assisted recombination. All in all, we showed that the apparent PL lifetime in MAPI is to large extend defined by the laser repetition rate and by the adjacent interfaces.

Further, we studied photon recycling in MAPI and FAPI. We monitored how the microscopic PL transforms while propagating through the thin perovskite film. The emission was recorded within 5 orders of magnitude in intensity up to 70 µm away from the excitation spot. The Beer–Lambert law previously failed to describe the complex interplay of the intrinsic PL spectrum and the additional red-shifted peak. Therefore, we developed a general numerical model that accounts for self-absorption and diffusion of the secondary charge carriers. A simulation based on this model showed excellent agreement with the experimental spatially resolved PL maps. The proposed model can be applied to any perovskite film, because it uses easily measurable intrinsic PL spectrum and macroscopic absorption coefficient as seeding parameters.

In **Chapter 6**, we conducted an extensive photophysical study of a novel compact deep blue OLED emitter, SBABz4, containing spiro-biacridine and benzonitrile units. We also considered its single-donor monomer counterpart, DMABz4, in order to highlight the structure–property relationships. Both compounds exhibited thermally activated delayed fluorescence (TADF), which was independently proven by oxygen quenching and

temperature-dependent transient PL measurements. The spiro-linkage in the double-donor core of SBABz4 rendered its luminescence pure blue compared to the blue-green emission from the single-donor DMABz4. Thus, the core-donor provided desirable color tuning in the deep blue region, as opposed to the common TADF molecular design with core-acceptor. Using PL lifetimes and efficiencies, we predicted $\mathrm{EQE}_{\max} = 7.1\%$ for SBABz4-based OLED, whereas a real test device showed $\mathrm{EQE}_{\max} = 6.8\%$. Transient PL was recorded from the solutions and solid films in the unprecedentedly broad dynamic range covering up to 6 orders of magnitude in time and 8 orders of magnitude in intensity. The stretched exponent was shown to fit the transient PL in the films very well, whereas PL decay in dilute solution was found purely exponential. When the emitter was embedded in the host matrix that prevented aggregation, its TADF properties were superior in comparison with the pure SBABz4 film. Finally, using temperature-dependent transient PL data, we calculated the TADF activation energy of 70 meV.

To sum up, this Thesis contributes to the two fascinating topics of the last decade's material research: perovskite absorbers for photovoltaics and TADF emitters for OLEDs. We were lucky to work with the emerging systems and tailor for them new models out of the well-known physical concepts. This was both exciting and challenging. In the end, science of novel materials is always a mess. We hope that we brought there a bit of clarity and light.

Zusammenfassung

Im Rahmen dieser Arbeit wurden Rekombinationsmechanismen in organischen und hybriden Halbleitern mittels statischer und zeitaufgelöster Photolumineszenz-Spektroskopie untersucht. Diese einfachen und flexiblen experimentellen Methoden erlaubten es, sowohl die infrarote Emission rekombinierender freier Ladungsträger in Perowskiten als auch die blaue Lumineszenz intramolekularer Ladungstransferzustände in neuartigen OLED-Emittern zu erforschen. Es wurde gezeigt, dass das Verhalten angeregter Ladungsträger in sehr unterschiedlichen Materialsystemen durch vergleichbare Zustandsdiagramme und kinetische Modelle beschrieben werden kann.

Kapitel 4 und **5** legen den Fokus auf Bleiiodid-Perowskite (MAPI und FAPI), deren vergleichsweise etablierte Herstellungsmethode systematische Untersuchungen erlaubt. In MAPI wurde die anomale Abhängigkeit transienter PL von der Repetitionsrate des Lasers verwendet, um die Bedeutung der Grenzflächen zwischen Perowskitschicht und den gängigsten ladungsselektiven Schichten $PC_{60}BM$, spiro-MeOTAD und P3HT zu untersuchen. Dafür wurde die Perowskitschicht auf ein Substrat aufgebracht, dieses in mehrere gleiche Stücke geteilt und anschließend mit einer jeweils unterschiedlichen ladungsselektiven Schicht bedeckt. Dies sicherte die Vergleichbarkeit der aktiven Schicht der verschiedenen Proben. Durch diesen Ansatz konnten der Einfluss des aktiven Materials als auch der seiner Grenzflächen auf die Ladungsträgerrekombination getrennt beobachtet werden. Ersterer dominierte den schnellen Anteil des PL-Abfalls, letzterer den langsamen Anteil. Die Repetitionsrate des Lasers verlangsamte den PL-Abfall in MAPI-Filmen mit zusätzlichen Grenzflächen signifikant, während sie die Lebensdauer der Ladungsträger in reinen MAPI-Filmen verkürzte. Dieser Effekt konnte durch ein qualitatives Modell erklärt werden, welches strahlende Elektron–Loch-Rekombination sowie nichtstrahlende Rekombination über Ladungsträgerfallen miteinbezieht. Insgesamt konnte gezeigt werden, dass die PL-Lebensdauer in MAPI stark von der Laserrepetitionsrate sowie von Grenzflächeneffekten abhängig ist.

Des Weiteren wurde der Photon-Recycling-Effekt in MAPI und FAPI untersucht. Dafür wurde verfolgt, wie sich die lokale PL mit ihrer Ausbreitung durch den dünnen Perowskitfilm verändert. Die Emission konnte bis zu 70 µm entfernt von der Anregung gemessen werden, bei einer Abnahme der Intensität um fünf Größenordnungen. Mit reiner Anwendung des Lambert–Beer'sches Gesetzes konnte das auftretende komplexe Zusammenspiel des ursprünglichen Spektrums mit einer zusätzlichen rotverschobenen Emission nicht erklärt werden. Deshalb wurde ein allgemeines numerisches Modell entwickelt, das sowohl Selbstabsorption als auch die Diffusion sekundärer Ladungsträger berücksichtigt. Entsprechende Simulationen zeigten hervorragende Übereinstimmung mit räumlich aufgelösten experimentellen PL-Messungen. Das Modell kann auf jeden Perwoskitfilm angewendet werden, da die nötigen Parameter auf dem einfach messbaren intrinsischen PL-Spektrum und dem makroskopischen Absorptionskoeffizienten des jeweiligen Films beruhen.

In **Kapitel 6** wird die umfangreiche photophysikalische Untersuchung eines neuartigen kompakten blauen OLED-Emitters, SBABz4, welcher Spiro-Biacridine und Benzonitril-Einheiten enthält, beschrieben. Auch sein Gegenstück DMABz4, als einfacher Donator, wurde betrachtet, um Zusammenhänge zwischen Struktur und Materialeigenschaften hervorzuheben. Beide Verbindungen zeigten thermisch-aktivierte verzögerte Fluoreszenz (TADF), welche unabhängig voneinander sowohl durch Sauerstoff-Fluoreszenzlöschung als auch durch temperaturabhängige transiente PL-Messungen nachgewiesen wurde. Die Spiro-Bindung im Inneren des zweifachen Donators SBABz4 führten zu einer, im Vergleich zur blaugrünen Emission des einfachen Donators DMABz4, reinen blauen Lumineszenz. Im Gegensatz zum Aufbau üblicher TADF-Molekülen mit zentralem Akzeptor, erlaubt in diesem Fall der zentrale Donator also die gewünschte Farbeinstellung im tiefblauen Bereich. Mit Hilfe von PL-Lebensdauern und -Effizienzen wurde eine EQE_{max} von 7.1% für SBABz4-basierte OLEDs abgeschätzt, während ein reales Testexemplar eine EQE_{max} von 6.8% aufzeigte. Transiente PL wurde für Lösungen sowie für feste Filme in einem beispiellos großen, dynamischen Bereich von sechs Größenordnungen in Zeit und acht Größenordnungen in Intensität aufgenommen. Die transiente PL der Filme lässt sich gut durch eine gestreckte Exponentialfunktion anpassen, während der PL-Abfall der Lösung rein exponentiell verläuft. Die Einbettung des Emitters in der Gast-Matrix, die Aggregieren verhinderte, führten zu gegenüber dem reinen SBABz4-Film überlegenen TADF-Eigenschaften. Zuletzt wurde die TADF Aktivierungsenergie von 70 meV unter alleiniger Verwendung der temperaturabhängigen transienten PL berechnet.

Zusammengefasst steuert diese Doktorarbeit einen Beitrag zu zwei der faszinierendsten Themen der Materialforschung des letzten Jahrzehnts bei: Perowskitabsorbern für die Photovoltaik und TADF-Emittern für OLEDs. Diese Arbeit erlaubte es mit aufkommenden Systemen zu arbeiten und neue Modelle aus bekannten physikalischen Konzepten für sie zu entwickeln. Dies war sowohl spannend als auch anspruchsvoll. Letztlich ist Forschung an neuartigen Materialien immer ein großes Durcheinander. Hoffentlich konnte durch diese Arbeit jedoch ein wenig mehr Klarheit geschaffen werden.

I. Publications and Conference Contributions

Publications

2020 Kudriashova, L. G.; Merkel, M. T.; Baianov, V.; Berger, S.; Tvingstedt, K.; Astakhov, G. V.; Baumann, A.; Dyakonov, V. Photon Propagation and Recycling in Perovskite Films by Spatially Resolved Photoluminescence. *In preparation.*

2019 Bunzmann, N.; Weissenseel, S.; Kudriashova, L.; Grüne, J.; Krugmann, B.; Grazulevicius, J. V.; Sperlich, A.; Dyakonov, V. Optically and Electrically Excited Intermediate Electronic States in Donor:Acceptor-Based OLEDs. *Submitted to Materials Horizons.*

2019 Weissenseel, S.; Drigo, N. A.; Kudriashova, L. G.; Schmid, M.; Morgenstern, T.; Lin, K.-H.; Prlj, A.; Corminboeuf, C.; Sperlich, A; Brütting, W.; Nazeeruddin, M. K.; Dyakonov, V. Getting the Right Twist: Influence of Donor–Acceptor Dihedral Angle on Exciton Kinetics and Singlet–Triplet Gap in Deep Blue Thermally Activated Delayed Fluorescence Emitter. *J. Phys. Chem C* **2019***, 123,* 27778–27784

2018 Drigo, N. A.; Kudriashova, L. G.; Weissenseel, S.; Sperlich, A.; Huckaba, A. J.; Nazeeruddin, M. K.; Dyakonov, V. Photophysics of Deep Blue Acridane- and Benzonitrile-Based Emitter Employing Thermally Activated Delayed Fluorescence. *J. Phys. Chem. C* **2018**, *122*, 22796–22801.

2017 Kudriashova, L. G.; Kiermasch, D.; Rieder, P.; Campbell, M.; Tvingstedt, K.; Baumann, A.; Astakhov, G. V.; Dyakonov, V. Impact of Interfaces and Laser Repetition Rate on Photocarrier Dynamics in Lead Halide Perovskites. *J. Phys. Chem. Lett.* **2017**, *8*, 4697–4703.

Conference Contributions

2018, March — The Role of Molecular Environment in Thermally Activated Delayed Fluorescence
Talk at the DPG Spring Meeting (Meeting of German Physical Society)
Berlin, Germany

2018, February – March — Blue Thermally Activated Delayed Fluorescence from Acridane- and Benzonitrile-Based Emitters
Poster at the International Symposium on Molecular Biradicals
Würzburg, Germany

2017, October — Impact of Interfaces and Laser Repetition Rate on Charge Carrier Dynamics in Lead Halide Perovskites
Poster at the 6th SolTech Conference (Solar Technologies Go Hybrid)
München, Germany

2017, March — Carrier Recombination Analysis in Perovskites by Time-Resolved Photoluminescence
Talk at the DPG Spring Meeting (Meeting of German Physical Society)
Dresden, Germany

SEPOMO Wide Network Events

2019, April — Mons, Belgium

2018, December — Oxford, UK

2017, April — Dresden, Germany

2017, November — Angers, France

II. Acknowledgements

My first day in EP6 was also my first day in Germany. This rather spontaneous decision to do PhD and to leap to the foreign culture turned my life upside-down in an amazing way. I thank everyone who made this time so incredibly great.

First of all, I thank my supervisor Professor Vladimir Dyakonov for giving me the opportunity to do my PhD in EP6. Dear Prof. Dyakonov, you accepted my application barely knowing me, without any guarantees. This trust helped me to hold on every time things got difficult. I am infinitely grateful for your support, for the excellent scientific supervision, for teaching me how to write, submit and apply, and for your willingness to perfect my clumsy talks and weak manuscripts over and over again.

Prof. Jens Pflaum and Prof. Jochen Fricke, your clever questions at the meetings and seminars made every talk given there interesting.

Our present and ex-group leaders — Dr. habil. Georgy Astakhov, Dr. Andreas Sperlich, and Dr. Andreas Baumann — are very different, but each is brilliant in his own way. Georgy, you are my role model of a good PI. Your kind, supportive, sympathetic, and incredibly motivating style of supervision helped me to publish my first paper in EP6. I was very lucky to be your student at least for one year. Hex, thank you for taking over the burden of being my PI. I know that I am not an easy person to deal with, and I am amused that you have never lost your temper, not for a single picosecond. Andy, you are an amazing person and you gather amazing people around you. I was very proud to belong to perovskite group, where I always felt welcomed and smart.

I thank our technical assistants, André Thiem-Riebe and Valentin Baianov. Dear André and Valentin, thank you for running our small universe so well, for the unceasingly pumping pumps and lasing lasers. Measurements were pure joy because of your permanent support.

EP6 is blessed with an excellent secretary, Diep Phan. Diep, you are our good angel, who pays attention to every little detail and always has a kind word for everyone in this huge group. With you, even the German bureaucracy is not that scary.

I cannot possibly mention here all people that made my time in Germany unforgettable, but skipping some names would be a crime. Milena Merkel was my darling master student, from whom I learned way more than I could teach her. Milli, you are a very bright person, a really hardworking and diligent scientist, and an amazing friend, whom I could trust with everything. Philipp Rieder and David Kiermasch, without your high-quality perovskite samples this thesis would not exist. David, we started PhD on the same day, and since then I am desperately trying to “be just like David”. You are an outstanding experimentalist, a great tutor, and a very good friend. Philipp, you make everything around you work properly. Thank you for always being there for me, for being fun, smart, problem-solving, honest, professional, and simply adorable. My dearest long-term officemates, Michael Auth and Nikolai Bunzmann, thanks for sharing with me so many great moments. Mishka, your courage, your sport skills, your enormous zest for life, your ability to listen and understand, and your unceasing optimism are unbeatable. It was my honor to work side-by-side with you and to be killed by you at lasertag multiple times. Niko, you are the kindest friend, the best badminton partner, and the terror of all stalkers. Thanks for discussing the TADF physics with me every time I got lost. One day I will learn to bake pancakes just the way you like, I promise. Rebecca Bönnighausen is responsible for developing my good taste

in YouTube videos, bonsai plants, and vegetarian meals. Becky, thanks for being always so sympathetic, cheerful, and open, for brightening our office, and for keeping all my secrets safe and sound. Christian Kasper is the only person, with whom I feel safe while driving at 280 km/h. Christian, your sense of humor and your charm is something I will really miss when I leave EP6. Kristofer Tvingstedt is the name I refer to, when I explain to external people, which group I belong to. Kris, your genuine involvement in physics, your deep feeling of truth and correctness, your ability to win every argument, your scientific knowledge and experience, and your inborn self-confidence keep filling me with awe. Benjamin Krugmann, Benny, thank you for hanging out with me, for our long walks in Würzburg and around, for our sushi dinners, and for hosting me in Nürnberg and in München. Nikita Drigo, thank you for skyping with me at any time of day and night, for dragging us both through the nightmare of paper writing, and for sending me packages of this white powder from EPFL. It was a real good stuff! Bernd Sturdza, Michael Hollenbach, Marshall Campbell, Simon Berger, Julian Höcker, Sebastian Weißenseel, Mathias Fischer, Nathania Henning, Manuel Ullrich, Moritz Fischer, Felix Klingert, Victor Soltamov, Johannes Junker, Melina Armer, Björn Kriete, Lisa Yi-Chieh Lee, Adam Whisnant… Guys, I am very lucky to know you and to have you on my side!

I thank SEPOMO project for financial support, for excellent organization, for inspiring network events, and for introducing me to the best professionals in the field of organic electronics. I also thank my fellow early-stage researchers for the unforgettable atmosphere during our meetings. I am grateful to my co-supervisor Moritz Riede for kindly accepting me in his group for a secondment.

My time here would not be quite as cloudless, if I would not feel permanent support from home. My precious university friends, every little message from you, every call, not to mention your visits, kept me sane, happy, and determined to move further. Алёнка Егорова, Дания Рудовская, Юля Юрчук, Мифтах Замалетдинов, Макс Сивков, Митя Чичинадзе, Олег Козлов, Данил Анисимов, Настя Рослякова, Даша Пономарёва, Серёжа Никулин, Ваня Цымбалов, Дима Белугин, Даша Жукова, Леночка Никонова, Гоша Бабайцев, Гоша Жарик, Игорь Данилович, Сашка Ульянов, Андрей Тархов, Стас Прокопьев, Игорь Григорьев, вы все мне очень дороги! Спасибо, что вы есть!

Special thanks go to my beloved parents. Мама и папа, я очень благодарна вам за то, что вы даёте мне так много свободы и одновременно так много поддержки. Спасибо за тёплый уютный дом, куда я всегда могу вернуться. Спасибо за каждое доброе слово, за каждый звонок, за то, что в любой ситуации вы на моей стороне и за то, что вы всегда рядом, даже если очень далеко. Я вас люблю!

Finally, my darling little brother Dmitry. Sometimes I really believe that we are twins. I hope that one day you will build a plane and we well fly away. Thank you for your enormous support and faith in me!